Polyelectrolyte nanostructures formed in the moving contact line: fabrication, characterization and application

Dissertation

zur Erladung des akademischen Grades

Doktor rerum naturalium

(Dr. rer. nat.)

vorgelegt

der Fakultät Mathematik und Naturwissenschaften

der Technischen Universität Dresden

von

Konstantin Demidenok

Geboren am 05.10.1979 in Orsk, Russland

Gutachter:

Eingereicht am:

Tag der Verteidigung:

Моему отцу и моей маме посвящается,
в благодарность за их доброту и мудрость

Contents

List of abbreviations

Latin letters

1D	One dimensional
2D	Two dimensional
3D	Three dimensional
AFM	Atomic Force Microscopy
APA	Alkyl-phosphonic acid
APS	Ammonium persulfate
CCD	Charge Coupled Device
DC	Direct Current
DNA / RNA	Deoxyribonucleic acid / Ribonucleic acid
FET	Field Effect Transistors
FIB	Focused Ion Beam
NW	Nanowire
P2VP	Poly-2-vinylpyridine
PDI	Polydispersity index
PDMS	Polydimethylsiloxane
PE	Polyelectrolyte
PGMA	Poly(glycidyl methacrylate)
PMB	Poly(methacryloyloxyethyldimethylbenzylammonium chloride)
PMMA	Poly(methyl methacrylate)
PPy	Polypyrrole
PS	Polystyrene
PSSA	Polystyrenesulfonic acid
PtBuA	Poly(tert-butyl acrylate)
PTFE	Polytetrafluoroethylene

PVP	Polyvinylpyrrolidone
PVP	Polyvinylpyrrolidone
Py	Pyrrole
Py-DPA	(12-pyrrol-1-yl-dodecyl)-phosphonic acid
SAM	Self-Assembled Monolayer
SEM	Scanning Electron Microscopy
SPM	Scanning Probe Microscopy
TEM	Transmission Electron Microscopy
UV	Ultraviolet
µCP	Microcontact printing

I want to build a billion tiny factories, models of each other, which are manufacturing simultaneously. . .

The principles of physics, as far as I can see, do not speak against the possibility of maneuvering things atom by atom. It is not an attempt to violate any laws; it is something, in principle, that can be done; but in practice, it has not been done because we are too big.

Richard Feynman, Nobel Prize winner in physics

General introduction

The concept of 'nano-technology' and its main principles were first introduced by physicist Richard Feynman in 1959. Feynman investigated the possibility of manipulating individual atoms and molecules in such a way that a set of tools was applied to build and operate another proportionally smaller set, and so on down to the needed scale. In the process scaling issues would arise from the changing magnitude of various physical phenomena: gravity would become less important, surface tension and Van der Waals attraction would become more important. This basic idea appears plausible, and exponential assembly enhances it with parallelism to produce a useful quantity of end products.[Feynman2000] The first definition of "nanotechnology" dates back to 1974 when professor Norio Taniguchi of Tokyo Science University proposed that "'Nano-technology mainly consists of the processing of, separation, consolidation, and deformation of materials by one atom or by one molecule".[Taniguchi1974] Later on the basic idea of this definition was explored and elaborated by Dr. K. Eric Drexler, who stressed the technological significance of nano-scale phenomena and devices in his speeches and the books Engines of Creation: The Coming Era of Nanotechnology (1986) and Nanosystems: Molecular Machinery, Manufacturing, and Computation.[Drexler1991]

The development of nanotechnology and nanoscience in the early 1980s was predetermined by the birth of cluster science and the invention of the scanning tunneling microscope. These events prepared ground for the discovery of fullerenes in

1985 and carbon nanotubes a few years later. At the same time the synthesis and properties of semiconductor nanocrystals were studied.

In its current sense nanotechnology is the study of the control of matter on an atomic and molecular scale.

Generally nanotechnology is concerned with structures of the size 100 nanometers or smaller, and involves developing materials or devices within that size. Nanotechnology is very diverse, ranging from novel extensions of conventional device physics, to completely new approaches based upon molecular self-assembly, to developing new materials with dimensions on the nanoscale, even to speculation on whether we can directly control matter on the atomic scale.

The heart of the matter is that as the size of the system decreases, a number of physical phenomena become pronounced which include statistical mechanical effects and quantum mechanical effects, for example the "quantum size effect" where the electronic properties of solids are altered with great reductions in particle size. This effect is not observed when we move from macro to micro dimensions but becomes evident and dominant when the nanometer size range is reached. Also, a number of physical (mechanical, electrical, optical, etc.) properties change when compared to macroscopic systems. One example is the increase in surface area to volume ratio altering mechanical, thermal and catalytic properties of materials.

In terms of its practical application, nanotechnology is often referred to as a general-purpose technology that will have significant impact on almost all industries and all areas of society. It offers better built, longer lasting, cleaner, safer, and smarter products for the home, for communications, for medicine, for transportation, for agriculture, and for industry in general.

A possible line of development of nanotechnology was proposed by Mihail Roco of the U.S. National Nanotechnology Initiative.[Roco1999] The author describes four generations of nanotechnology as outlined in the chart below. According to Roco, we are currently passing the generation of passive nanostructures, where materials are designed to perform one task, and are about to enter the second phase which will bring active nanostructures for multitasking; for example, actuators, drug delivery devices, and sensors. The third generation is expected to begin emerging around 2010 and will

feature nanosystems with thousands of interacting components. A few years after that, the first integrated nanosystems, functioning (according to Roco) much like a mammalian cell with hierarchical systems within systems, are expected to be developed (see figure 1).

1st: Passive nanostructures

    (a) Dispersed and contact nanostructures. Ex: aerosols, colloids
    (b) Products incorporating nanostructures. Ex: coatings, nanoparticle reinforced composites; nanostructures metals, polymers, ceramics

2nd: Active nanostructures

    (a) Bio-active, health effects. Ex: targeted drugs, biodevices
    (b) Physico-chemical active. Ex: 3D transistors, amplifiers, actuators, adaptive structures

3rd: Systems of nanosystems

    Ex: guided assembling; 3D networking and new hierarchical architectures, robotics, evolutionary

4th: Molecular nanosystems

    Ex: molecular devices "by design", atomic design, emerging functions

Figure 1: A possible line of development of nanotechnology.

The last few years witnessed a major boost of research activity in the field of nanoscale size objects. This may be accounted for, in the first place, by the advances in electron and ion beam microscopy, which lead to the spread of SEM, TEM, SEM+FIB machines; as well as by the increase of the functionality and precision of the SPM, AFM techniques. Noteworthey is the fact that SEM+FIB technique allows us to not only visualize nanoobjects, but also modify such and even create new ones. Therefore more and more scientific groups are getting engaged in the study of the properties and the functionality of nanoobjects. The nanotechnology information database keeps growing, which his reflected by the growing number of publications (as is demonstrated by the search results at http://pubs.acs.org).

Figure 2: The growing number of publications (search results at http://pubs.acs.org, word 'nano').

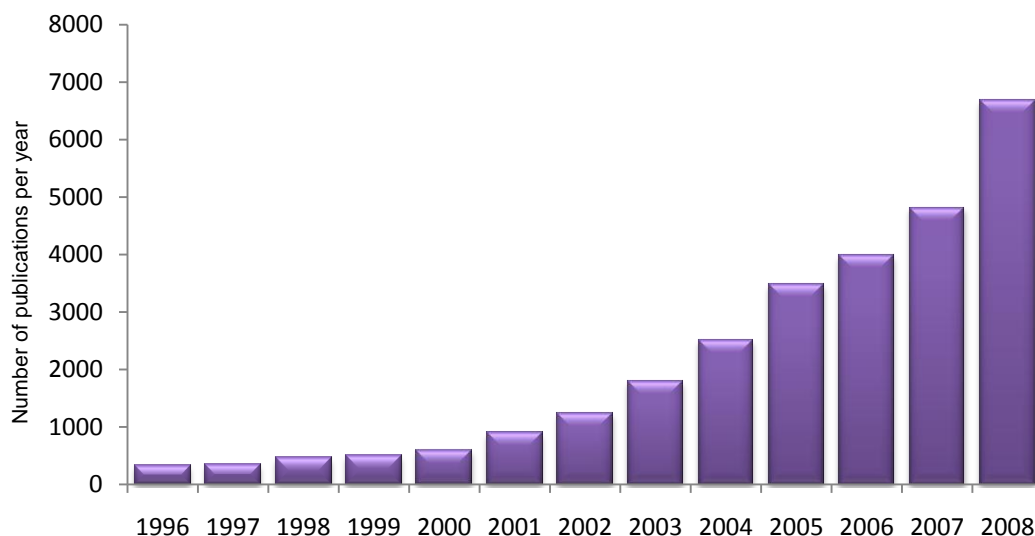Another sign of the increasing interest to the nanotechnology is the fact that over the last several years a considerable number of countries proposed their own national research programs in the field of nanotechnology. At the same time more and more international institutes and organizations have been emerging with the goal of fostering research and business collaboration, and providing advanced education and training in the field of nanotechnology. A number of nanotechnology subfields have been intensely investigated recently, such as organic and nonorganic nanotubes, polymer brushes, quantum nanodots, etc.

On the background of the overall advances in the field of nanotechnology the scientific society is paying close attention to the research of new nanomaterials, new techniques and methods which would allow for the matter assembly and manipulation at nanoscale level. Of particular importance are such processes of nanostructures formation when molecules are driven by self-induced, self-stabilized forces, i.e. the so called self-assembly processes.

The study of one of such process, of self-orientation and stretching of polymer molecules, and of the application of the latter for fabrication of nanostructures became the primary motivation of the present thesis.

A crucial problem of nanotechnology is that a number of different elements have to be integrated into complex and predictably operating systems. It was proposed in Leibniz Institute of Polymer Research Dresden that single molecules of polymers or their structures can be utilized as diverse and convenient nanotechnological building blocks.[Bocharova2004, Bocharova2005] It is important that the modern polymer chemistry provides an access to various molecules (building blocks) of desired size, shape (architecture) and functionality. Important advantage of the proposed "single-molecule" approach is a possibility for manipulation and organization of complex structures via self-assembly.

For instance, just like conventional ropes, single molecules of linear polymers could be stretched and aligned under external forces (e.g., centrifugal or capillary forces, electric or shear fields) and immobilized onto surfaces by simple procedures like casting or printing. Recently it was demonstrated that single polyelectrolyte molecules could be randomly deposited and stretched using a spincoating technique.[Bocharova2006] These molecules were used as templates for conductive nanowires fabrication, that makes them a perspective candidates for fabrication of nanodevices and sensors.[Bocharova2006-2] However, an important drawback of the developed method is its low reproducibility and uncontrolled orientation and positioning of the structures.

Aims & objectives

- To develop advanced deposition techniques for obtaining highly oriented, with known orientation, polymeric nanostructures by utilizing the moving three-phases (solid-liquid-gas) contact line;

- To identify the key factors of the nanostructures formation;

- To convert 1D polyelectrolyte templates into functional structures involving non-covalent interactions (e.g., selective adsorption of amphiphilic molecules bearing potentially useful functional groups);

- To fabricate electrically conductive conjugated polymer (polypyrrole) nanowires on the basis of 1D polyelectrolyte templates via selective polymerization.

Main results & achievements

Having conducted the research described in this thesis I found that there exists a possibility to produce polyelectrolyte nanostructures on hydrophobic surfaces by application of the moving contact line approach. It was demonstrated that the morphology of nanostructures displays a range of structure variations from root-like to a single wire structure with a high anisotropy and aspect ratio (providing diameters of several nanometers and the length limited by the sample surface dimensions). Such nanostructures can be produced exactly on the spot of interest or can be transferred from the surface where they were produced to any other surfaces by the contact printing technique.

A model describing the polymer deposition during the moving contact line processes on hydrophobic surfaces has been proposed. The application of this model provides the ground for an explanation of all the obtained experimental data.

Utilizing moving contact line approach aligned one-dimensional polycation structures were fabricated and these structures were used as templates for assembling amphiphile molecules.

Quasiperiodic aligned and oriented nanostructures of polyelectrolyte molecules formed in moving droplets were utilized for fabrication of electrically conductive one-dimensional nanowires.

Outline of the thesis

The first chapter gives the theoretical background for the interpretation of experimental data. In this chapter the main aspects of the long-wave theory and wetting have been described. The second chapter describes basics of the research techniques: atomic force microscopy, ellipsometry, conductive measurements and optical microscopy. The third chapter discusses the nanostructures fabrication using contact line movement approach. In this chapter I propose the model which explains experimental data. The fourth and fifth chapters are dedicated to the application of polymeric nanostructures obtained using contact line movement approach. In fourth

chapter I shows how polyelectrolyte nanostructure can be used as templates for SAM`s substances. The fifth chapter discusses the application of PSSA nanostructures for synthesis of polypyrrole nanowires and study of their conductive properties.

Publications

Demidenok K.; Bocharova V.; Stamm M.; Jahne E.; Adler H.-J. P.; Kiriy A. One-dimensional SAMs of (12-Pyrrol-1-yl-dodecyl)-phosphonic acid templated by polyelectrolyte molecules. Langmuir **2007**, 23, 9287-9292.

Demidenok K., Bocharova V., Kiriy A., Vinzelberg H., Mönch I., Stamm M. Electron transport in polypyrrole nanowires. *In progress.*

Demidenok K., Bocharova V., Kiriy A., Stamm M. Polyelectrolyte nanostructures formed in the moving contact line. *In progress.*

Contribution to the conferences

Poster: Stretching of polyelectrolyte molecules on hydrophobic surfaces. Demidenok K., Kiriy A., Stamm M. //*8th International Conference on Advanced Polymers via Macromolecular Engineering: Dresden, Germany, 2009.* Poster award granted

Poster: Polypyrrole nanowires grown from polyelectrolyte single molecules. Bocharova V., Demidenok K., Kiriy A., Moench I., Vinzelberg H., Stamm M. //*DPG (Conference of German Physical Society): Berlin, Germany, February 2008.*

Poster: Transport studies of polypyrrole nanowires grown from polyelectrolyte single molecules. Bocharova V., Demidenok K., Kiriy A., Moench I., Vinzelberg H., Stamm M. //*3rd International Symposium on „Reactive Polymers in Inhomogeneous Systems, in Melts, and at Interfaces"REACT2007: Dresden, Germany, 2007.*

Poster: Stretching of polyelectrolyte molecules on hydrophobic surfaces. Demidenok K., Bocharova V., Kiriy A., Stamm M. //*3rd International Symposium on „Reactive Polymers in Inhomogeneous Systems, in Melts, and at Interfaces"REACT2007: Dresden, Germany, 2007.*

Chapter 1.

Theoretical aspects of wetting and the long-wave theory approach

1.1. Wetting on the macroscopic scale

A large part of the work in this thesis deals with wetting of solid surfaces. It entails a detailed discussion of the underlying physics even though a lot of open questions will remain unanswered.

1.1.1. Contact angle and Young's law

In the theory of classical capillarity of the wetting phenomena, the interfacial tension γ_{ij} plays the key role. It represents the free energy necessary to increase by one unit the area of contact between two different phases i and j. The physical origin of this free energy can be explained as follows: Inside the dense phase, i, molecules attract each other, and their ability to interact with the neighbors of the same species i is higher when located in the bulk material than when they are close to the interface to phase j.
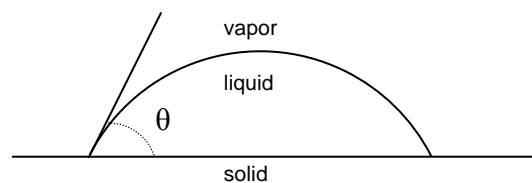

Figure 1.1: Scheme of wetting during the coexistence of three phases, respectively the liquid, solid and vapor phases. The contact angle is denoted by θ.

Suppose we have a solid substrate S wetted by a liquid L in contact with a vapor V, as shown in figure 1.1. Three interfaces can then be distinguished: liquid-vapor, solid-liquid, and solid-vapor with the correspondingly associated free surface energies: γ_{LV}, γ_{SL} and γ_{SV}, respectively.

In figure 1.1, a tendency is shown towards wetting rather than dewetting. Indeed, out of the two phases, liquid and vapor, the solid substrate prefers the liquid and disfavors the vapor. This can be seen from the spreading of the liquid on the solid substrate: the contact angle θ is less than 90°. Experimentally, the contact angle must be measured close enough to the wall, that is, within a few percent of the capillary length a_0.[Rowlinson1984] This length is a measure of the distance over which the liquid-vapor interface is curved, and results from the competition of the surface tension and gravity. It is defined as:

$$a_0 \; = \; \sqrt{\frac{2\gamma_{LV}}{g\Delta\rho}} \qquad (1.E1)$$

where g is the gravitational acceleration and $\Delta\rho$ is the density difference of the liquid and vapor. Typical values of a_0 are of the order of one millimeter. Also noteworthy is that all the free energies are "far-field", which means that these interfacial free energies act "sufficiently" far away from the region near the contact line of molecular dimensions. In figure 1.1, it can also be observed that, although the inequality $\gamma_{LS} < \gamma_{SV}$ applies, a direct solid-vapor contact is still tolerated. However, when the preference for adsorption of the liquid is increased here (for example, by changing the temperature), the vapor may become excluded from contact with the solid. Then, a liquid layer will intrude between the solid and vapor. This is termed *complete wetting*, whereas the situation in figure 1.1 represents *partial wetting*.

The thickness of the liquid wetting layer in the case of complete wetting is typically a few hundred angstroms. The equilibrium surface free energy of the solid-vapor interface is consequently defined as

$$\gamma_{SV} \geq \gamma_{SL} + \gamma_{LV} \qquad (1.E2)$$

at complete wetting.

For partial wetting, on the other hand, the inequality applies:

$$\gamma_{SV} < \gamma_{SL} + \gamma_{LV} \qquad (1.E3)$$

which expresses that although the solid-liquid contact is preferred, the solid-vapor interface has lower free energy than the combination of solid-liquid and liquid-vapor interfaces. Balancing the components of these forces along the direction parallel to the substrate and perpendicular to the contact line (the vertical direction in figure 1.1.) leads to:[Gennes1985]

$$\cos \theta = \frac{\gamma_{SV} + \gamma_{SL}}{\gamma_{LV}} \qquad (1.E4)$$

The angle θ is the contact angle, as defined in figure 1.1. Equation 1.E4 is also known as Young's law. Note that equation 1.E4 can also serve as the thermodynamic definition of the contact angle, when the surface free energies are known, but no direct observation of θ is made. Clearly, complete wetting corresponds to $\theta = 0$. Young's law needs to be generalized as soon as the surface tension of the interface between the two adsorbed phases is anisotropic. In the case of partial wetting, Young's law expresses the mechanical equilibrium of the forces (per unit length) that the interfaces exert on the contact line along which they meet. The contact angle given by Young's equation is static, i.e. Young's law applies to the equilibrium state of the system.

However, if the three phase (liquid/solid/vapor) boundary is in actual motion, the angles produced are called *dynamic contact angles* and are referred to as "advancing" and "receding" angles, as shown in figure 1.2. The difference between "advanced" and "advancing", "receded" and "receding" is that in the static case the motion is incipient while in the dynamic case the motion is actual. During its motion toward the equilibrium state, a liquid drop scans a range of dynamic contact angles. Dynamic contact angles may be determined at various rates of speed. Dynamic contact angles measured at low velocities should be equal to properly measured static angles.
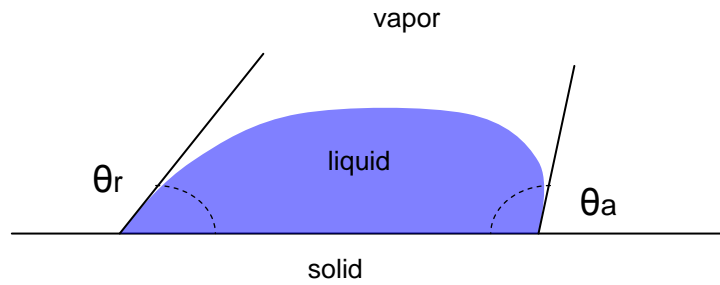
Figure 1.2: Side view of a sessile water drop on a solid surface showing advancing and receding contact angles (θ_a and θ_r)

1.1.2. Spreading coefficient

In cases of non-equilibrium situations, we may have a solid/vapor interfacial tension γ_{SV} that is larger than $\gamma_{SL} + \gamma_{LV}$. The difference

$$S = \gamma_{SV} - \gamma_{SL} - \gamma_{LV} \qquad (1.E5)$$

is called the spreading coefficient.

The transition from the partial to complete wetting can be discussed in terms of the equilibrium spreading coefficient S as follows. When S is positive, the spreading is energetically favored. The liquid spontaneously spreads and tends to cover the whole solid surface. Using Young's law (equation 1.E4), we obtain:

$$S = \gamma_{LV}(\cos\theta - 1) \qquad (1.E6)$$

so that for partial wetting $S < 0$, and for complete wetting $S = 0$. The wetting kinetics can now be characterized by the way in which S tends to zero, or, equivalently, the way in which $\cos\theta$ tends to 1.

Up to now, all the situations mentioned above can be summarized in terms of the contact angle as:

• complete wetting $\leftrightarrow$ $\theta = 0^o$

- partial wetting $\leftrightarrow 0^{\mathrm{o}} < \theta < 90^{\mathrm{o}}$
- partial drying $\leftrightarrow 90^{\mathrm{o}} < \theta < 180^{\mathrm{o}}$

From the values of bulk cohesive energy, there are two main types of solids: a) hard solids (covalent, ionic, or metallic), which have a solid/vapor interfacial energy of γ_{sv} - 500 to 5000 ergs/cm² and b) weak molecule crystals and organic liquids (bound by van der Waals forces, or in some special cases, by hydrogen bonds), which have a γ_{sv} of 50 ergs/cm².[Fox1955] Most molecular liquids can have complete wetting on high-energy surfaces. This can be explained qualitatively as follows: the underlying solid usually has a polarity much higher than that of the liquid. In contrast, low-energy surfaces can also give rise to partial or complete wetting. It depends on the surface tension of the liquid. For complete wetting, there exists a "critical surface tension". Only when the surface tension of the chosen liquid is smaller than the critical value can complete wetting occur.

1.1.3. Tanner's law

It is important to notice that the effect of body forces such as gravity on the contact line is vanishingly small and that, therefore, equation 1.E4 is valid even in the presence of gravity or any other body force. Only such forces as viscous forces which might become increasingly large at the contact line can affect Young's law. In the case when the surface tension is the only driving force, Tanner's spreading law [Tanner1979] is an approximated solution of the hydrodynamics of spreading.

Regard a nonvolatile liquid drop on a nonreactive smooth surface when inertial or viscoelastic effects are neglected. Furthermore, the drops are supposed to be small enough for the gravity to be negligible.

On the macroscopic scale, according to Tanner, a universal spreading equation, regarded as Tanner's law, reads:

$$\frac{da}{dt} = \upsilon^* \theta^3 \qquad (1.E7)$$

where a is the radius of the liquid-substrate contact area and υ^* is the characteristic velocity, defined by

$$\upsilon^* = \frac{\gamma_{LV}}{\mu} \qquad \text{(1.E8)}$$

where μ is the viscosity of the spreading liquid.

As a result of equation 1.E7, this model gives the radius a as a function of the time t in the complete wetting regime as $a \sim t^n$.

Tanner's law has also been obtained by de Gennes from the balance between the viscous dissipation and the work done by the surface tension force.[de Gennes1985] He uses a general equation that describes the profile of the droplet near the edge when the long-range forces are negligible. In this more general theory, the dependence of a on the droplet volume V is obtained by:

$$a \sim V^m (\upsilon^* t)^n \qquad \text{(1.E9)}$$

with $n = 0.1$, $m = 0.3$.

Lopez *et al.* have analyzed the situation, when gravity is the main driving force.[Lopez1976] They obtained a similar power law with $n = 0.125$ and $m = 0.375$. These theories are based on the steady state arguments focusing on the edge of the film and using a lubrication approximation.

Tanner and Lopez compared theories to experiments, finding good agreement in both cases. Hydrodynamic models, however, do not predict the dependence of n on a change such as in temperature or in pH value which alter both the surface tension and the viscosity. The lack of a controlled experimental environment might therefore explain the range of observed values of n and m.

1.1.4. Cox equation

A model avoiding the difficulties of the hydrodynamic description of the moving contact line was proposed first by Hansen and Toong.[Hansen1971] The flow in a dynamic

meniscus is divided into two regions: the inner region, in immediate proximity to the contact line (with characteristic dimension L_S) and the outer one (with dimension $L \gg L_S$). The introduction of the inner region is imposed by the singularity of the viscous stresses appearing at the contact line.[Huh1971] Either the inner region is excluded from the hydrodynamic consideration [Hansen1971, Voinov1976] or another mechanism removing the singularity is assumed - slippage of the liquid with respect to the solid [Dusean1979] or existence of long-range attraction forces in the three-phase contact zone.[Gennes1985]

The solution of the hydrodynamic problem proposed by Cox assumes slippage of the fluid in the inner region.[Cox1986] The dependence of the dynamic contact angle θ on the contact line velocity V is expressed by the equation:

$$g(\theta, \varepsilon) = g(\theta_0, \varepsilon) \pm Ca \ln (L/L_S) \qquad (1.E10)$$

θ refers to the intermediate region between the inner and outer ones, [Hocking1982] and the dimension L_S of the inner region takes the meaning of the slip length. $g(\theta, \varepsilon)$ is defined as

$$g(\theta, \varepsilon) = \int_0^\theta \frac{d\beta}{f(\beta,\varepsilon)}$$

$$f(\beta, \varepsilon) = \frac{2 \sin \beta [\varepsilon^2(\beta^2 - \sin^2 \beta) + 2\varepsilon\{\beta(\pi - \beta) + \sin^2 \beta\} + \{(\pi - \beta)^2 - \sin^2 \beta\}]}{\varepsilon(\beta^2 - \sin^2 \beta)\{(\pi - \beta) + \sin \beta \cos \beta\} + \{(\pi - \beta)^2 - \sin^2 \beta\}(\beta - \sin \beta \cos \beta)} \qquad (1.E11)$$

At advancing (plus sign), $\varepsilon = \frac{\mu_r}{\mu_a}$ is the viscosity ratio of the receding and advancing fluid, and the capillary number should be written as $Ca = \frac{\mu_a V}{\gamma}$. At receding (minus sign), $\varepsilon = \frac{\mu_a}{\mu_r}$ and $Ca = \frac{\mu_r V}{\gamma}$ (γ is the fluid/fluid interfacial tension).

The contact angle θ_0 is the "microscopic contact angle", defined in the inner region. In most hydrodynamic considerations it is assumed to be constant and velocity independent.[Hocking1982, Hansen1971, Lowndes1980] However, Cox, Voinov, and Dussan admit the possibility of a nonhydrodynamic velocity dependence of θ_0.

Blake and Haynes consider the wetting kinetics as a process of desorption of the molecules of the receding fluid and adsorption of those of the advancing one onto adsorption centers of the solid surface.[Blake1969] Their equation could be regarded as a

balance of the driving force $\gamma \, |\cos \theta_Y - \cos \theta|$ and the friction force located in the three-phase contact zone (both taken per unit length of the contact line):

$$\cos \theta = \cos \theta_Y \pm (2nkT/\gamma) \; \text{arsh} \; (V/2K\lambda) \qquad (1.E12)$$

k and T are the Boltzman constant and temperature, K is the equilibrium frequency of molecular oscillation between two adjacent adsorption centers, situated at a distance λ, and n is the average two-dimensional concentration of these centers ($n \approx \lambda^{-2}$). The minus sign in eq. 1.E12 refers to advancing, while the plus sign denotes receding. θ_Y is the equilibrium Young contact angle.

Taking into account the nonhydrodynamic velocity dependence of the angle θ_0 more general expression is obtained:

$$g(\theta,\varepsilon) = g(\theta_0(V),\varepsilon) \pm \text{Ca} \; \ln \; (L/L_S) \qquad (1.E13)$$

where $\theta_0(V) = \arccos \{ \cos \theta_Y \pm (2nkT/\gamma) \; \text{arsh} \; (V/2K\lambda) \}$.

When the viscosity of the advancing phase is negligibly low ($\varepsilon \approx 0$) and the dynamic contact angle is less than $3\pi/4$, the Cox function $g(\theta, \varepsilon)$ can be approximated by $\theta^3/9$.[Sedev1992]

1.1.5. The role of the disjoining pressure

As was mentioned earlier, if the spreading coefficient S is positive, spontaneous spreading occurs, and the equilibrium situation corresponds to a complete coverage of the solid by a thin liquid film. However, several measurements of the spreading kinetics of liquids on a large variety of substrates seem to give spreading kinetics approximately independent of S, and the adequacy of a description based on interfacial energies and simple hydrodynamic concepts has been widely debated.[Marmur1983] To solve this dilemma Joanny and de Gennes pointed out the role of molecular long-range forces, which may result in the formation of a precursor film.[Gennes1985, Joanny1986] They stated that when a film is very thin, long-range forces cannot be neglected. These forces may be

electrostatic, steric or van der Waals in nature. In this thesis, all the long-range forces are restricted to the van der Waals interactions, which always exist between two atoms or molecules. The potential of interaction is attractive and decreases with intermolecular distance r as r^{-6}; this is the so-called nonretarded regime. When this potential is integrated over all pair wise interactions between two half-spaces separated by a small distance h_0, one finds a slow decreasing potential:[Israelachvili1992]

$$W(h_0) = -\frac{A}{12\pi h_0{}^2} \qquad (1.E14)$$

where A is an effective Hamaker constant [Visser1972] which contains all non-geometric contributions to the interaction, on the order of a few kT (where k is the Boltzmann constant and T is the absolute temperature), and h_0 is the liquid film thickness. If A is positive, the interaction is attractive. As an example, A is always positive between two identical bodies, which explains why particles in solution generally flocculate.

In the case of a liquid film deposited on a solid surface, the two half-spaces are different (solid and gas, as shown in figure 1.3), and the Hamaker constant can be either positive or negative. In the wetting conditions, A is negative: the solid and the gas repel each other through the liquid. The effect of the long-range forces, that is the disjoining pressure, is then to make the liquid film thicker, since W(h) has a minimum for an infinite liquid thickness (h = ∞). The sign of A can be determined from approximate combining relations:

$$A \cong A_{SV} + A_{LL} - A_{LV} - A_{SL} \qquad (1.E15)$$

where A_{IJ} is the Hamaker constant in general between media *I* and *J* (which could be either a liquid, a vapor or a solid), which is proportional to the product of the densities of phases *I* and *J* and to the product of their polarizabilities $\alpha_I \alpha_J$. As the density of the gaseous phase is generally negligible, A is negative when the polarity of the solid is larger than that of the liquid. Therefore, a solid of high surface energy, such as metal or clean glass, should be wet by all common liquids.
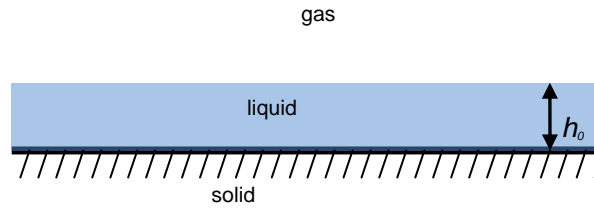
gas

liquid

h_o

solid

Figure 1.3: Wetting film on a planar solid surrounded by a gas.

1.1.6. Navier–Stokes equation

The Navier–Stokes equation, see Eq. 1.E16., named after Claude-Louis Navier and George Gabriel Stokes, describes the motion of fluid substances, that is substances which can flow. These equations arise from applying Newton's second law to fluid motion, together with the assumption that the fluid stress is the sum of a diffusing viscous term (proportional to the gradient of velocity), plus a pressure term.

$$\rho \left(\frac{\partial \mathbf{v}}{\partial t} + \mathbf{v} \cdot \nabla \mathbf{v} \right) = -\nabla p + \nabla \cdot \mathbb{T} + \mathbf{f} \qquad (1.E16)$$

The Navier-Stokes equations are based on the macroscopic, continuum model of fluids (and not by definition molecular). Classically, the governing boundary condition for a viscous fluid at a solid boundary is that of continuity of the velocity.

In particular, the condition can be mathematically realized by imposing that the velocity field be continuous across any two media. For a solid boundary the tangential velocity must be zero since there clearly is not any velocity in the solid. The following is the no-slip boundary condition at the intersection between the solid and fluid. The basis for such a boundary condition comes from a microscopic argument. It is argued that if there exists a slip between the two media, this slip gives rise to a stress that tends to force the system to equilibrate, i.e. the momentum gets dissipated to a mean level that causes the velocities to be equal on both sides of the said interface. The Navier-Stokes equations along with the no-slip condition at the boundary are referred to as the classical theory.

Entangled polymers do not flow like common liquids. De Gennes predicted that polymers slip on "smooth, passive" surfaces.[de Gennes1979] The slippage is characterized by the *extrapolation length b,* defined by the distance to the wall at which the velocity extrapolates to zero, see figure 1.4. A pressure gradient parallel to the film induces a usual Poiseuille flow in thick films (thickness $h \gg b$), but a plug flow in thin films *(h < b):* the polymer then moves like a solid, and the viscous dissipation is confined at the solid/liquid interface. The conditions required to observe a slippage of the polymer have been studied recently.
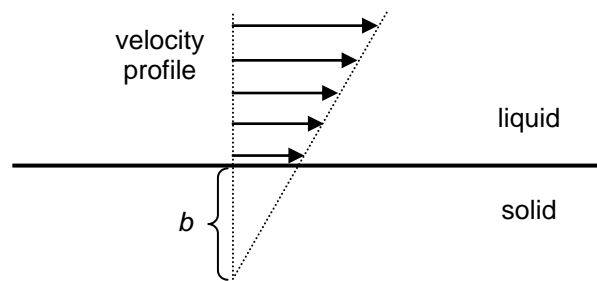

Figure 1.4: Sketch of the polymer slippage on a solid surface.

When a solid surface is perfectly smooth and passive the length b is large, and the polymer is expected to slip; i.e. there exists a nonzero flow velocity, V_S, at the solid surface. The ratio between the shear stress σ at the solid-liquid interface and the surface velocity V_S defines the friction coefficient κ:

$$\sigma = \kappa V_s \qquad\qquad (1.\text{E}17)$$

Two forms of the shear stress give equation:

$$\sigma = \eta \left(\frac{dV}{dZ}\right)_{z=0} = \kappa V_s \qquad\qquad (1.\text{E}18)$$

where η is the bulk polymer viscosity. Then

$$b = V_s / \left(\frac{dV}{dZ}\right)_{z=0} = \frac{\eta}{k} \qquad\qquad (1.\text{E}19)$$

For ideal conditions, $\kappa = \kappa_o \approx \eta_o/a$, where η_o is the monomer viscosity and a is the molecular size. The viscosity η is huge for an entangled melt [$\eta \approx \eta_o (N^3/N_e^2)$, where N is the polymerization index and N_e is the threshold for entanglements ($N_e \approx 100$)]. Equation 1.E19 leads to

$$b_p \approx a \, (N^3/N_e^2) \qquad\qquad (1.E20)$$

$b_p \approx 10$ μm for $N = 10^3$ and $N_e = 10^2$.[Brochard-Wyart1994]

1.2. The long-wave theory approach

Thin liquid films display a variety of interesting dynamics. Since the interface between the liquid and the surrounding gas is a deformable boundary, these films display wave motion; the waves can travel and steepen under certain conditions for high flow rates, and the waves can make transitions into quasiperiodic or chaotic structures. The film can rupture, leading to holes in the liquid that expose the substrate to the ambient gas. The connectedness of the film changes in this case, as it does if droplets of liquid are dislodged from the film. Changes in the structure occur in flows having contact lines leading to fingered patterns.

The lubrication theory or long-wave theory approach is based on the asymptotic reduction of the governing equations and boundary conditions to a simplified system which often consists of a single nonlinear partial differential equation formulated in terms of the local thickness of the film. The rest of the unknowns, i.e. the fluid velocity, fluid temperature, etc., are then determined via the functionals of the solution of that differential equation. The notorious complexity of the free boundary problem is thus removed. However, the resulting penalty is the presence of the strong nonlinearity in the governing equation(s) and the higher-order spatial derivatives appearing there. A simplified linear stability analysis of the problem can be carried out based on the resulting evolution equation. A weakly nonlinear analysis of the problem is also possible through that equation. However, the fully nonlinear analysis that allows one to

study finite-amplitude deformations of the film interface must be performed numerically. Still, the numerical solution of the evolution equation is considerably less difficult than the numerical solution of the original, free-boundary problem.

1.2.1. Slipper bearing

The long-scale methods that will be used to describe interfacial instabilities have their origins in the lubrication theory of viscous fluids. The easiest way to illustrate this theory is by considering a fluid-lubricated slipper bearing. Fluid-lubricated bearings are machine parts in which viscous fluid is forced into a converging channel. The flow creates vertical pressure forces that can be used to support large loads and hence reduce wear. In his pioneering work Reynolds laid the foundations for the theory of lubrication.[Reynolds1886] He applied the hydrodynamics of the slow viscous flow and derived the fundamental differential equation of the field, found approximate solutions for this equation, and compared his theoretical results with the experiments performed earlier. This idea is illustrated below where the structure called a slipper bearing is displayed. Many more details related to Reynolds and others work can be found in Dowson's publication.[Dowson1979]

In figure 1.5, a (solid) bearing is shown in which a plate at $z = 0$ moves in the positive x direction at constant speed U_0 driving fluid into the converging channel. In steady flow, the lower boundary of the bearing (the upper boundary of the channel) is at $z = h(x)$. The fluid is taken to be an incompressible, Newtonian viscous fluid of viscosity μ, density ρ, and kinematic viscosity $\nu = \mu/\rho$. When the length of the plate L is large, the liquid is able to support a load due to the large pressures generated under the bearing. For a fixed channel narrowing $\Delta h = h(0) - h(L)$, the tilt angle

$$a \equiv \mathrm{d}h/\mathrm{d}x \qquad\qquad (1.E21)$$
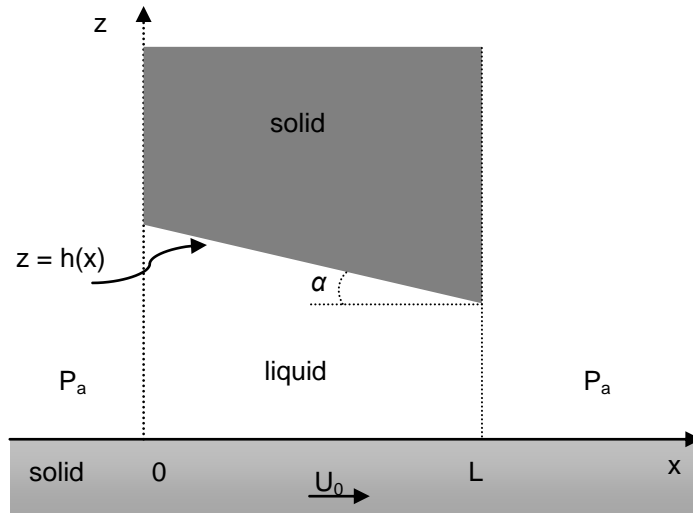
is small within this limit.

Figure 1.5: Slipper bearing. The plate moves with the constant velocity U_0. The lower boundary of the bearing, located at $z = h(x)$, is static and tilted at a small angle α. The external pressure is p_a.

Under this condition and in two dimensions, the Navier-Stokes and continuity equations can be reduced [Schlichting1968] to the simplified forms

$$\mu\partial_z^2 u - \partial_x p = 0, \qquad (1.E22)$$

$$-\partial_z p = 0, \qquad (1.E23)$$

$$\partial_x u + \partial_z w = 0, \qquad (1.E24)$$

where the velocity vector is $\vec{v} = (u, w)$, and p is the pressure in the fluid. Equation 1.E22 tells us that since a is small, the flow is locally parallel. Equation 1.E23 states that the pressure is vertically uniform (or, if gravity were to be included, hydrostatic). Equation 1.E24 is the continuity equation.

The boundary conditions below the bearing, $0<x<L$, are

$$u(0) = U_0, \qquad w(0) = 0, \qquad u(h) = 0. \qquad (1.E25)$$

Beyond the bearing, $x \leq 0$ and $x \geq L$, the pressure is atmospheric, and in particular

$$p(0) = p(L) = p_a. \qquad\qquad (1.E26)$$

Given that p depends on x only, one can solve the system (1.E22-1.E26) directly to find that

$$\mu u(z) = \tfrac{1}{2}\partial_x p(z^2 - hz) + \mu U_0(1 - \tfrac{z}{h}); \qquad\qquad (1.E27)$$

the flow is a linear combination of the plane Poiseuille and plane Couette flows. Of course, $p(x)$ is not yet known.

Given that the flow is steady, the flow rate Θ (in the x direction),

$$\Theta = \int_0^{h(x)} u(z)dz, \qquad\qquad (1.E28)$$

must be constant, which gives

$$\mu\Theta = -\tfrac{1}{12}h^3\partial_x p + \tfrac{1}{2}\mu U_0 h. \qquad\qquad (1.E29)$$

Alternatively, one can write the derivative of this equation,

$$\partial_x\left(-\tfrac{1}{12}h^3\partial_x p + \tfrac{1}{2}\mu U_0 h\right) = 0. \qquad\qquad (1.E30)$$

Equation 1.E30 is the Reynolds lubrication equation. Given $h(x)$, it is an ordinary differential equation for p.

It is possible to extend the theory to situations in which h depends (slowly) on time t. In this case Eq. 1.E30 would have the form

$$\mu\partial_t h + \partial_x\left(-\tfrac{1}{12}h^3\partial_x p + \tfrac{1}{2}\mu U_0 h\right) = 0, \qquad\qquad (1.E31)$$

or in the case of a three-dimensional flow, $h = h(x, y, t)$,

$$\mu \partial_t h + \vec{\nabla}_1 \left(-\frac{1}{12} h^3 \vec{\nabla}_1 p + \frac{1}{2} \mu \vec{U}_0 h \right) = 0, \qquad (1.E32)$$

Here

$$\vec{\nabla}_1 = \left(\frac{\partial}{\partial x}, \frac{\partial}{\partial y} \right), \vec{U}_0 = (U_0, V_0). \qquad (1.E33)$$

Now I would like to turn to the main subject of this part of the chapter, starting with the basics of the long-scale methods. One will notice the similarity between the time-dependent Reynolds lubrication equation 1.E30 and the general evolution equations for thin, bounded liquid films, Eqs. 1.E69 and 1.E70 derived below. Thus the slipper bearing theory carries one to the more general cases of films with free surfaces, and so to the phenomena of wave propagation, free-surface instability, and film rupture.

1.2.2. The evolution equation for a bounded film

The lubrication approximation will now be applied to a viscous-liquid flow, bounded below by a horizontal plate and above by an interface between the liquid and a passive gas, as shown in figure 1.6. Here one allows the possibility on the interface of external normal $\vec{\Pi}$ and tangential $\vec{\tau}$ stresses, slowly varying in space and time. Further, a conservative body force with potential φ is allowed.
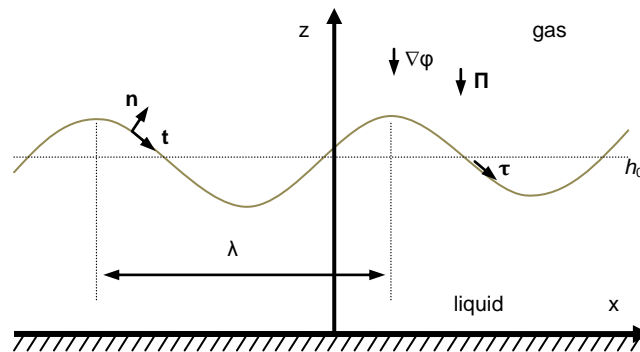

Figure 1.6: Sketch of a bounded liquid film. The body force is $\vec{\nabla}\varphi$, and the imposed normal and tangential stresses are $\vec{\Pi}$ and $\vec{\tau}$, respectively.

The Navier-Stokes and continuity equations in two dimensions have the form

$$\rho(\partial_t u + u\partial_x u + w\partial_z u) = -\partial_x p + \mu\nabla^2 u - \partial_x \varphi, \qquad (1.E34)$$

$$\rho(\partial_t w + u\partial_x w + w\partial_z w) = -\partial_z p + \mu\nabla^2 w - \partial_z \varphi, \qquad (1.E35)$$

$$\partial_x u + \partial_z w = 0, \qquad (1.E36)$$

where $\nabla^2 = \dfrac{\partial^2}{\partial x^2} + \dfrac{\partial^2}{\partial z^2}$.

The classical boundary conditions between the liquid and the plate are those of no penetration, $w = 0$, and no slip, $u = 0$. These conditions are appropriate for the continuous films to be considered here. However, we wish to derive equations now that will apply not only to this case but also to the case in which a contact line (or trijunction) exists and the liquid spreads on the solid substrate and displaces the surrounding fluid (say, gas). The classical conditions then lead to a nonintegrable singularity at the contact line [Huh1971, Dussan1974], which can be relieved by allowing a relative motion, slip, between the liquid and the solid near the contact line. In order to include such cases we generalize the conditions. The condition of no penetration is retained and the tangential relative motion is allowed. The Navier model that assumes a slip proportional to the shear stress gives

at z=0: $\qquad\qquad w = 0, u - \beta\partial_z u = 0. \qquad\qquad (1.E37)$

Here β is the slip coefficient, which will be taken to be zero for the case of continuous films.

On $z = h(x, t)$:

$$w = \partial_t h + u\partial_x h, \qquad (1.E38)$$

$$\mathbf{T} \cdot \vec{\mathbf{n}} = -\kappa\sigma\vec{\mathbf{n}} + \frac{\partial\sigma}{\partial s}\vec{\mathbf{t}} + \vec{\mathbf{f}}, \qquad (1.E39)$$

where $\mathbf{T}$ is the stress tensor of the liquid, $\vec{\mathbf{n}}$ is the unit outward vector normal to the interface, $\vec{\mathbf{t}}$ is the unit vector tangential to the interface, $\vec{\mathbf{f}}$ is the prescribed forcing at the

interface, whose normal and tangential components are $\vec{\Pi}$ and $\vec{\tau}$, respectively, κ is the mean curvature of the interface, and s is the arc length along the interface, such that

$$\vec{\mathbf{n}} = \frac{(-\partial_x h, 1)}{[1+(\partial_x h)^2]^{1/2}}, \ \vec{\mathbf{t}} = \frac{(1, \partial_x h)}{[1+(\partial_x h)^2]^{1/2}}, \kappa = -\vec{\nabla}_1 \vec{\mathbf{n}}. \qquad (1.\text{E}40)$$

Equation 1.E38 is the kinematic boundary condition (in the absence of the interfacial mass transfer) that balances the normal component of the liquid velocity at the interface with the speed of the interface. Equation 1.E39 has two components. Its tangential component states that the shear stress on the interface is balanced by the sum of $\vec{\tau}$ and the surface gradient of the surface tension σ. Its normal component states that the normal stress minus $\vec{\Pi}$ exhibits a jump equal to the surface tension times the mean curvature. When the external force $\vec{\Pi}$ is zero, and the fluid has zero viscosity, then $\mathbf{T} \cdot \vec{\mathbf{n}} \cdot \vec{\mathbf{n}} = -p$, and this component equation reduces to the well-known Laplace equation, which describes the excess pressure in the air bubble, compared to the external pressure, as twice the surface tension divided by the bubble radius.[Landau1987]

Let me now introduce scales for thin films that are motivated by the arguments and scalings used in the analysis of the slipper bearing. Consider length scales in the x direction defined by wavelength λ on a film of mean thickness h_0. Consider the distortions to be of *long scale* if

$$\epsilon = \frac{2\pi h_0}{\lambda} \ll 1. \qquad (1.\text{E}41)$$

It is natural to scale z to h_0; then the dimensionless z coordinate is

$$Z = \frac{z}{h_0} \qquad (1.\text{E}42)$$

and x to λ, or equivalently, $\frac{h_0}{\epsilon}$. Then the dimensionless x coordinate is given by

$$X = \frac{\epsilon x}{h_0}. \qquad (1.\text{E}43)$$

Likewise if there are no rapid variations expected as $\epsilon \to 0$, then

$$\frac{\partial}{\partial X}, \frac{\partial}{\partial Y} = O(1). \qquad (1.\text{E}44)$$

If $u = O(1)$, the dimensionless fluid velocity in the x direction is

$$U = \frac{u}{U_0}, \qquad (1.\text{E}45)$$

where U_0 is the characteristic velocity of the problem. Then the continuity requires that the dimensionless fluid velocity in the z direction be

$$W = \frac{w}{\epsilon U_0}. \qquad (1.\text{E}46)$$

Time is scaled to λ/U_0 so that the dimensionless time is

$$T = \frac{\epsilon U_0 t}{h_0}. \qquad (1.\text{E}47)$$

Finally, one expects, as in the slipper-bearing example, a locally parallel flow in the liquid so that $\partial_x p \sim \mu \partial_z^2 u$ and hence the dimensionless stresses, body-force potential, and pressure are

$$(\vec{\tau}, \vec{\Pi}) = \frac{h_0}{\mu U_0}(\vec{\tau_0}, \epsilon \vec{\Pi_0}), \ (\Phi, P) = \frac{\epsilon h_0}{\mu U_0}(\varphi, p). \qquad (1.\text{E}48)$$

Notice that the ''pressures'' are large due to the lubrication effect. If these forms are substituted into the governing system 1.E34–1.E40, the following scaled system is obtained:

$$\epsilon Re(\partial_T U + U \partial_X U + W \partial_Z U) = -\partial_X P + \partial_Z^2 U + \epsilon^2 \partial_Z^2 U - \partial_X \Phi, \qquad (1.\text{E}49)$$

$$\epsilon^3 Re(\partial_T W + U \partial_X W + W \partial_Z W) = -\partial_Z P + \epsilon^2(\partial_Z^2 W + \epsilon^2 \partial_X^2 W) - \partial_Z \Phi, \qquad (1.\text{E}50)$$

$$\partial_X U + \partial_Z W = 0. \qquad (1.\text{E}51)$$

At Z=0,

$$W = 0, U - \beta_0 \partial_Z U = 0. \qquad (1.E52)$$

Here $\beta_0 = \frac{\beta}{h_0}$ is the dimensionless slip coefficient.

At Z=H,

$$W = \partial_T H + U \partial_X H, \qquad (1.E53)$$

$$(\partial_Z U + \epsilon^2 \partial_X W)[1 - \epsilon^2 (\partial_x H)^2] - 4\epsilon^2 (\partial_x H)(\partial_X U) = \tau_0 [1 + \epsilon^2 (\partial_X H)^2] + \partial_X \Sigma[1 +$$
$$\epsilon 2(\partial XH)21/2, \qquad (1.E54)$$

$$-P - \Pi_0 + \frac{2\epsilon^2}{[1+\epsilon^2(\partial_X H)^2]}\{\partial_X U[\epsilon^2(\partial_X H)^2 - 1] - \partial_X H(\partial_Z U + \epsilon^2 \partial_X W)\} = \frac{C^{-1}\epsilon^3 \partial_X^2 H}{[1+\epsilon^2(\partial_X H)^2]^{3/2}},$$

$$(1.E55)$$

where H = h/h_0 is the dimensionless thickness of the film and $\Sigma = \frac{\epsilon\sigma}{\mu U_0}$ is the dimensionless surface tension. The Reynolds number Re and capillary number C are given, respectively, by

$$Re = \frac{U_0 h_0}{\upsilon}, \qquad C = \frac{U_0 \mu}{\sigma}. \qquad (1.E56)$$

Before taking limits, we integrate the continuity Eq. 1.E49 in Z from 0 to H(X,T), use integration by parts, Eq. 1.E53, and the boundary conditions 1.E52 to obtain

$$\partial_T H + \partial_x \left(\int_0^H U dZ \right) = 0. \qquad (1.E57)$$

This equation constitutes a more convenient form of the kinematic condition and ensures conservation of mass on a domain with a deflecting upper boundary.

Finally, I seek the solution of the governing Eqs. 1.E34–1.E40 as a perturbation series in powers of the small parameter ϵ:

$$U = U_0 + \epsilon U_1 + \epsilon^2 U_2 + \cdots,$$

$$W = W_0 + \epsilon W_1 + \epsilon^2 W_2 + \cdots, \qquad (1.E58)$$

$$P = P_0 + \epsilon P_1 + \epsilon^2 P_2 + \cdots.$$

One lubrication approximation of the governing system is obtained by letting Re, C = O(1) as $\epsilon \to 0$. In the former case the inertial terms, measured by ϵRe, are one order of magnitude smaller than the dominant viscous terms, consistent with the local parallel flow assumption. In the latter case, the surface tension terms, measured by $C^{-1}\epsilon^3$, are two orders of magnitude smaller and would be lost. It will turn out to be essential to retain the surface tension effects at leading order, so that one writes

$$\overline{C} = C\epsilon^{-3} \qquad\qquad (1.E59)$$

and takes another lubrication limit Re, $\overline{C}$ = O(1) as $\epsilon \to 0$. The latter is applied when the surface tension effects are strong relative to the others. At leading order in ϵ the governing system becomes, after omitting the subscript 0 in U$_0$,W$_0$, and P$_0$,

$$\partial_Z^2 U = \partial_X P + \partial_X \Phi, \qquad\qquad (1.E60)$$

$$0 = \partial_Z P + \partial_Z \Phi, \qquad\qquad (1.E61)$$

$$\partial_T H + \partial_X \left(\int_0^H U \, dZ \right) = 0. \qquad\qquad (1.E62)$$

At Z=0,

$$U - \beta_0 \partial_Z U = 0, \qquad\qquad (1.E63)$$

and, at Z=H,

$$\partial_Z U = \tau_0 + \partial_X \Sigma, \qquad\qquad (1.E64)$$

$$-\Pi_0 - P = \overline{C}^{-1} \partial_X^2 H. \qquad\qquad (1.E65)$$

For our purposes, there is no need to find W, although it can be obtained by solving Eq. 1.E51 with the first condition of 1.E52. Note the similarity to Eqs. 1.E22-1.E26 for the slipper bearing when $\beta_0 \equiv h_0\beta = 0$ in Eq. 1.E63. Again, there is locally parallel flow, but now the upper boundary has prescribed the shear stress, normal stress, and surface tension, and there is a conservative body force.

In order to solve these equations it is convenient to introduce a reduced pressure $\overline{P}$,

$$\overline{P} = P + \Phi. \qquad\qquad (1.E66)$$

It follows from Eqs. 1.E61 and 1.E64 that

$$\overline{P} = \Phi \big|_{Z=H} - \overline{C}^{-1} \partial_X^2 H - \Pi_0. \qquad\qquad (1.E67)$$

In this case

$$U = (\tau_0 + \partial_X \Sigma)(Z + \beta_0) + \partial_X \overline{P}(\tfrac{1}{2} Z^2 - HZ - \beta_0 H), \qquad\qquad (1.E68)$$

as follows from Eqs. 1.E60, 1.E66 and 1.E67. If form 1.E68 is substituted into the mass conservation condition of Eq. 1.E62, one obtains the appropriate evolution equation for the interface,

$$\partial_T H + \partial_X \left[(\tau_0 + \partial_X \Sigma) \left(\tfrac{1}{2} H^2 + \beta_0 H \right) \right] - \partial_X \left[\left(\tfrac{1}{3} H^3 + \beta_0 H^2 \right) \partial_X \overline{P} \right] = 0. \qquad\qquad (1.E69)$$

In three dimensions one can show that the evolution equation has the form

$$\partial_T H + \vec{\nabla}_1 \left[(\vec{\tau}_0 + \vec{\nabla}_1 \Sigma) \left(\tfrac{1}{2} H^2 + \beta_0 H \right) \right] - \vec{\nabla}_1 \left[\left(\tfrac{1}{3} H^3 + \beta_0 H^2 \right) \vec{\nabla}_1 \overline{P} \right] = 0. \qquad\qquad (1.E70)$$

where $\vec{\tau}_0$ is the vector shear stress imposed on the interface. Equations 1.E69 and 1.E70 are the appropriate Reynolds lubrication equations for the present system. Whereas in the slipper-bearing problem H is known and P is determined by this equation, here H is unknown and P is a functional of H determined by Eq. 1.E67 (due to the surface tension and body forces). This distinction is associated with the presence of either a fixed solid boundary or a free gas-liquid interface. Equation 1.E69 is a generalization of the evolution equation presented by Sharma and Ruckenstein in the case of no slip on the solid and no external forces ($\beta_0 = \tau_0 = \Pi_0 = 0$).[Sharma1986]

The physical significances of the terms are revealed when Eqs. 1.E69 and 1.E70 are written in the original dimensional variables:

$$\mu\partial_t h + \partial_x\left[(\tau + \partial_x\sigma)\left(\tfrac{1}{2}h^2 + \beta h\right)\right] - \partial_x\left[\left(\tfrac{1}{3}h^3 + \beta h^2\right)\partial_x(\varphi\big|_{z=h} - \sigma\partial_x^2 h - \Pi)\right] = 0,$$

(1.E71)

$$\mu\partial_t h + \vec{\nabla}_1\left[(\vec{\tau} + \vec{\nabla}_1\sigma)\left(\tfrac{1}{2}h^2 + \beta h\right)\right] - \vec{\nabla}_1\left[\left(\tfrac{1}{3}h^3 + \beta h^2\right)\vec{\nabla}_1(\varphi\big|_{z=h} - \sigma\nabla_1^2 h - \Pi)\right] = 0.$$

(1.E72)

In many of the examples discussed below, all forces are isotropic in the horizontal dimensions x and y, and so only two-dimensional cases will be examined. Further, unless specified, only disturbances periodic in x will be discussed. Thus λ is the wavelength of these disturbances and $\frac{2\pi h_0}{\lambda}$ is the dimensionless wave number.

1.2.3. Constant shear stress and constant surface tension only

Suppose that the gas exerts a ''wind'' stress on an interface that exhibits a constant surface tension. In this case $\beta_0 = \Pi = \varphi = 0$, and τ and σ are constant. Equation 1.E71 becomes

$$\mu\partial_t h + \tau h\partial_x h + \tfrac{1}{3}\sigma\partial_x(h^3\partial_x^2 h) = 0. \qquad (1.E73)$$

In the absence of the surface tension ($\sigma = 0$), Eq. 1.E73 is a first-order nonlinear wave equation whose solutions are waves that travel in the direction of the shear and they steepen as they go. No instability is present. When the surface tension is present, the steepening is retarded. The numerical study of the nonlinear equation 1.E73 shows that the amplitude of its periodic solutions decays to zero with time.

One can investigate the behavior of small disturbances to the uniform film $h = h_0$ by perturbing it with a small disturbance h', periodic in x: $h = h_0 + h'$. If one substitutes this into Eq. 1.E73 and linearizes in primed quantities, then one has a linear stability

equation for h'. Since this equation has coefficients independent of t and x, one can seek separable solutions of the form

$$h' = h_0' e^{ikx+st}, \qquad (1.E74)$$

which is a complete set of "normal modes" that can be used to represent any disturbance. If these are substituted into the linearized disturbance equation, one obtains the following characteristic equation for s:

$$\mu s = -ik'\tau - \frac{\sigma}{3h_0}k'^4, \qquad (1.E75)$$

where $k' = kh_0$ is the nondimensional wave number and s is the growth rate of the perturbation. The amplitude of the perturbation, therefore, will decay if the real part of the growth rate Re(s) is negative and will grow if Re(s) is positive. Purely imaginary values of s correspond to translation along the x axis and give rise to traveling-wave solutions. Finally, zero values of s correspond to neutral, stationary perturbations. See figure 1.7.
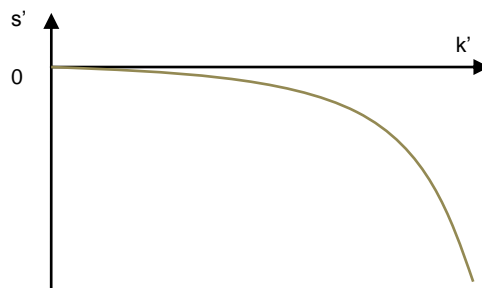
Figure 1.7: Characteristic equation given by Re(s) = $-\frac{1}{3h_0\mu}\sigma k'^4$. $s' = Re(s)\frac{h_0\mu}{\sigma}$ is the dimensionless growth rate of the perturbation with the dimensionless wave number k'. Negative growth rate corresponds to the decay of a perturbation; therefore there is no instability in the system.

1.2.4. Constant surface tension and gravity only

Consider perhaps the simplest film in which gravity is present and the surface tension is constant. Here $\beta_0 = \partial_x \sigma = \Pi = \tau = 0$ and $\overline{P} = \rho g h - \sigma \partial_x^2 h$, so that Eq. 1.E71 becomes

$$\mu \partial_t h - \frac{1}{3}\rho g \partial_x (h^3 \partial_x h) + \frac{1}{3}\sigma \partial_x (h^3 \partial_x^3 h) = 0. \qquad (1.E76)$$

In the absence of the surface tension, Eq. 1.E76 is a nonlinear (forward) diffusion equation so that no disturbance to $h = h_0$ grows in time. The surface tension acts through a fourth-order (forward) dissipation term so that no instabilities would occur for g > 0. If Eq. 1.E76 is linearized about $h = h_0$, the characteristic equation is

$$\mu s = -\frac{1}{3h_0}\left[\rho g h_0^2 + \sigma k'^2\right]k'^2. \qquad (1.E77)$$

This equation describes film leveling since s < 0; if at time t = 0 a small bump is imposed on the interface, Eq. 1.E77 governs how it will relax to $h = h_0$.

Equation 1.E76 also applies to the case of a film on the underside of a plate, the Rayleigh-Taylor instability of a thin viscous layer, as shown in figure 1.8. Here one replaces g by -g in Eq. 1.E77 and finds that

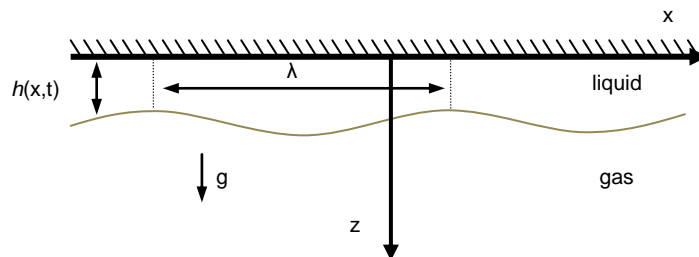$$\mu s = -\frac{1}{3h_0}\left[-\rho |g| h_0^2 + \sigma k'^2\right]k'^2. \qquad (1.E78)$$

Figure 1.8: Sketch of a liquid film lying on the underside of a horizontal plane and subject to Rayleigh-Taylor instability.

As shown in figure 1.9, the layer is linearly unstable if

$$k'^2 < k_c'^2 \equiv \frac{\rho g h_0^2}{\sigma} \equiv Bo, \qquad\qquad (1.E79)$$

i.e., if the perturbations are so long that the (nondimensional) wave number is smaller than the square root of the Bond number Bo, which measures the relative importance of the gravity and capillary effects. The value of k_c' is often called the (dimensionless) *cutoff wave number* for neutral stability.
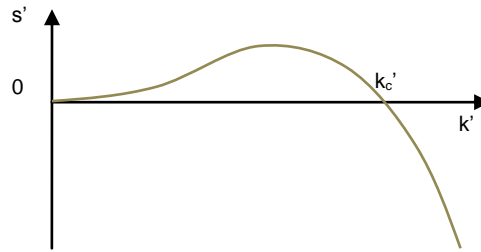

Figure 1.9: Characteristic equation given by 1.E77 for Bo=1. $s' = \frac{3s\mu}{\rho|g|h_0}$ is the dimensionless growth rate of the perturbation with the dimensionless wave number k'. Positive growth rate corresponds to the growth of the perturbation, whereas negative growth rate indicates decay. Therefore the unstable domain is 0<k'<k_c'.

1.2.5 Van der Waals forces and constant surface tension only

Van der Waals forces can be important when film thickness is in the range of several hundreds of angstroms. Such forces in general compete with the others of electrical or entropic origin (e.g., excess interfacial surface charge or electrical double layers), which exist on both longer and shorter scales than the van der Waals attractions do. At a given thickness of the layer, one or another of these can dominate. Only the h^{-3} forces will be considered here.

Dzyaloshinskii *et al.* derived a theory for the van der Waals attractions in which an integral representation is given for the excess Helmholtz free energy of the layer as a

function of the frequency-dependent dielectric properties of the materials in the layered system.[Dzyaloshinskii1959]

In the special case of a film with parallel boundaries and nonretarded forces in the absence of ionic species, $\varphi = \varphi_r + A' h^{-3}/6\pi$, where φ_r is the reference value for the body-force potential and A′ is the dimensional Hamaker constant. When A′>0, there is negative disjoining pressure and the corresponding attraction of the two interfaces (solid-liquid and liquid-gas) to each other. When the disjoining pressure is positive, A′<0, the interfaces repel each other.

Consider the negative disjoining pressure in a film with constant surface tension only, so that $\beta_0 = \partial_x \sigma = \Pi = \tau = 0$. When A′>0, instabilities occur, as shown below. When A′<0, the planar film persists. Equation 1.E71 then becomes [Williams1982]

$$\mu \partial_t h + \frac{A'}{6\pi} \partial_x \left(\frac{\partial_x h}{h}\right) + \frac{1}{3}\sigma \partial_x (h^3 \partial_x^3 h) = 0. \qquad (1.E80)$$

Linearization of Eq. 1.E80 around $h = h_0$ yields the characteristic equation

$$\mu s = \frac{k'^2}{h_0^2}\left[\frac{A'}{6\pi h_0} - \frac{1}{3}\sigma h_0 k'^2\right]. \qquad (1.E81)$$

It follows from Eq. 1.E81 that there is instability for A′>0, driven by the long-range molecular forces and the stabilization is due to the surface tension. The cutoff wave number k′$_c$ is then given by

$$k_c' = \frac{1}{h_0}\left(\frac{A'}{2\pi\sigma}\right)^{1/2}, \qquad (1.E82)$$

which reflects the fact that an initially corrugated interface has its thin regions thinned further by the van der Waals forces while the surface tension cuts off the small scales. Instability is possible only if 0<k′<k′$_c$, as seen by combining Eqs. 1.E81 and 1.E82:

$$\mu s = \frac{\sigma k_c'^2}{3h_0}\left(k_c'^2 - k'^2\right). \qquad (1.E83)$$

On the periodic domain of wavelength $\lambda = 2\pi/k$, the linearized theory predicts that the film is always unstable since all wave numbers are available to the system. In an experimental situation the film resides in a container of finite width, say L. The solution of the linear stability theory for $0 \leq X \leq L$ would show that only corrugations of a small enough wavelength could ''fit'' in the box, i.e. $\lambda < L$. No instability would then occur by this estimate, if $\frac{2\pi h_0}{L} > k_c{}'$. One sees from this theory that it is inappropriate to seek the critical thickness from the theory but only the critical thickness for a given experiment, since the condition depends on the system size L.

The evolution of the film interface as described by Eq. 1.E80 with the periodic boundary conditions and initial corrugation leads to the rupture of the film in a finite time. This breakup manifests itself by the fact that at a certain time the local thickness of the film becomes zero.

Several authors [Kheshgi1991, Mitlin1993, Sharma1993, Jameel1994, Mitlin1994] have considered the dynamics of thin liquid films in the process of dewetting of a solid surface. The effects important for a meaningful description of the process are gravity, capillarity, and, if necessary, the use of the generalized disjoining pressure, which contains a sum of intermolecular attractive and repulsive potentials. The generalized disjoining pressure is destabilizing (attractive) for the film for larger thicknesses and stabilizing (repulsive) for larger (smaller) thicknesses still within the range of several hundreds of angstroms.[Israelachvili1992] Equation 1.E71 may be rewritten, respectively, in the form

$$\mu \partial_t h - \frac{1}{3} \partial_x (h^3 \partial_x [\rho g h - \sigma \partial_x^3 h + \varphi]) = 0. \qquad (1.E84)$$

Different forms for the potential φ are encountered in literature. Teletzke *et al.* [Teletzke1988] expressed the generalized disjoining pressure as

$$\varphi = \sum_{i=1}^{4} a_i h^{-i}, \qquad (1.E85)$$

where a_i are coefficients determined by the specific intermolecular forces brought into consideration. In particular, the disjoining pressure corresponding to the van der Waals forces used by Williams and Davis [Williams1982],

$$\varphi = a_3 h^{-3}, \qquad (1.E86)$$

is obtained from Eq. 1.E85 for $a_3 \neq 0$, $a_i = 0$, $i \neq 3$. Mitlin [Mitlin1993] and Mitlin and Petviashvili [Mitlin1994] used the 6-12 Lennard-Jones potential for solid-liquid interactions

$$\varphi = a_3 h^{-3} - a_9 h^{-9}. \qquad (1.E87)$$

Polar and apolar (van der Waals) intermolecular interactions give rise to the generalized disjoining pressure expressed by

$$\varphi = a_3 h^{-3} - l_1 e^{-\frac{h}{l_2}}, \qquad (1.E88)$$

where l_1 and l_2 are dimensional constants [Williams1981, Sharma1993, Jameel1994] representing the strength of the repulsive and attractive forces, respectively, and decay lengths. Oron and Bankoff [Oron1997] used

$$\varphi = a_3 h^{-3} - a_4 h^{-4} \qquad (1.E89)$$

to model the simultaneous action of the attractive ($a_3 > 0$) long-range and repulsive ($a_4 > 0$) short-range intermolecular forces and their influence on the dynamics of the film.

Linearizing Eq. 1.E84 around $h = h_0$, one obtains

$$\mu s = -\frac{k'^2 h_0}{3}\left[\rho g + \frac{d\varphi}{dh}\Big|_{h=h_0} + \frac{\sigma k'^2}{h_0^2}\right]. \qquad (1.E90)$$

Kheshgi and Scriven [Kheshgi1991] studied the evolution of the film using Eq. 1.E84 with potential 1.E86 and found that smaller disturbances decay due to the presence of gravity leveling while larger ones grow and lead to film rupture. Mitlin [Mitlin1993] and Mitlin and Petviashvili [Mitlin1994] discussed possible stationary states for the late stage of solid-surface dewetting with potential 1.E87 and drew a formal analogy between the latter and the Cahn theory of spinodal decomposition [Cahn1960]. Sharma and Jameel [Sharma1993] and Jameel and Sharma [Jameel1994] followed the film evolution as described by Eqs. 1.E84, 1.E88 and concluded that thicker films break up, while thinner ones undergo ''morphological phase separation'' that manifests itself in creation of steady structures of drops separated by ultrathin flat liquid films. Similar patterns were also observed by Oron and Bankoff in their study of the dynamics of thin spots near the film breakup.[Oron1997]

Chapter 2.

Experimental techniques

2.1. Atomic force microscopy (AFM)

AFM belongs to the family of Scanning Probe Microscopy (SPM) instruments that are used to measure properties of surfaces. AFM is used to solve processing and materials problems in a wide range of technologies affecting the electronics, telecommunications, biological, chemical, automotive, aerospace, and energy industries. The investigated materials include thin and thick film coatings, ceramics, composites, glasses, synthetic and biological membranes, metals, polymers, and semiconductors. AFM is applied in the study of such phenomena as abrasion, adhesion, cleaning, corrosion, etching, friction, lubrication, plating, and polishing. By using AFM one can not only image the surface in atomic resolution but in addition AFM offers a variety of new contrast mechanisms which provide information on differences in friction, adhesion, elasticity, hardness, electric fields, magnetic fields, carrier concentration, temperature distribution, spreading resistance, and conductivity.

The main feature of AFM is a sharp tip on the end of a flexible cantilever which moves across the sample surface. The tip-sample interaction is monitored by reflecting a laser off the back of the cantilever into the split photodiode detector. In general, the physical nature and character of the tip-sample interaction are quite complicated, since they are defined by the tip characteristics, surface properties and surrounding medium. The main forces which contribute to exert the tip are: the force coming from mechanical contact of the tip end atoms with the sample (figure 2.1), the van der Waals force and the capillary force arising from condensation of water vapor in the contact area. The scanning force microscopes can be operated in many ways measuring different

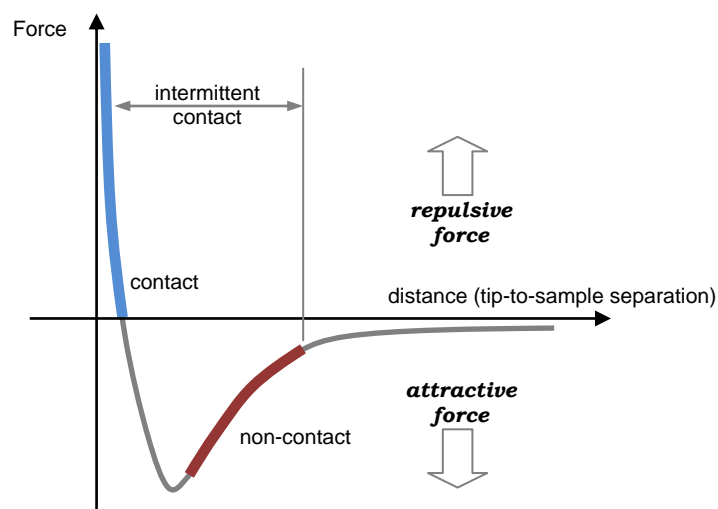interactions between the probe tip and the sample and using different types of detection schemes.

Figure 2.1: Intermolecular force curve.

The two most commonly used modes of operation are the contact mode AFM and the TappingMode™ or intermittent contact mode (IC-mode). The AFM measurements were taken in the *intermittent contact mode* (*IC-mode*) or *tapping mode*. In the IC-mode, the probe cantilever is driven to vibrate with high amplitude (10–100 nm) near its resonant frequency by a piezoelectric element. Since the contact time between the tip and the sample is two orders shorter as compared to *contact mode*, the IC-mode is less damaging and typically used for imaging topography of soft materials. Because of the high amplitude of oscillation, the tip propagates through regions of attractive (van der Waals, electrostatic) and repulsive forces in a single oscillation cycle (figure 2.1). The amplitude and the frequency of the cantilever decrease while approaching the sample surface. Upon scanning, these parameters (and, hence, the force gradient) are maintained constant at a set-point level by the feedback loop. It is achieved by adjusting the tip-sample distance. The feedback signal and the phase lag of the cantilever oscillation relative to the driving oscillation are displayed yielding height and phase images, respectively

AFM experimental setup. A multimode AFM instrument or NanoScope IV-D3100 (Digital Instruments, Santa Barbara) was used for sample characterization, operating in the tapping mode. Silicon tips with a radius of 10-20 nm, spring constant of 30 N/m

and resonance frequency of 250-300 KHz were used. The amplitude set-point ratio (A_{sp}/A_0) was in the range of 0.99-0.85 for the "light" tapping mode. All measurements were taken at ambient conditions (temperature 21 ± 2 °C; relative humidity 50-70 %).

2.2. Ellipsometry

Ellipsometry is a versatile and powerful optical technique for the investigation of dielectrical properties (complex refractive index or dielectrical function of thin films). It has applications in many different fields, from semiconductor physics to microelectronics and biology, from basic research to industrial applications. Ellipsometry is a very sensitive measurement technique and provides unequalled capabilities for thin film metrology. As an optical technique, spectroscopic ellipsometry is non-destructive and contactless.

Ellipsometry measures two of the four Stokes parameters, which are conventionally denoted by Ψ and Δ. Ellipsometry measures the change in polarization of monochromatic light reflected upon a flat surface with a single or multiple layers on it. The polarization state of the light incident upon the sample may be decomposed into the s and a p components (the s component is oscillating perpendicular to the plane of incidence and parallel to the sample surface, and the p component is oscillating parallel to the plane of incidence). The amplitudes of the s and p components, after reflection and normalized to their initial value, are denoted by r_s and r_p, respectively. Ellipsometry measures the ratio of r_s and r_p, which is described by the fundamental equation of ellipsometry:

$$\frac{r_p}{r_s} = \tan \Psi \, e^{i\Delta} \qquad (2.E1)$$

Thus, $\tan \Psi$ is the amplitude ratio upon reflection, and Δ is the phase shift (difference). The measurement of Δ and ψ at one wavelength and one angle of incidence allows determining two real parameters such as the refractive index and thickness. For a given multilayer interfaces it is appropriate to do ellipsomentry measurements after

each stage of film preparation. Since ellipsometry measures the ratio (or difference) of two values (rather than the absolute value of either), it is very robust, accurate, and reproducible. For instance, it is relatively insensitive to scatter and fluctuations, and requires no standard sample or reference beam.

Ellipsometry experimental setup. Ellipsometric measurements were carried out on a rotating-analyzer ellipsometer SE400 (SENTECH Instruments GmbH, Germany). The instrument uses a He-Ne laser as the light source (λ = 632.8 nm) and is equipped with focusing optics collimating the laser beam in a 30 µm size spot on sample surface and a XY-stage for mapping measurements. The incident angle was fixed at 70°.

The measurements were performed for chapter 3. The thickness of the polymer films was calculated using a three-layer model: $Si-SiO_2$ / polymer / air. The ellipsometric parameters were fitted using the Elli program developed by Optrel GBRmBH (thickness of SiO_2 = 1.8 ± 0.1 nm; n_{SiO_2} =1.4598; n_{Si} = (3.858 − i 0.018); n_{air}=1;

2.3. Electrical measurements

Electrical measurements were performed in a specially equipped room. Electrical measurements for chapter 5 were followed using 18-finger gold micro-electrodes (step height 50 - 100 nm, width 500 - 1000 nm, separation 500 - 1000 nm) were fabricated by photo-lithography on Si-wafer with an insulating SiO_2 layer (~300 nm) and probe head with tungsten needles for contact realization (figure 2.2). Electrical measurements were performed with a Keithley 2400 Source-Measure Unit.

The Model 2400 Source-Measure solution is a 20W instrument that allows sourcing and measuring voltage from ±5 µV (sourcing) and ±1µV (measuring) to ±200 V DC and current from ±10 pA to ±1 A. All data was automatically transferred to the computer and processed by the LabVIEW™ program. Using Keithley 2400 Source-Measure Unit the voltage from 0.1 V to 1 V with step 0.1 V was applied. In each step 20 data points were recorded and the average value of the current corresponding to a certain voltage was calculated.
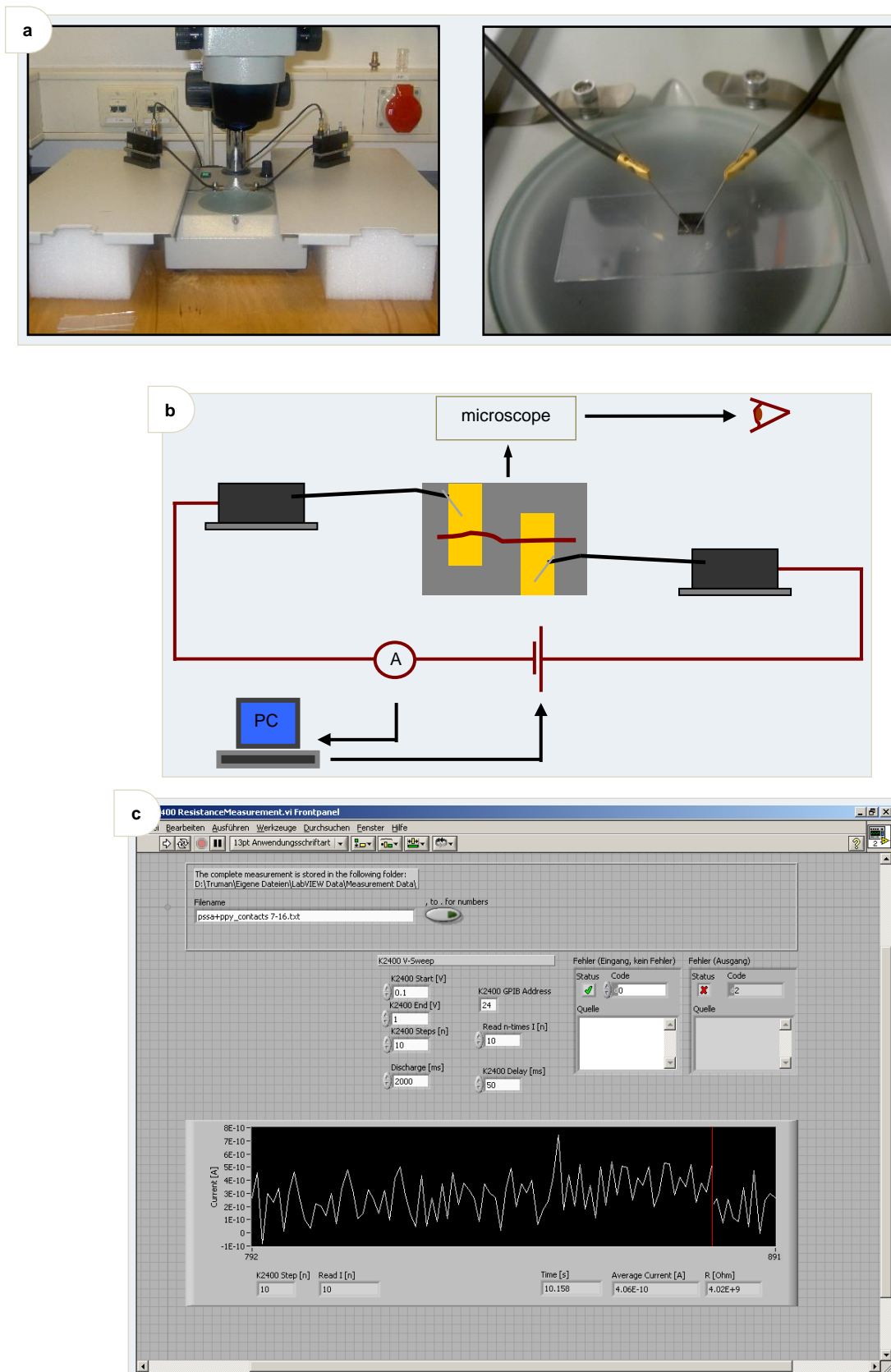
Figure 2.2: (a) Photo of the set up for electrical measurements; (b) diagram of the measurement realization; (c) screenshot of the LabVIEW™ software.

2.4. Optical microscopy

The past decade witnessed an enormous growth in the application of optical microscopy for micron and submicron level investigations in a wide variety of disciplines.[Herman1993, Davidson] Rapid development of new fluorescent labels accelerated the expansion of fluorescence microscopy in laboratory applications and research. Advances in digital imaging and analysis also enabled microscopists to acquire quantitative measurements quickly and efficiently on specimens ranging from photosensitive caged compounds and synthetic ceramic superconductors to real-time fluorescence microscopy of living cells in their natural environment. Optical microscopy, with the help of digital video, can also be used to image very thin optical sections, and confocal optical systems are now in operation at most major research institutions.

In the optical microscope, when the light from the microscope lamp passes through the condenser and then through the specimen (assuming the specimen is a light absorbing specimen), some of the light passes both around and through the specimen undisturbed in its path. Such light is called direct light or undeviated light. The background light passing around the specimen is also undeviated light. Some of the light passing through the specimen is deviated when it encounters parts of the specimen. Such deviated light is rendered one-half wavelength or 180 degrees out of step with the direct light that has passed through undeviated. The one-half wavelength out of phase, caused by the specimen itself, enables this light to cause destructive interference with the direct light when both arrive at the intermediate image plane located at the fixed diaphragm of the eyepiece. The eye lens of the eyepiece further magnifies this image which finally is projected onto the retina or the film plane of a camera.

What happens is that the direct or undeviated light is projected by the objective and spread evenly across the entire image plane at the diaphragm of the eyepiece. The light diffracted by the specimen is brought to focus at various localized places on the same image plane, where the diffracted light causes destructive interference and

reduces intensity resulting in more or less dark areas. These patterns of light and dark are what we recognize as an image of the specimen. Because our eyes are sensitive to variations in brightness, the image becomes a more or less faithful reconstitution of the original specimen.

Fluorescence microscopy.[Bradbury1996] In most cases, a component of interest in the specimen is specifically labeled with a fluorescent molecule called a fluorophore. The specimen is illuminated with light of a specific wavelength (or wavelengths) which is absorbed by the fluorophores, causing them to emit longer wavelengths of light (of a different color than the absorbed light). The illumination light is separated from the much weaker emitted fluorescence through the use of an emission filter. Typical components of a fluorescence microscope are the light source (xenon arc lamp or mercury-vapor lamp), the excitation filter, the dichroic mirror (or dichromatic beamsplitter), and the emission filter (see figure 2.3). The filters and the dichroic are chosen to match the spectral excitation and emission characteristics of the fluorophore used to label the specimen. In this manner, a single fluorophore (color) is imaged at a time. Multi-color images of several fluorophores must be composed by combining several single-color images.
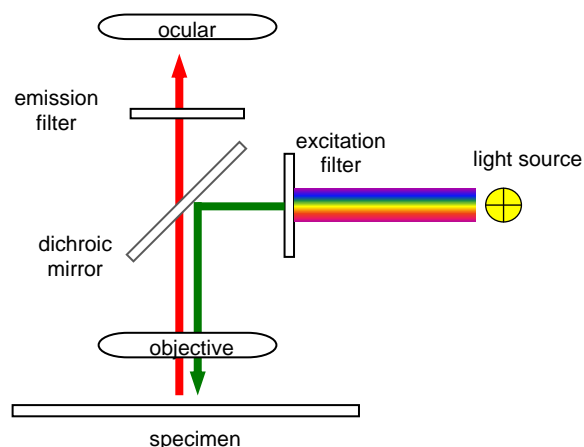
Figure 2.3: Fluorescence filters.

Most fluorescence microscopes in use are epifluorescence microscopes (i.e. excitation and observation of the fluorescence are from above (epi–) the specimen).

These microscopes have become an important part in the field of biology, opening the doors for more advanced microscope designs, such as the confocal microscope and the total internal reflection fluorescence microscope.

For fluorescence studies, an inverted microscope (Zeiss LSM META laser lines: 458, 488, 514, 543, 633 nm), equipped with a sets of long distance objectives and standard fluorescence filter sets, was used (Carl Zeiss, Germany). Images were taken by a cooled CCD camera (Orca ER, Hamamatsu Photonics, Germany) and processed by imaging software.

The principle of **confocal imaging** was patented by Marvin Minsky in 1957 and aims to overcome some limitations of the traditional wide-field fluorescence microscopes.[Minsky1957] In a conventional (i.e. wide-field) fluorescence microscope, the entire specimen is flooded with light from a light source. All parts of the specimen in the optical path are excited and the resulting fluorescence is detected by the microscope photodetector or camera as a background signal. In contrast, the confocal microscope uses point illumination and a pinhole in the optically conjugate plane in front of the detector to eliminate the out-of-focus information - the name "confocal" stems from this configuration. As only the light produced by the fluorescence very close to the focal plane can be detected the image resolution, particularly in the sample depth direction, is much better than that of the wide-field microscopes. However as much of the light from the sample fluorescence is blocked at the pinhole, this increased resolution is at the cost of decreased signal intensity so long exposures are often required.

Chapter 3.

Nanostructures obtained the using contact line movement approach

3.1. Introduction

There has been continuous research interest in the three-phase contact line systems, where the solid, liquid, and gas phases have common border. In such systems deferent physical processes may take place, i.e. wetting/dewetting, interfaces instabilities, internal flows in liquid phase, solute adsorption/deposition, etc. Superposition of those processes determines the behavior of the system. Therefore it is important to determine the role of each process, especially on various length scales.

The wettability of a liquid is highly dependent on the heterogeneity of the surface with respect to both morphology and chemistry, studies of the microscopic features of the contact line will be able to reveal the origins of the wetting and dewetting behavior.[Xu2004, Xu2005] Also, it will help us to understand the properties of liquids at small dimensions and may have an impact on applications such as high-resolution printing technologies, microfluids, nanofluids, electronic devices and biomaterials.[Joanny1984, Raphael1989, Golestanian2001, Golestanian2004, Ramos2003, Nikolayev2005, Seemann2005, Gonuguntla2004, Kumar1995, Marsh1993, Chow1998, Vannimenus2002]

There is a history of microscopy research on contact lines with regard to both morphology and dynamic evolution. Studies were conducted with different methods on various length scales, and efforts were made to improve the spatial resolution so that more details about the contact line can be explored. Optical imaging techniques were widely used to study the morphology of the contact line and its temporal relaxation on length scales ranging from centimeters [Huppert1982, Ondarcuhu1991] to millimeters [Shmuylovich2002, Cachile2002, Poulard2003, Cachile2002-2]. To explore the microscopic feature of contact lines down to even smaller length scales, other microscopy methods, such as laser scanning cofocal

fluorescence microscopy, atomic force microscopy (AFM), and scanning electron microscopy were utilized.[Vyawahare2006] Such studies drove the length scale of observation down to the range of micrometers. Because of the influence of surface heterogeneity on liquid wettability, research was also conducted to study the effect of the nanometer-scale surface roughness on the wetting behavior, in which contact line pinning with respect to nanometer-size heterogeneity was discussed.[Ramos2003, Ramos2006] Details of the contact line at the single-molecule level, for example, molecular motion in the precursor film of wetting, viscous polymeric liquid, by AFM were reported.[Xu2004, Xu2005] Because of the fluidity and softness of liquids, the morphology of the contact line on a small length scale is hard to determine, and tracer substances were used as probes of the contact line shape. For example, colloidal particles and fluorescent DNA samples were used in investigations, and the morphology of these tracing substances was studied to illustrate the morphology and temporal evolution of the contact line.[Shmuylovich2002, Deegan1997, Deegan2000, Deegan2000-2] However, due to the intrinsic dimension of the particles, the local morphology of the contact line may not be fully reproduced, especially on length scales smaller than that of the tracing particles.

Self-assembly of polymers and colloidal particles attracted a lot of attention as the result of the growing importance of colloidal patterning for photonic, electronic, and magnetic applications, as well as a surging interest in biomacromolecular self-organization and recognition. An ordered colloidal particle or polymer arrays serve as a platform for developing nanoscale devices whose functionalities are enabled by the physical (i.e., optical, electrical, and magnetic) properties and their arrangement. For example, an area of increasing interest is one-dimensional (1D) nanoparticle arrays because they provide a model system to study the transport phenomena [Maier2003, Shipway2000, Simon1998] between nanoparticles in addition to their potential technological applications, such as chemical sensors [Favier2001] and lithography masks [Henrichs1999]. Ordered arrangements of nanoparticles on templates such as block copolymer scaffolds and along crystal step edges were also demonstrated.

Various intriguing structures from rings [Deegan1997, Deegan2000, Deegan2000-2] to hexagonal networks [Maillard2001] to dendrites [Haidara2001, Mougin2002] over broad systems from colloidal particles [Harris2007, Shmuylovich2002] to polymers [Fang2006, Smalyukh2006, Maeda2000] were observed on

substrates of different chemistry and topography upon the moving contact line. Remarkably enough, self-organization of substrates with completely different size (from nano- to macroscopic), shape (spherical or rod-like), flexibility and/or chemical nature (inorganic colloids and organic polymer molecules) sometimes results in very similar types of morphologies. On the contrary, the same substrate can give a range of morphologies (stripes, tree-like, rim structures, rings) under different moving contact line conditions. The formation of the same general types of morphologies for very different objects can be explained by the dominating role of the underlying self-organization mechanisms. It should be, however, mentioned that the nature and, especially, the size of the elementary units being self-assembled, defines the exact characteristic size of the resulting structures. For example, tree-like structures formed upon the self-assembly of microspheres and tree-like structures formed by polymer molecules looks very similarly, however the sizes of the resulting structures differ over few orders of magnitudes.

Processes underlying the patterns formation are very diverse and complex. Not all of them are fully understood or even known, since they are governed by a complex superposition of a number of forces. Among the most important and studied processes underlying the patterns formation are the following ones:

(1) Coffee ring formation process.[Deegan1997] These structures are formed by the capillary flow, where the pinned contact line of an evaporating droplet results in the formation of an outward capillary flow to compensate for the loss of the solvent near the edge of the contact line which continuously carries and deposits the solute toward the droplet perimeter and consequently forms a single ring like a stain near the initial contact line (see figure 3.1a).

(2) Process of periodic pattern formation, induced by Benard-Marangoni convection, where the evaporation of solvent at the liquid-air interface lowers the surface temperature and results in a temperature gradient perpendicular to the solid surface.[Maillard2001, Nguyen2002] As a result, the surface tension gradient established in the liquid film induces the Benard-Marangoni instabilities to form the patterns (see figure 3.1b).

(3) Molecular combing. Process of elongation of macromolecules by surface tension, where continuous receding of the contact line at the air-liquid interface stretches macromolecules by imposed interfacial hydrodynamic forces (see figure 3.1c).[Bensimon1994]
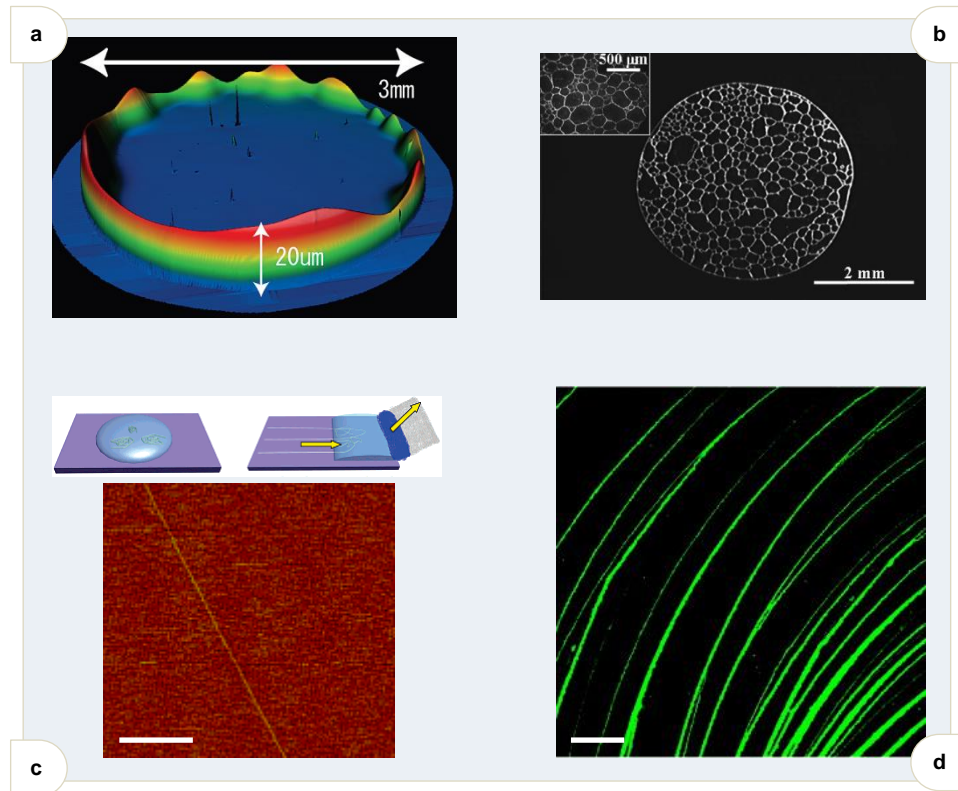

Figure 3.1: The most studied processes underlying the patterns formation:
(a) Coffee ring formation process - the polymer film profile formed after butanol-PDMA droplet dried up; [adopted from Kajiya2009]
(b) Process of periodic pattern formation, induced by Benard-Marangoni convection - reflected-light microscopy image of the connected polygonal network formed by particles left as residue after the drop evaporates; [adopted from Nguyen2002]
(c) Molecular combing - AFM image of DNA strand prepared by molecular combing (scale bar – 1 µm); [adopted from Zhang2005]
(d) Process of multiple-ring pattern formation – fluorescent microscopy image of pattern formed after a droplet of water solution of DNA-colloidal particles dried up (scale bar – 300 µm). [adopted from Zhang2008]

(4) Process of multiple-ring pattern formation. This process is induced by the oscillatory motion of the contact line.[Shmuylovich2002, Adachi1995, Maeda1999, Maeda2000, Takhistov2002, Maheshwari2008] Adachi *et al.* proposed that the competition between the friction and surface

tension at the contact line results in the stick-slip motion of the receding contact line to form consecutive multiple rings (see figure 3.1d).[Adachi1995]

When a liquid phase containing nonvolatile materials, such as colloidal particles and polymers, moves on a substrate, it leaves a film of deposit on the substrate. This is a commonly observed phenomenon in our daily life but involves many unsolved problems and has attracted a resurging interest recently in both the scientific and industrial communities. An important problem here is how to control the shape and properties of the final deposit left on the substrate. One of the critical factors that govern the drying process is the movement of the contact line, whether it is pinned or not.

Goals of this chapter:

- *Development of advanced deposition techniques for obtaining highly oriented, with known orientation, polymeric nanostructures by utilizing the moving three-phases (solid-liquid-gas) contact line;*
- *Identification of the key factors of the nanostructures formation.*

3.1.1. Micro- and nanostructures formation in drying drops

Robert D. Deegan developed and experimentally tested a theory for the formation of rings in drying drops.[Deegan1997, Deegan2000] A common manifestation of this phenomenon is the brown ring left when a drop of coffee dries. He found that contact line pinning and evaporation are sufficient conditions for ring formation. Since these are common and generic conditions, ring formation often occurs whenever a liquid with solid constituents evaporates. The ring forms because the contact line cannot move during the whole process of drying; the contact line is pinned at the very early stage of drying, and it leaves a ring-like deposit. Deegan explained that the contact-line pinning is caused by the accumulation of solute in the vicinity of the contact line, and the formation of the ring-like deposit is due to the solute transport by the outward capillary flow.

When evaporation removes liquid from around the contact line, a flow develops to keep the substrate wet up to that point. The solute in the drop is dragged to the contact

line by this flow, where it accumulates to form the ring-like deposit that remains after all the liquid evaporates. The substrate by itself cannot keep the contact line pinned indefinitely. In Refs. [Deegan1997, Deegan2000] it is assumed that the accumulation of solid components at the contact line perpetuates the pinning of the contact line. Uncomplicated constraints produce a simple structure - a ring.

The one-ring pattern formation process requires the contact line to be pinned on to the substrate at a nonzero contact angle for the entire cycle, while evaporation of the solvent, which is maximum at the contact line, transports the solute outwards and towards the pinned contact line. This causes the formation of the ring like a stain at the outer regions of the drop. At the same time, sustained evaporation and the pinning of the contact line causes the drop height to continually decrease. Ultimately when the meniscus at the center of the original drop comes in contact with the solid substrate, the meniscus ruptures at that point and almost instantaneously the entire drop dewets and the stain-formation process is completed. The notable feature of this process is the almost 100% transfer of the solute to the contact line, pointing to the pinning of the contact line at its initial position throughout the entire cycle.

On the other hand, there are cases when the contact line does move at a certain stage of drying. In dilute colloidal suspensions and DNA solutions, it has been reported that the contact line shows a stick-slip motion.[Deegan2000, Shmuylovich2002, Maheshwari2008, Zhang2008] When this happens, the pattern of the deposit varies, multiple ring and other complex patterns were observed. The stick-slip motion is considered to be caused by the competition between the capillary force, which pulls the contact line inward, and the pinning force because of the accumulation of solute in the vicinity of the contact line. The contact line motion is also reported for a droplet having a large contact angle ($\theta \approx 90^{\circ}$).[de Gans2004, Kajiya2006, Fukai2006, Kaneda2008] In this case, the contact line motion is observed at a certain period of the overall duration of the process of drying: when drying starts, the contact line remains in its place for a while, then starts to recede, and then stops again. The multi-ring pattern requires repeated pinning and depinning of the contact line. While the contact line recedes, it does not leave any deposit behind. These one-ring and multi-ring patterns are perpendicularly aligned to the meniscus (contact line).

Zhang *et al.* observed multiple-ring pattern that spontaneously emerged upon evaporation for DNA solutions on the microscope cover slips.[Zhang2008, Maheshwari2008] With time-elapsed microscopic observation, they demonstrated that DNA precipitation dynamics as well as the resulting stain patterns strongly depended on the initial DNA concentration. At high initial DNA concentrations, DNA ~50 mg/mL, periodic multiple-ring patterns were observed. At initial DNA concentrations, DNA ~10 mg/mL, multiple rings with less periodicity were observed, where the number of rings decreased considerably and the space between the adjacent rings became much wider. At low initial DNA concentrations, the drying behavior appeared to resemble the evaporation of a pure water droplet with a continuously receding contact line, resulting in a structureless concentrated DNA residue stain. By recording the position of the contact line with time, Zhang observed that the contact line receded with a pinning-depinning cycle, which periodically generated new contact lines with trapped DNAs via an internal microstagnation flow. The cycle of the pinning-depinning steps in the entire evaporation process determined the number of the resulting stain rings at different DNA concentrations.

A drop of soluted 100 nm sulfate-terminated polystyrene microspheres forms different structures on mica during drying.[Deegan2000-2] At the highest concentration (initial volume fractions ~1%) Deegan found multiple ring structures with rings coated by multiple layers of microspheres. At 0.25% and 0.13% a grid-like pattern appears. It can exist concurrently with or separately from other patterns at these concentrations. The production of the grid appears to be an unstable version of the single-layer production. Direct observation of the contact line shows that parts of it move steadily and that the parts between these move in a stick-slip fashion. The steady moving segments lay down the radial lines of the grid and stick-slip segments produce nothing when moving and a ring when at rest; the combination of the radial lines and the rings forms a grid. Finally, at the concentration of 0.063% another new mode appears in which radial spokes are produced.

The grid appears when the number of holes times their average size becomes comparable to the circumference of the drop. Unlike the arch creation period in which the majority of the contact line is pinned, large portions of the contact line become free

to move. At high concentrations this motion is heavily constrained by the accumulation of particles, and is therefore erratic. Half-formed arches develop when a small portion of the contact line is temporarily pinned. However, for lower concentrations the contact line organizes itself into a series of cusps that emit particles. This deposition appears to be a release of particles controlled, so that there is no net accumulation at the contact line. During this type of motion, radial lines are formed. The ability of the contact line to do this is thwarted at higher concentrations because the influx of particles is overwhelming. As the concentration is lowered and fewer particles reach the contact line per unit time the ejection process can handle all the particles that arrive. This process leads to the formation of structures aligned perpendicular to the meniscus.[Deegan2000-2]

3.1.2. Stripe-like micropatterns

The stripe-like micropattern is, probably, the most important type of morphology for the present thesis tasks and is therefore discussed in detail.

Several groups reported stripe-like micropattern formation in transferred surfactant films, which can be categorized into two types.[Raudino2007, Gleiche2000, Mahnke1999, Pignataro2002]

The <u>first</u> type is based on stripe-like "defects" found in lipid monolayers prepared near pK, or those transferred near the phase transition from the liquid-expanded to liquid-condensed phases.[Raudino2007, Gleiche2000, Moraille2002, Spratte1994, Kovalchuk2003, Yaminski1997] The pattern formation mechanism is explained as periodic oscillations of the contact angle and meniscus height of the water subphase on the substrate during the Langmuir-Blodgett transfer of the films.[Mahnke1999] These dewetting patterns aligned parallel to the meniscus are interpreted in terms of substrate-mediated condensation at the three-phase contact line. By filling the periodically separated gaps with organic and inorganic filling materials, these channels show a potential application in lithographic templates.[Lenhert2004, Lu2002]

More recently, Pignataro *et al.* reported that a lipid monolayer in the liquid-condensed phase forms periodic defects perpendicular to the meniscus, when the film is

transferred at low temperature, where is <u>second</u> type of pattern.[Pignataro2002] The obtained patterns suggest a different mechanism of pattern formation; however, further physical characterizations seem to be necessary to determine the dominant physical parameter.

As a general feature, under certain limits, high speed and low lateral pressure drive the pattern toward periodic structures perpendicular to the transfer. In contrast, at a lower speed and/or higher pressure, parallel structures are favored. Between these two regions, there is a transition zone where both parallel and perpendicular features coexist.[Gleiche2000]

These two types of patterns, aligned parallel and perpendicular to the contact line, are typical structures which can be obtained during the contact line movement. For example, they are observed during the drop drying on a solid surface or at the deep coating techniques application.

Przerwa *et al.* showed what lifting of smooth non-patterned mica plate from a suspension of microspheres allows the controlled particle deposition.[Przerwa2004] In this case particles are assembled into stripes oriented parallel to the meniscus. The stripes are distributed quite regularly on the plate. Przerwa suggested that assembly of microspheres into a stripe-like pattern is due to the capillary forces acting on the microspheres crossing the water-air interface. The quality of particle assemblies and particle assembly distribution are strongly affected by the particle-plate adhesion forces (microspheres should be weakly adsorbed to allow their sliding or rolling on the plate) and by the shape of the water surface in the vicinity of the plate where microspheres crossing the water-air interface. The concentration of microspheres in suspension also affects the formation of adsorbed particle assemblies. The best results were obtained for concentrations of microspheres equaling 10 mg/mL and rates (with which the plate crossed the liquid-air interface) of 13.8 μm/s for particles of 1 μm size.

Liu *et al.* showed what perpendicular (to the meniscus) aligned structures were formatted after a droplet of polymer solution would evaporate.[Liu2008] This process carried out on surfaces of homopolymer thin films of PS and PMMA. The morphology of the polymer molecules after droplet drying deposition of PVP solution with different concentrations exhibits similar structures. The stripe-like morphology is observed - the structures of PVP after drying consists of buttons connected by ribbons generally

oriented in the direction of the contact line movement. The dimensions of the buttons and ribbons gradually changed when the observation region shifted from near the edge of the original droplet to the center region. For example, the buttons are about 3-8 nm thick with the diameter of 20-40 nm, and the ribbons are 1-2 nm thick and 10-15 nm wide.

Liu suggested what using water-soluble polymers as tracing substances allows the observation of the morphology of the three-phase contact line and its temporal evolution on a much smaller length scale, compared with the conventional methods of microspheres. The current study demonstrates that the shape of the contact line is modified by nanoscale surface structures and its pinning and depinning occur in a localized manner, and the observation of polymeric precipitates after droplet evaporation shows that the above process can take place on a length scale down to at least 20 nm. In the meantime, the results exhibit a new way to create surface patterns, which can be guided by a predetermined structure. Patterns formed by the polymeric precipitates after evaporation is a nonequilibrium process, and the patterns that are formed are highly dependent on the rate of the contact line movement.

It can be concluded that patterns formation processes induced by the moving contract lines are subjects of intense investigations. Such studies, on the one hand, are of theoretical interest and will help understand the liquid behavior near the contact line, but on the other hand, can provide a novel prospective way to fabricate nanometer-scale objects, especially those with large aspect ratios. It can be envisioned that other nanoobjects made of different materials, for example, functional polymers, may be fabricated in a similar way. This fabrication can be, in principle, conducted on-sites, for example, on pre-patterned functional surfaces such as nanoelectrodes.

3.2. Materials

Polystyrenesulfonic acid (M_W's 6 900 000 g/mol, PDI=1.3; 500 000 g/mol; 200 000 g/mol; 30 000 g/mol) was purchased from Polymer Standards Service, Mainz. Other chemicals were purchased from Aldrich.

Preparation of polyelectrolyte solutions. PSSA samples of different M_W of 6 900 000, 500 000, 200 000, 30 000 g/mol were used in this study. PSSA samples were dissolved for 2 days in deonized water (18 MΩ/cm) at room temperature in a shaker. The highest concentrations of PSSA solutions were obtained by direct dissolution of the required amount of PSSA in water. All other concentrations were obtained by the respective dilution of the solution with the highest concentration.

For reliability and reproducibility of results it is essential to molecularly dissolve polyelectrolyte molecules. It was found that for rather high MW polyelectrolytes the dissolution is a slow process and takes weeks.

It is important to note that PSSA solutions dissolved for a short time, such as for a few hours may look as "true" solution of molecularly dissolved PSSA. The membrane filtration cannot be applied to separate a "true" solution from undissolved clusters because of the exceedingly high M_W of the samples. On the other hand, incomplete dissolution strongly affects (decreases) the real concentration of the molecularly dissolved PSSA. Figure 3.2 shows an AFM image of such a sample of PSSA of M_W = 6 900 000 g/mol dissolved with stirring for 12 hours. Besides the molecularly dissolved chains there are several large aggregates deposited. It is clear that in such incompletely dissolved samples the predominant quantity of the polymer is present in the aggregated, but not in the molecularly dissolved state.

After the preparation all water solutions of PSSA could be stored for a long time, but require shaking for several hours (depending on the concentration) before use.
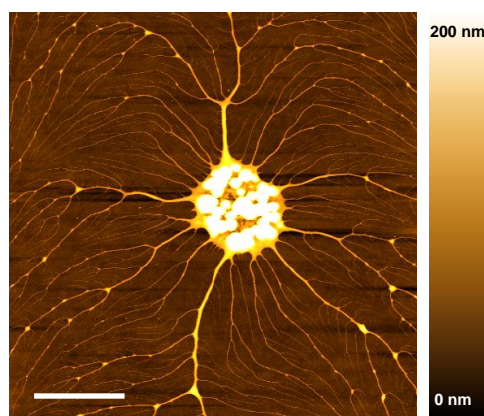
Figure 3.2: AFM image of an undissolved cluster of PSSA molecules. Scale bar - 4 μm.

Fabrication of PDMS stamps. Covering glasses (2 cm x 8 cm) were chosen as substrates for experiments of the patterns formation. Each glass slide was washed with chlorophorm, ethanol and then with water followed by drying in the nitrogen flow. Dow Corning WL-5351 photopatternable spin-on silicone from the Dow Corning corporation was spun coated on covering glass. To this end, 500 μL of WL-5351 was deposited on the glass slide and in 30 seconds, when the viscous solution would spread on the entire surface, rotation was started. The following optimal conditions were determined: speed - 2000 rpm, time - 30 seconds, acceleration - 1000 rpmm. Following spincoating the samples were placed under UV light (254 nm wave length) for 30 min, radiation dose ~1000 J/cm^2, and then heated to 150 °C in air for 30 min to complete the curing. The above procedure allowed obtaining transparent hydrophobic films with a thickness of several micrometers on the glass substrate. Figure 3.3 shows atomic force microscopy image (AFM) and the data of water contact angles of the resulting surface.
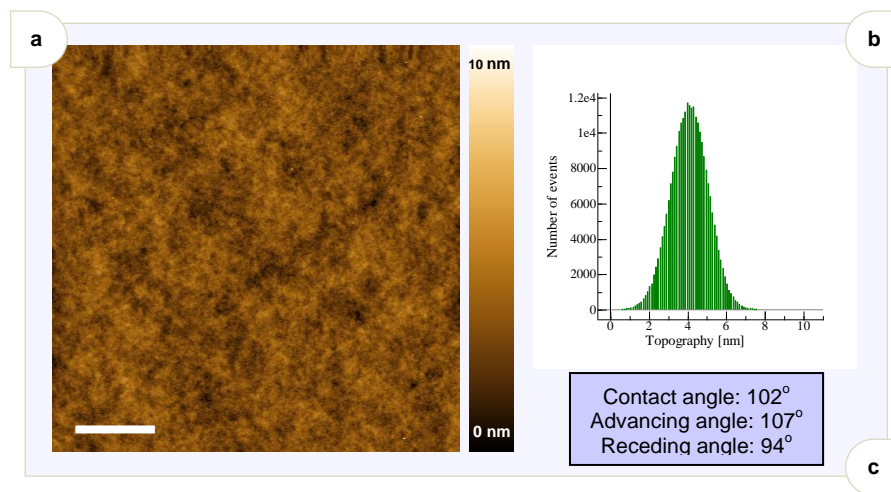
Figure 3.3: (a) AFM image and (b) the topography data of the surface covered by WL-5351 material; scale bar - 2 μm; (c) the wetting properties (for water) of that surface.

The usage of WL-5351 material as the surface modifier presented several advantages. First of all, a flat surface covered by WL-5351 has a high wetting contact angle for water, equal to ~100°. Also WL-5351 can be easily spincoated on glass or silica substrate without the formation of any dewetting areas, surface defects. Independently of the substrate roughness, the resulting surfaces have the roughness of several

nanometers. This point is crucial in terms of the surface topology requirements for further adsorbents visualization. WL-5351 can be cured by temperature or/and by UV light. After fabrication the samples can be stored on air at room temperature, the properties of as-prepared samples are preserved for several weeks and the possible deviations of the surface properties are low enough and can be neglected for the purpose of this thesis.

3.3. Results and discussion

3.3.1. Guided movement of the droplet.

When a drop of PSA solution is placed on a surface with the aid of a capillary it forms a meniscus at the solid-liquid interface. It is essential that the drop is still connected to the capillary. Due to the hydrophobicity of the surface and weak interactions between the liquid and the solid on the one hand, and because of strong interactions between the liquid and the capillary on the other, it is possible to move the drop of liquid along the surface just by moving the capillary (see figure 3.4, figure 3.5a).

On the surface the moving drop may be divided into two moving contact lines (the lines where the solid, liquid and gas phases meet): the advancing and the receding moving contact lines.
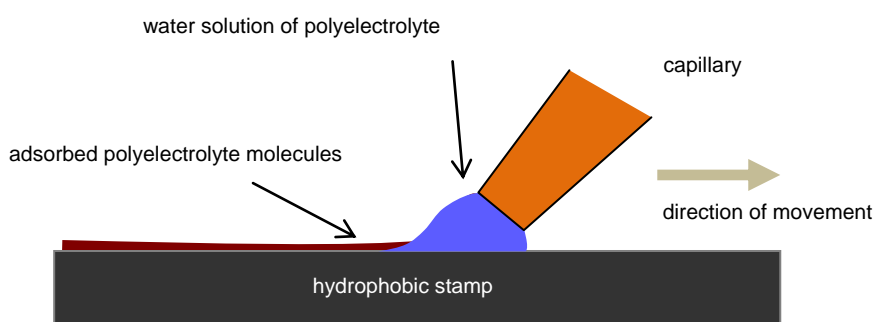
Figure 3.4: Sketch of droplet followed by capillary.

The influence of the surface tension forces on the drop of liquid is such that its volume is kept to the minimum and the droplet doesn't spread on the hydrophobic surface. During the movement, the advancing contact line is pushed forward, whereas

the receding contact line is pulled to the bulk of the drop. Depending on the viscosity of the solution, the speed of the movement and the polymer-surface interactions, the distortion of the moving droplet can reach different values. Droplets of low concentration solutions as well as droplets of pure water, moving at the speeds of several microns per second, remain almost undistorted in comparison with free standing droplets. For concentrated solutions and high moving speeds significant distortions were observed, especially for the receding contact line. Over the course of such experiments the droplet would sometimes lose contact with the capillary because of the high movement speed and in such cases the droplet would dry where it stopped (see figure 3.5b). In other instances the droplet doesn't lose contact with the capillary, but the receding contact line stops, which leads to thin film deposition on the surface while the droplet movement continues (see figure 3.5c).
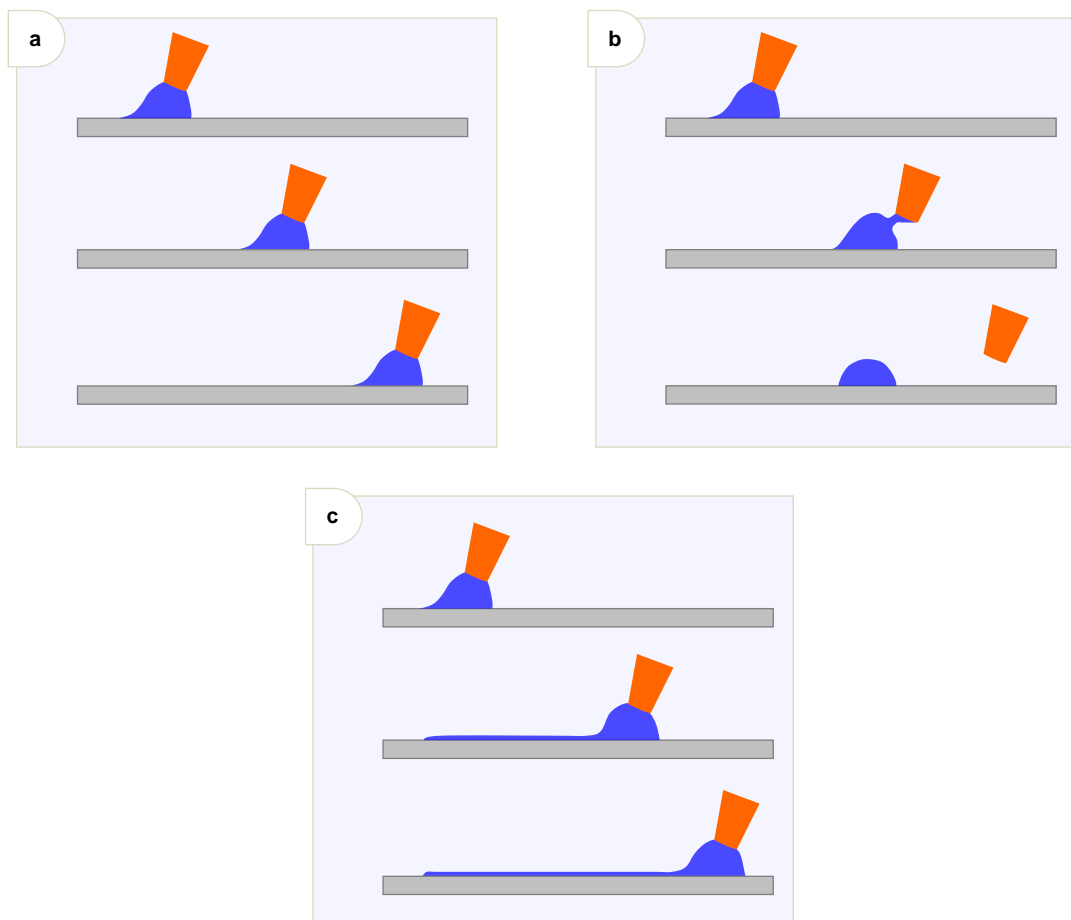
Figure 3.5: Sketch of the moving droplet: (a) continuous movement of the droplet without film deposition; (b) movement with further detachment from the capillary; (c) continuous movement of the droplet with film deposition. Capillary moves from left to right

The ability of the droplet to stay in contact with the capillary in our case originates from the competition between two types of forces. They are the adhesion and capillary forces. The adhesion force which acts at the interface between the surface and the liquid operates in the direction, opposite to that of the movement, and the larger the contact area the higher the force is. The capillary force acts in the point where the droplet touches the capillary. The maximum value of the capillary force is limited by the nature of the solution and the capillary diameter. If the adhesion force is weaker than the maximum value of the capillary force then the droplet can move, whereas the domination of the adhesion force over the capillary force results in detachment of the droplet from the capillary.

Also, the moving droplet may deposit a thin film of liquid on the surface. The latter is observed when the capillary forces are quite strong and the surface tension is weak. In this case it is energetically more advantageous for the system to form a new surface than to detach from the capillary.

3.3.2. Nanostructures formation: morphology and orientation

Having carried out a considerable number of tests and experiments aimed at investigating the behavior of polymer molecules on surfaces I found that polyelectrolyte molecules can be deposited on hydrophobic surfaces by the moving contact line and a periodic pattern can be formed. Firstly, experiments were carried out for PSSA (polysterensulfonic acid, salt) water solutions with WL-5351 material used as surface modifier.

Different structures were formed depending on the droplet movement speed, solution and surface properties. Figure 3.6 shows 3 examples of such structures (single stripes, bundles and "roots"). Although the structures formed by the moving contact line look somewhat different, they have a common property. They are partially or completely oriented parallel to the movement direction (perpendicular to the contact line). This observation permits me to assume that the key elements that determine the orientation of the structures are the geometry and the contact line movement direction.

This hypothesis was confirmed by the observation that the structures display different orientation in different spots of the sample. Figure 3.7 shows the model of the moving drop and the adsorbed structures orientation. The different orientation is also shown on the AFM images and images captured by optical microscopy.
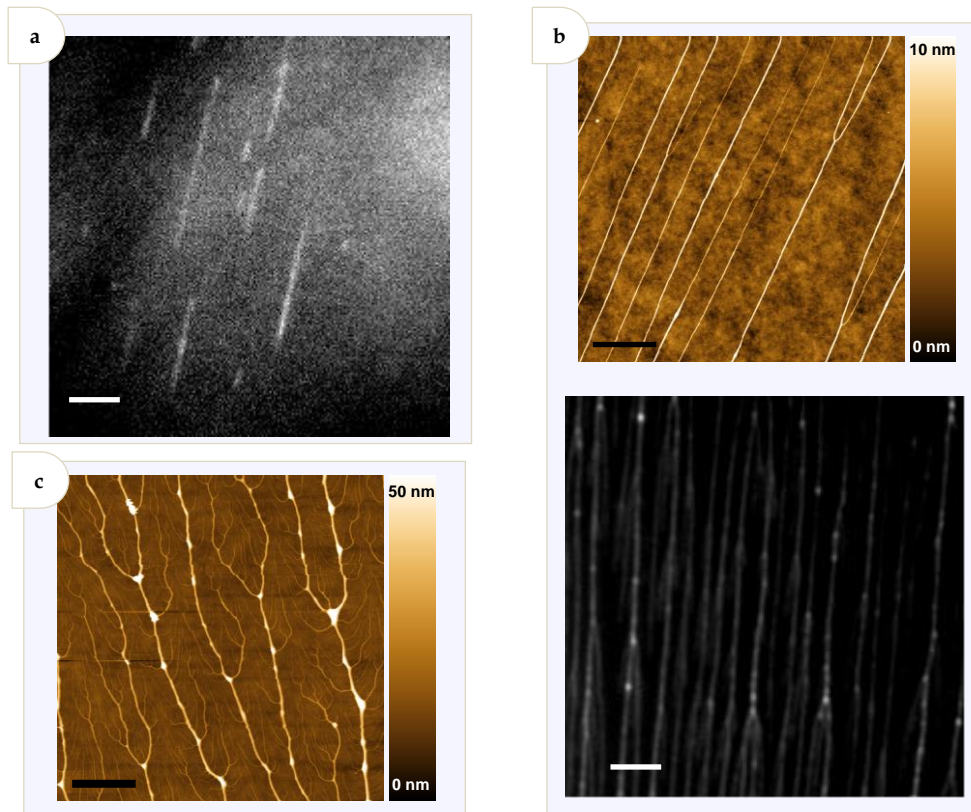

Figure 3.6: Nanostructure formed by the moving contact line (PSSA M_W = 6 900 000 g/mol, droplet volume 30 µL):
(a) Single stripes. Solution concentration 1 mg/mL, droplet movement speed ~10^{-3} m/s;
(b) Bundles. Solution concentration 10 mg/mL, droplet movement speed ~10^{-4} m/s;
(c) "Roots". Solution concentration 20 mg/mL, droplet movement speed ~10^{-3} m/s;
AFM images and images captured by fluorescent microscope shown here. On images black scale bar - 2µm, white one - 5µm.

Deegan also mentioned the influence of the moving contact line geometry on the orientation of structures.[Deegan2000-2] According to the results he obtained, both the advancing and receding contact lines play the role leading to the formation of two patterns which have a different orientation and cross. In my case only one type of pattern was observed with the orientation of the structures determined by the geometry and the receding contact line movement direction. I may assume that the reason for this was weak interaction of the polymer with the surface. In this case any structures formed

by the advancing contact line are destroyed (desorbed in the droplet bulk) or re-oriented by the receding contact line.

The observation that each nanostructure is oriented perpendicular to the local receding contact line allows us to control the orientation of nanostructures on the macroscopic level by changing the movement direction and the shape of the receding contact line. This is one of the most important advantages of using the moving contact line for fabrication of nanostructures.
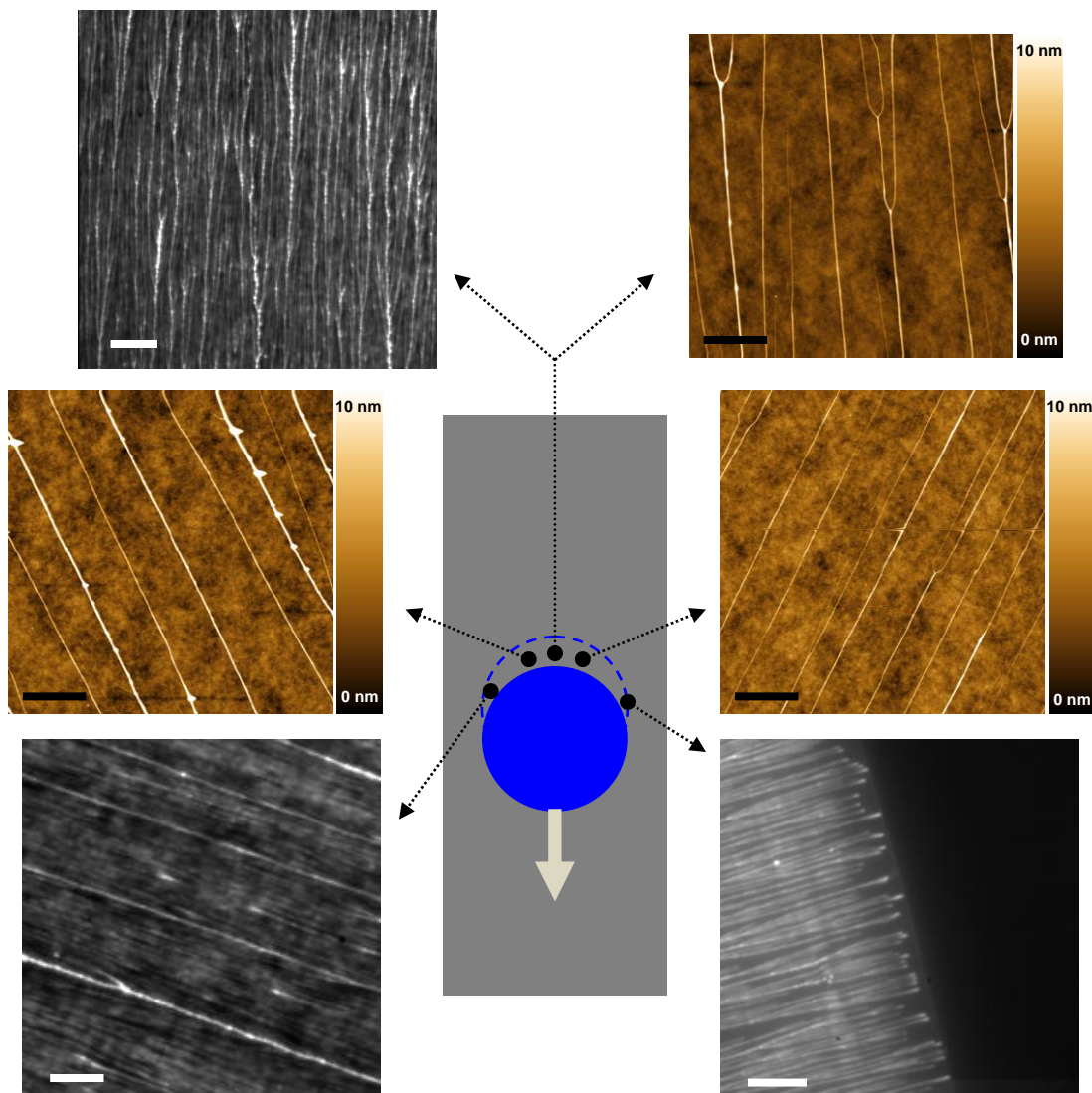
Figure 3.7: Model of a moving droplet, view from the top. In each point the nanostructures are oriented perpendicular to the local moving contact line. On the images black scale bar - 2µm, the white one - 20µm.

3.3.3. Moving the droplet with a pushing element

For further investigation I decided to improve the nanostructures formation process by changing the receding contact line shape from semi-circle to an almost straight one. It was done by using a flat and rather thick glass slide as a pushing element instead of the capillary pulling the drop. Figure 3.8 shows a sketch of such a set-up. As the glass advances, the larger part of the drop is being pushed in front of it and only a small portion is getting between the glass and the sample. The high hydrophobisity of the surface and the high surface tension of the water solution do not allow the droplet to slide to the back of the glass. Due to the high hydrophobisity the water droplet repeats the shape of the glass. It is also possible to fix the glass on a moving trolley, which would allow to control the speed with more precision. Such a set-up has another advantage over the capillary-driven movement, that is the possibility of wider movement speed variation, especially for solutions with high viscosities.
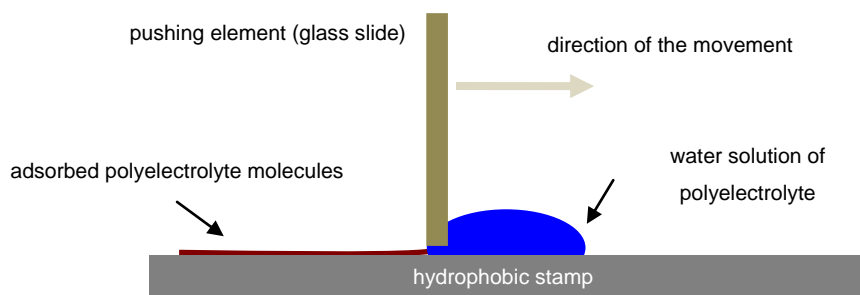
Figure 3.8: Sketch of droplet followed by pushing element.

3.3.4. Molecular bundles

Among the most interesting structures are bundles. These are mechanically entangled polymer molecules which dry to form single separate strings. The orientation of such bundles is perpendicular to the moving contact line and they also display an extremely high aspect ratio. Typical PSSA bundles have the diameter of several nanometers (the biggest one was 50 nm in diameter) and the length of many microns. The possible length of the bundles was investigated by continuous AFM imaging and it was discovered that uninterrupted length of the bundles may reach more than 0.25 cm

(see figure 3.9). Probably some bundles can be infinite and in such cases their length will be limited by the sample dimensions only.
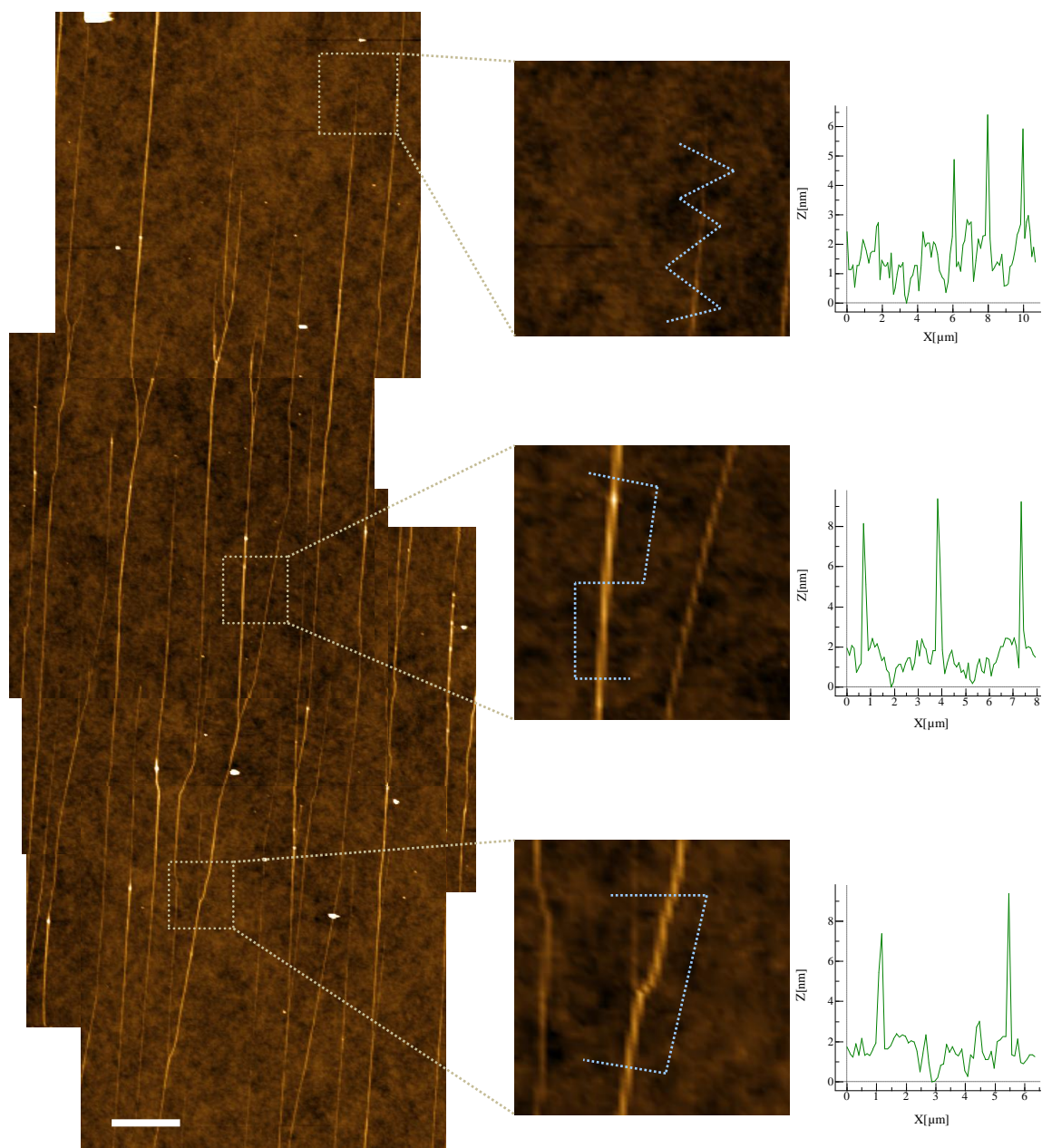

Figure 3.9: Continuous AFM image represents the uninterrupted nature of the bundles. The close-up images on right side represent the starting point of the bundle, bundle body and knot, respectively. Scale bar - 5 μm.

Each bundle has a starting point, i.e. the place where the first polymer molecule was "trapped" on the surface. Then the diameter increases to a certain value and upon reaching it remains constant. Let us call this region body – a string with a constant

diameter. In some cases bundles join together, and such points are called knots. Smaller bundles will be referred to as branches.

It was observed that when a branch joins a bundle, the bundle locally changes its orientation. The scale of the change depends on the thickness of the branches. The thicker branches cause more considerable changes. Sometimes two or more branches join bundle in one knot. Figure 3.10 shows 3 examples of bundle distortions at knots.
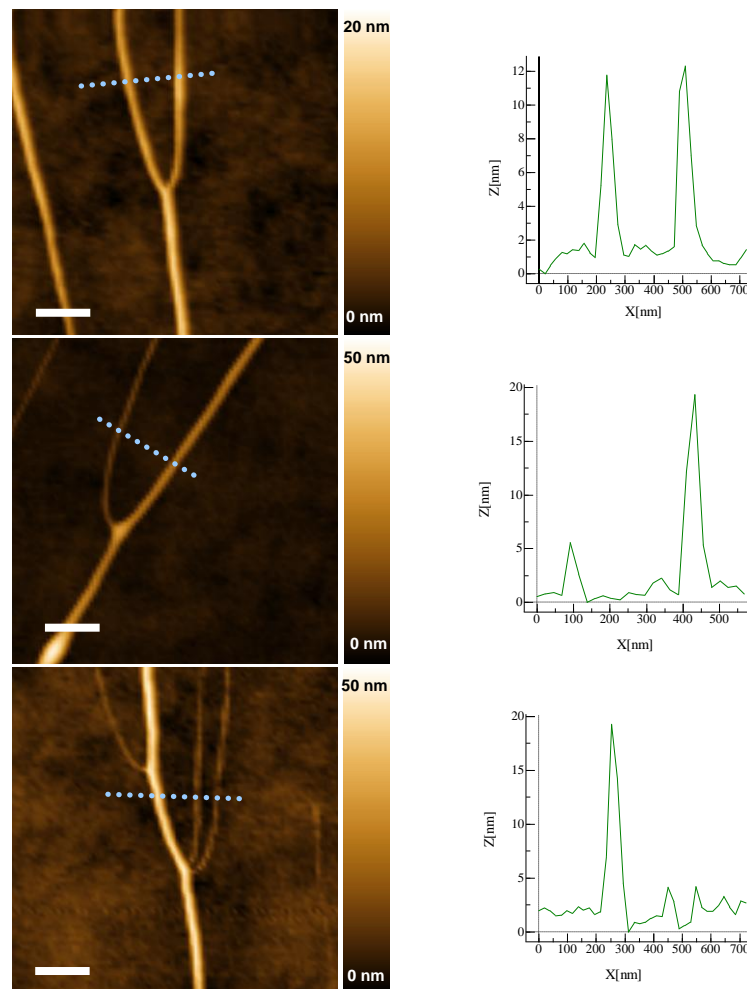
Figure 3.10: Examples of knots. The first image presents a knot formed by PSSA molecules from 10 mg/mL solution, the other two images shows single and double branching of the bundles obtained from 20 mg/mL PSSA solution. PSSA M_W=6 900 000 g/mol, droplet movement speed $5*10^{-3}$ m/s in all cases. Scale bar on AFM images - 300 nm.

Figure 3.11 presents a sequence of captured images demonstrating pattern formation by the moving contact line. Images were taken with an optical microscope in the fluorescent regime. Rhodamine 6G was used as the fluorescent mark for PSSA molecules. The upper left part represents liquid, the contact line moves from bottom-

right to top-left. In conducting this experiment a small drop of PSSA solution was placed between two pieces of glass with WL-5351 coating. The moving contact line was realized by the surface tension forces during water evaporation. This process is quite different from the moving droplet, however for the purpose of simplification it can be used for preliminary *in situ* visualization of patters formation by the moving contact line.
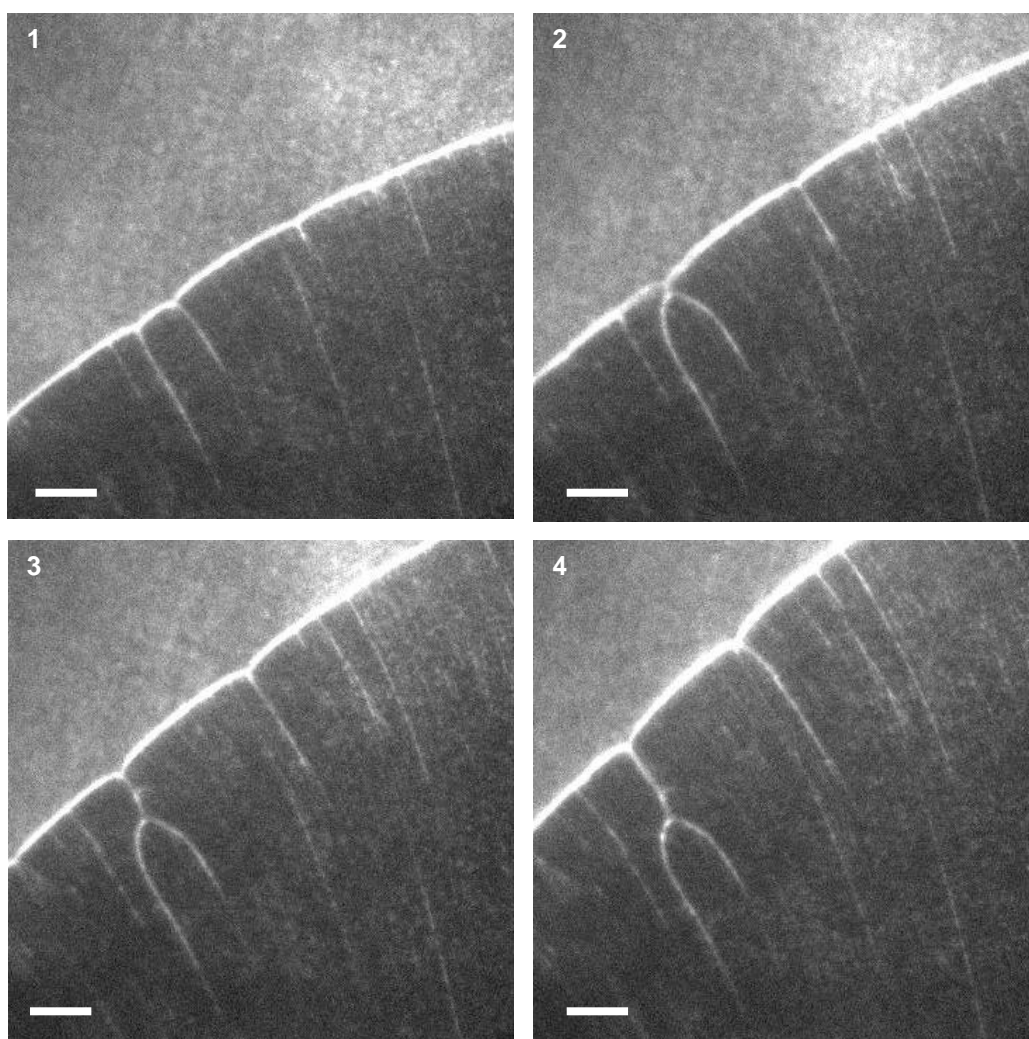

Figure 3.11: Nanostructures formation observed with fluorescent optical microscopy. Images were captured with delay 500 μs. Scale bar - 10 μm.

3.3.5. Influence of the droplet movement speed and solution concentration on pattern formation

The number of bundles per micron, their diameter distribution, and the number of knots depend on the speed of the droplet movement and on solution concentration. A higher speed of movement conditions a lower number of bundles as well as reduction of branching, a smaller diameter of an average bundle and a narrower diameter distribution. The same results were observed in a situation of decreasing solution concentration (see figure 3.12). As one can see, the increase of concentration from 10 mg/mL to 20 mg/mL led to a tenfold increase of branching (see figure 3.13). These concentration ranges do not allow decrease of the branching by increasing the movement speed because the liquid is too viscous to retain contact with the moving capillary. I assume that such limitation of the highest speed of the droplet movement exists for any concentration, even for pure water.
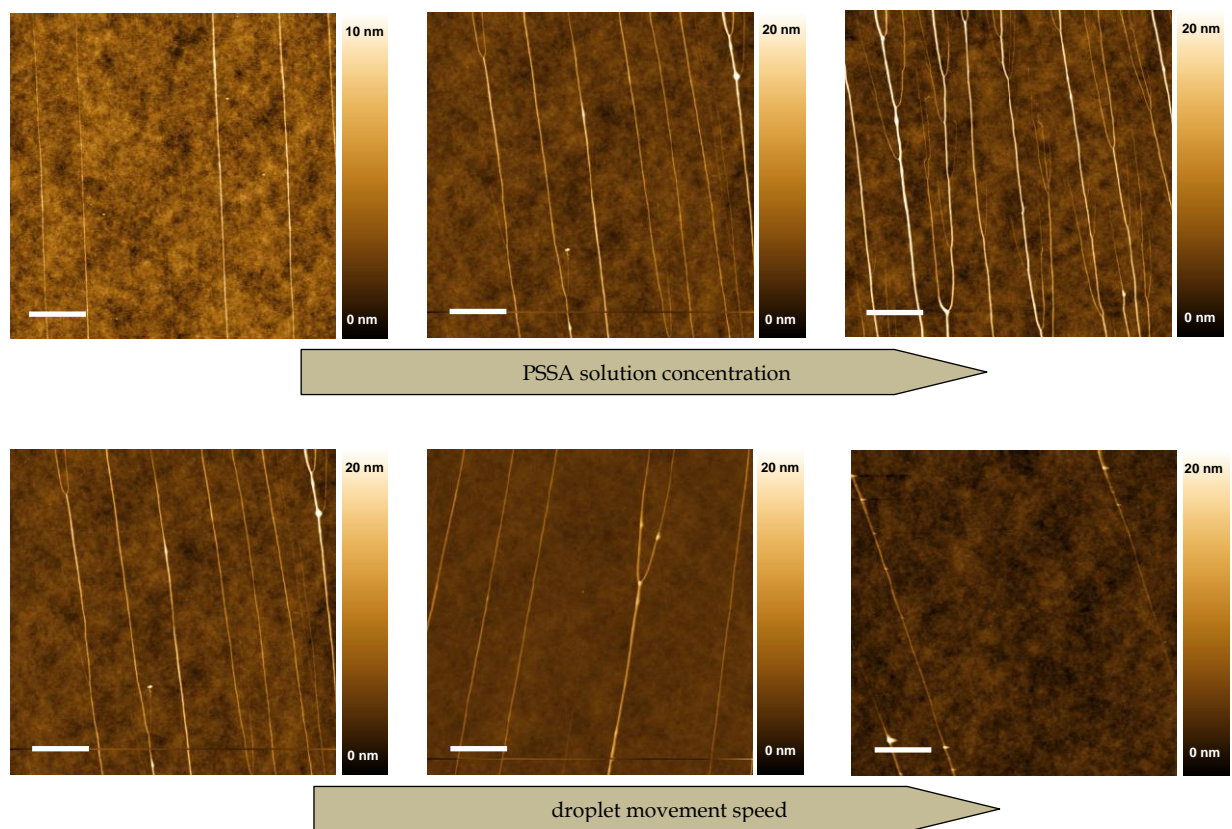
Figure 3.12: Dependence of the bundles morphology on the PSSA solution concentrations and on the droplet movement speed. Scale bar - 2 μm.

It should also be mentioned that a moving droplet with polyelectrolyte concentration lower than 1 mg/mL doesn't yield bundles. Only single molecules deposited as stripes could be found, but the process of stripes formation was often unstable and normally no structures were found at all.

Effects of different concentration with constant droplet movement speed ~10 cm/min
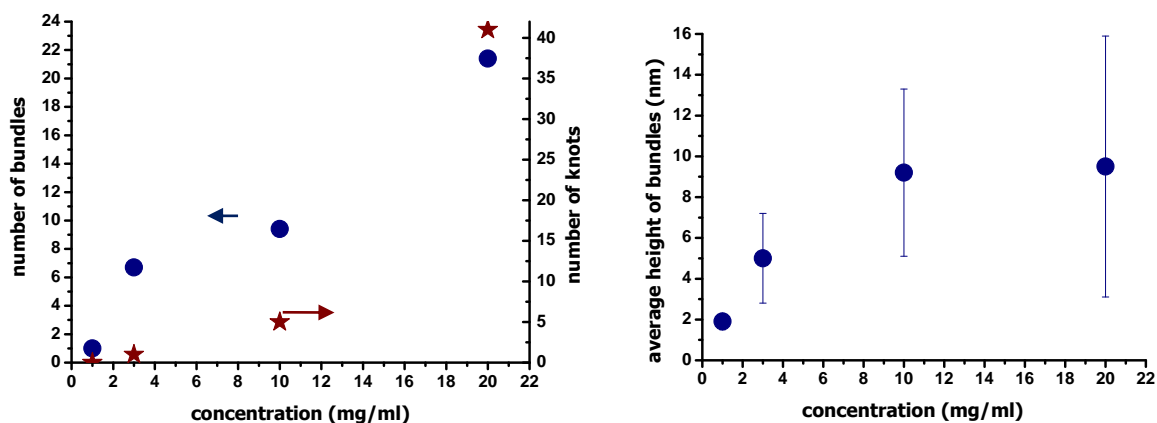
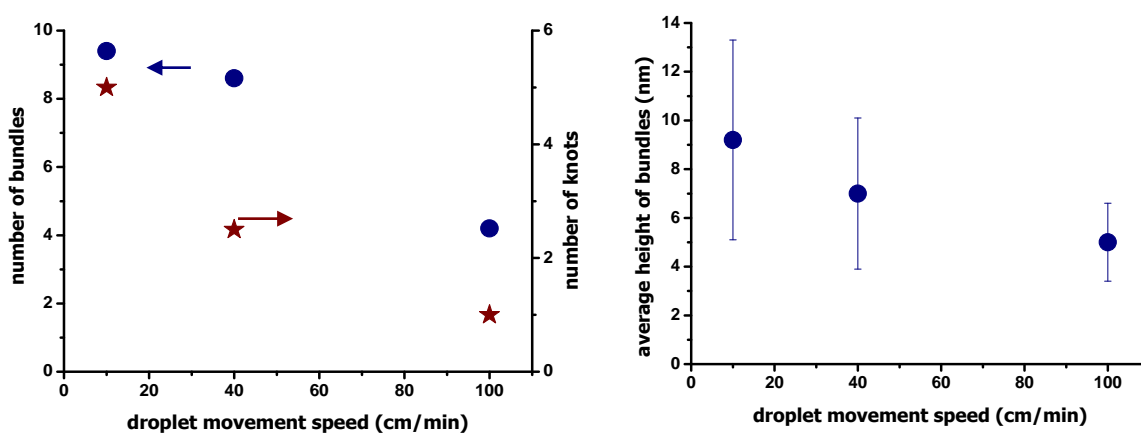Effects of different droplet movement speed for concentration 10 mg/mL

Figure 3.13: Influence of the concentration and droplet movement speed on the number of bundles and their morphology. Data was obtained after statistical treatment of AFM images. Values [number of bundles] and [number of knots] were calculated for 10 μm x10 μm area. Vertical brackets represent the bundle heights distribution.

3.3.6. Influence of the polyelectrolyte MW on pattern formation

Another source of significant influence on pattern formation is the molecular mass of polyelectrolyte. For PSSA M_W = 30 000 g/mol no bundles formation was obtained

even at the highest possible concentration of 140 mg/mL. The samples produced at this concentration and with low movement speed demonstrate only roughness changes on AFM images. This probably corresponds to the presence of network-like structures with nanometer scale heights. The samples produced at the concentration of lower than 100 mg/mL demonstrate no structures when investigated by AFM and by fluorescent microscopy.
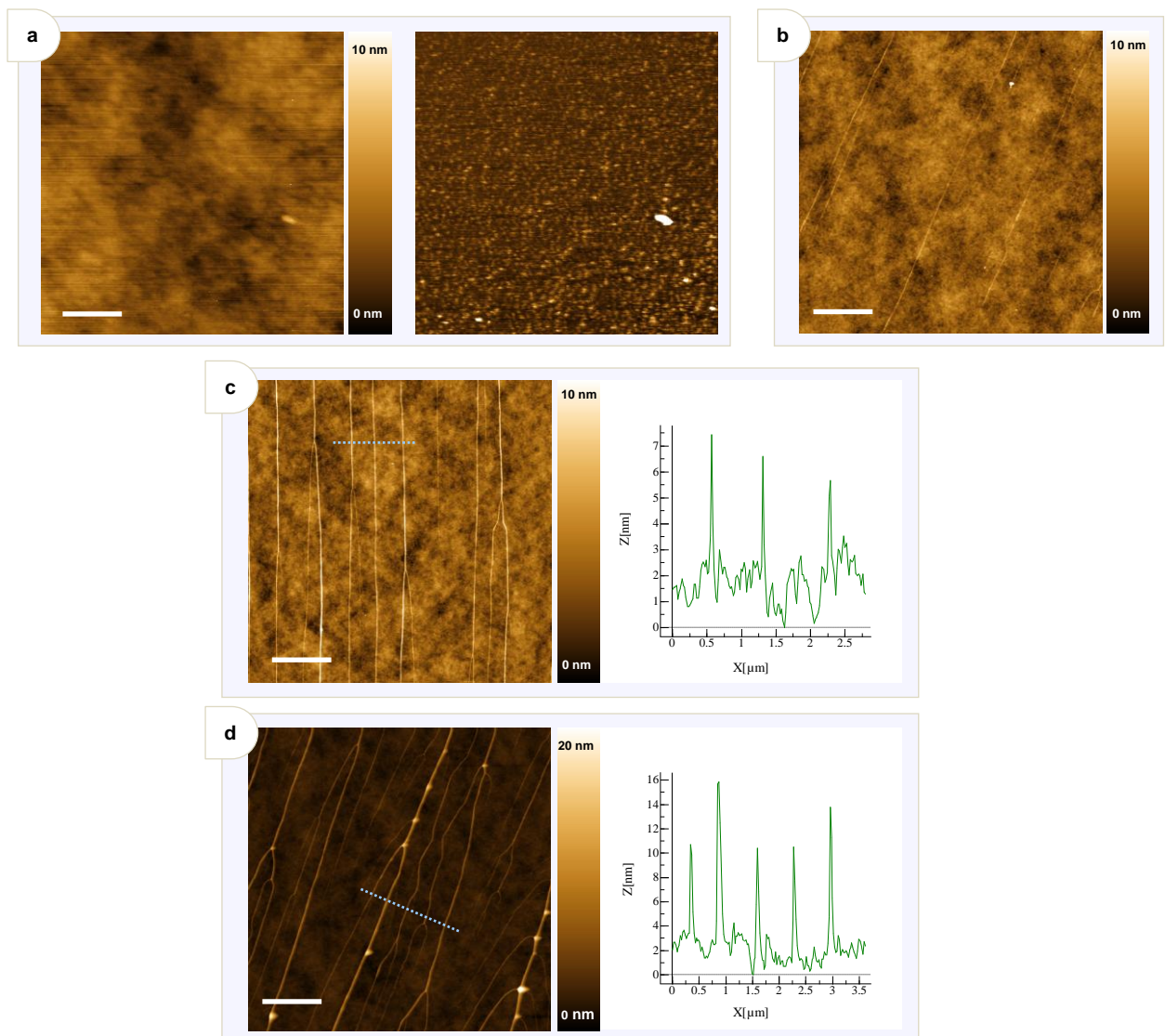

Figure 3.14: Influence of the PSSA molecular mass on the morphology of nanostructures.
(a) PSSA M_W = 30 000 g/mol, 140 mg/mL concentration. Height and phase AFM images. Scale bar - 400 nm;
(b) PSSA M_W = 200 000 g/mol, 5 mg/mL concentration. Nanostructures have heights comparable with surface roughness. Scale bar – 1 μm;
(c) PSSA M_W = 500 000 g/mol, 5 mg/mL concentration. Scale bar - 2 μm;
(d) PSSA M_W = 6 900 000 g/mol, 5 mg/mL concentration. Scale bar - 2 μm.

Moving a droplet with concentration 10 mg/mL of PSA M_W = 6 900 000 g/mol at the speed of ~5 cm/min lead to the formation of highly branched bundles with heights of ~10 nm. However for M_W = 500 000 g/mol a non-branched periodic pattern of bundles with the height of ~5 nm was obtained. And for M_W = 200 000 g/mol only a few bundles per a 10 µm x 10 µm scan were found with heights comparable with the surface roughness (see figure 3.14). The polyelectrolyte molecular mass has influence on the viscosity of solution and on the number of entanglement per one polymer molecule.

The application of the flooding method on AFM images of heights provides a possibility to calculate the amount of the deposited material. Such operation was carried out for two molecular weights (M_W = 6 900 000 g/mol and M_W = 500 000 g/mol) and for a set of concentrations. The results are presented in figure 3.15. It is evident from the image that for a certain molecular concentration and movement speed there exists a threshold in the deposited mass – concentration dependence. Both M_W = 500 000 g/mol and M_W = 6 900 000 g/mol possess a threshold near the concentration equaling ~3 mg/mL and the movement speed of 5 cm/min. For concentrations lower than that no deposition was detected. Also a lower molecular mass leads to a lower amount of deposition, which was partly shown in figure 3.14 as well. And the increase of the movement speed shifts the threshold towards lower concentrations.
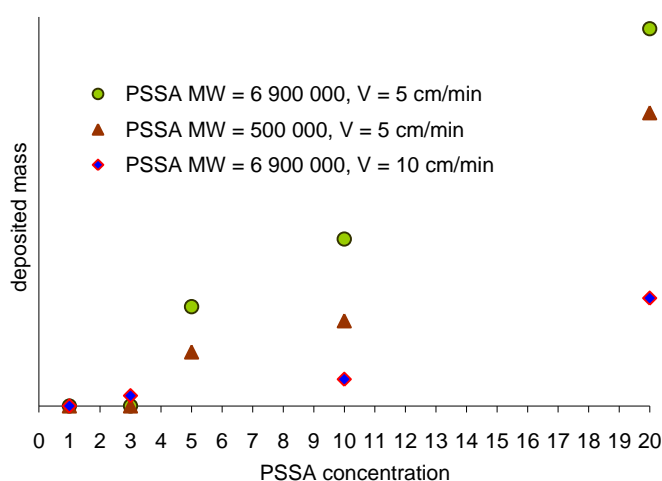

Figure 3.15: Deposited polyelectrolyte mass – polyelectrolyte concentration dependence calculated from AFM images.

3.3.7. Influence of bivalent salt additives on pattern formation

The influence of the solution viscosity and the number of entanglement per one polymer molecule on the morphology of bundles can also be traced in experiments when bivalent salt is added to the solution. Figure 3.16 presents the results of such experiments.
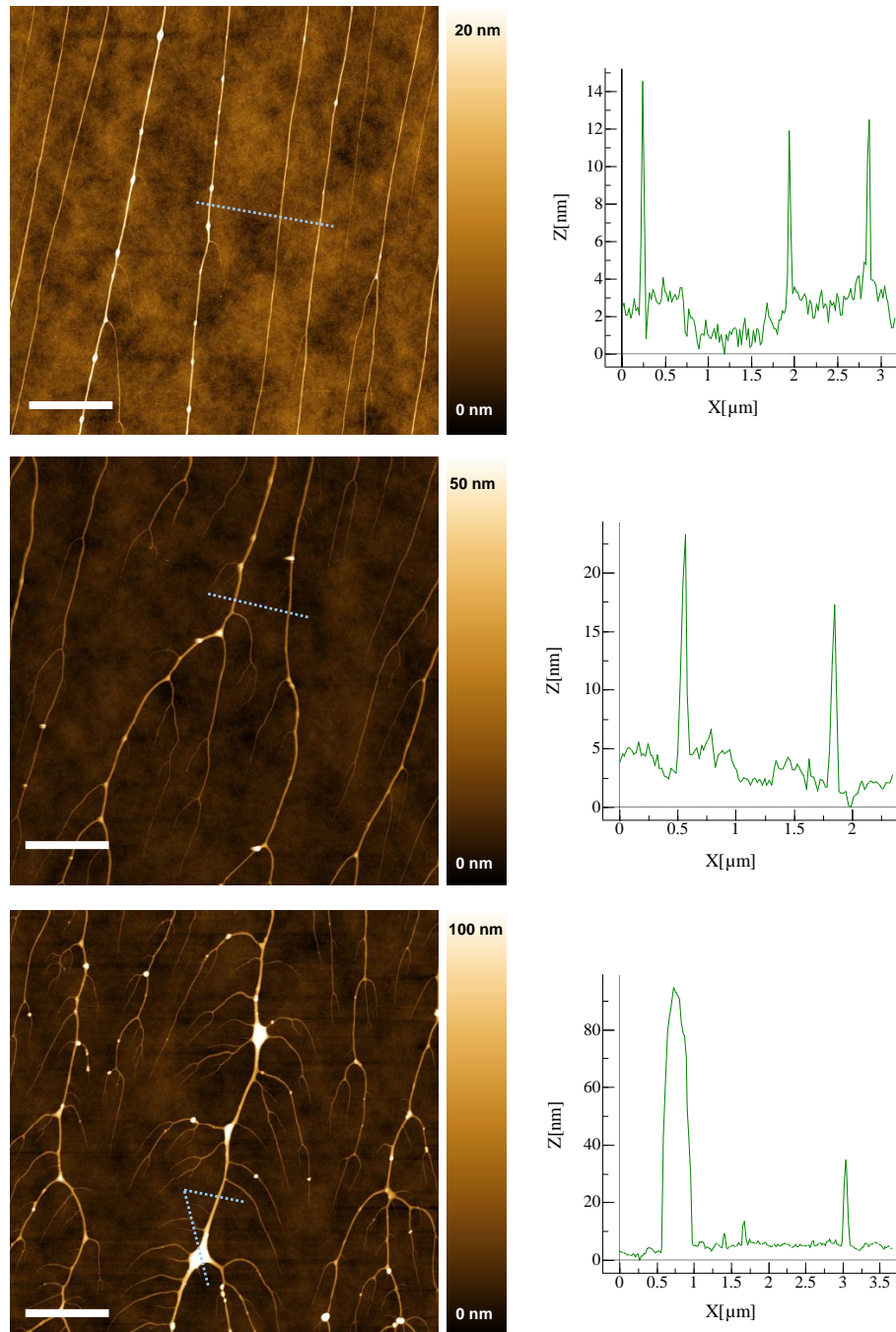

Figure 3.16: AFM images of the nanostructures obtained from 5 mg/mL PSSA solution with different additions of $CaCl_2$: 0.01 mg/mL, 0.2 mg/mL and 2 mg/mL. Scale bar - 2 μm.

For samples with $CaCl_2$ concentration of 0.01 mg/mL no significant distortions were found, only a few point defects on the bodies of the bundles were detected; however the concentration of 0.01 mg/mL equals to, approximately, 100 new ionic bonds between the interchain and extrachain monomer units per polymer molecule. And only a huge amount of salt added to the solution leads to the increase of branching and to significant bundle distortions, as well as to the increase of the bundle heights. On the ground of the data I propose the idea that viscosity is one of the most significant parameter which determines the morphology of bundles and their number.

3.3.8. Nanostructures formed on different surfaces

The results of the experiments carried out for PSSA solution droplets on surfaces with different hydrophobisity allow for a conclusion that nanostructures may be formed on them as well, see figure 3.17. Different concentrations, M_W's and movement speeds may be used to adjust the formation of nanostructures induced by the moving contact line. A lower level of hydrophobisity brings about a stronger liquid-surface interaction and a stronger adhesion force. This effect limits the concentrations and speeds which can be used for surfaces with low hydrophobisity.
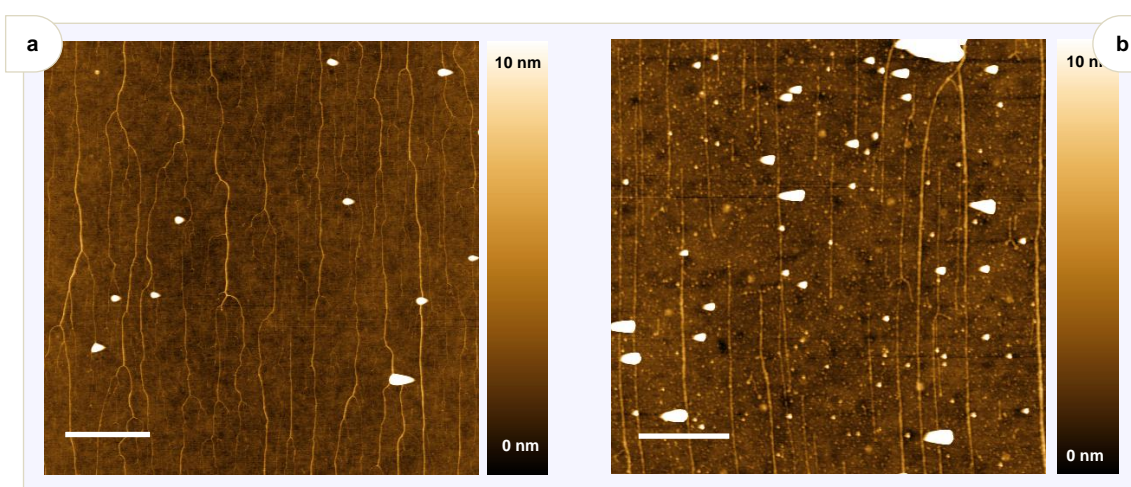

Figure 3.17: Examples of bundles on different surfaces: (a) silicon wafer with PGMA layer, covered by Poly(2,2,3,4,4-hexafluorobutylmethacrylate-co-butylmethacrylate) 50/50; (b) silicon wafer with PGMA layer, covered by PtBuA. Scale bars - 2 μm.

The fact that polyelectrolyte molecules have different adhesion force to the places with different hydrophobicity allows using patterned surfaces for controlled deposition of nanostructures. As proof of concept I perform a polyelectrolyte deposition via the "droplet pulling" method on a patterned PS surface. The preparation of the patterned surface is described in Ref. [Khanduyeva2009]. As shown in figure 3.18 the PSSA bundle repeat the pattern order.
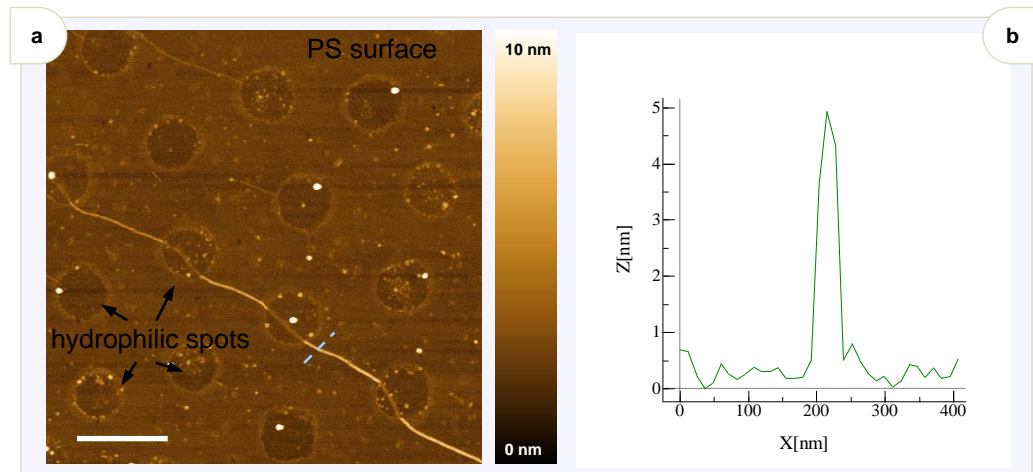

Figure 3.18: (a) AFM image and (b) cross section of the PSSA bundle deposited on a patterned surface. Scale bars - 1 μm.

Utilization of fluoro-silane [*(heptadecafluoro-1,1,2,2-tetrahydrodecyl)triethoxysilane*] allowed me to produce a sample with a high hydrophobic surface. Bundles were fabricated on that surface in the same manner as on the WL-5351 surface, but with one important distinction. The bundles were partly collapsed, see figure 3.19. The reason for this was the low level of interaction between the bundles and the surface. Such relaxations are no doubt entropy driven and are typical for macromolecules systems. Formation of the bundles structures was followed by collapsing processes. In cases when the bundles collapsed during the contact line movement, such collapsed bundles, or hills, would cause significant distortion of the contact line, which would then increase the deposition of the polymer. However, hills and bundles coexist next to each other. I assume that intensive collapsing processes took place right after the bundles formation, when some water molecules still existed in the intermolecular space. The weak mobility of the macromolecules on the surface was enough to collapse the bundles to hill-like structures. There is a chance that the relaxation processes remain

effective even at lab humidity and temperature, but clear and sharp AFM images provided me with the ground for a conclusion that these processes are weak and slow.
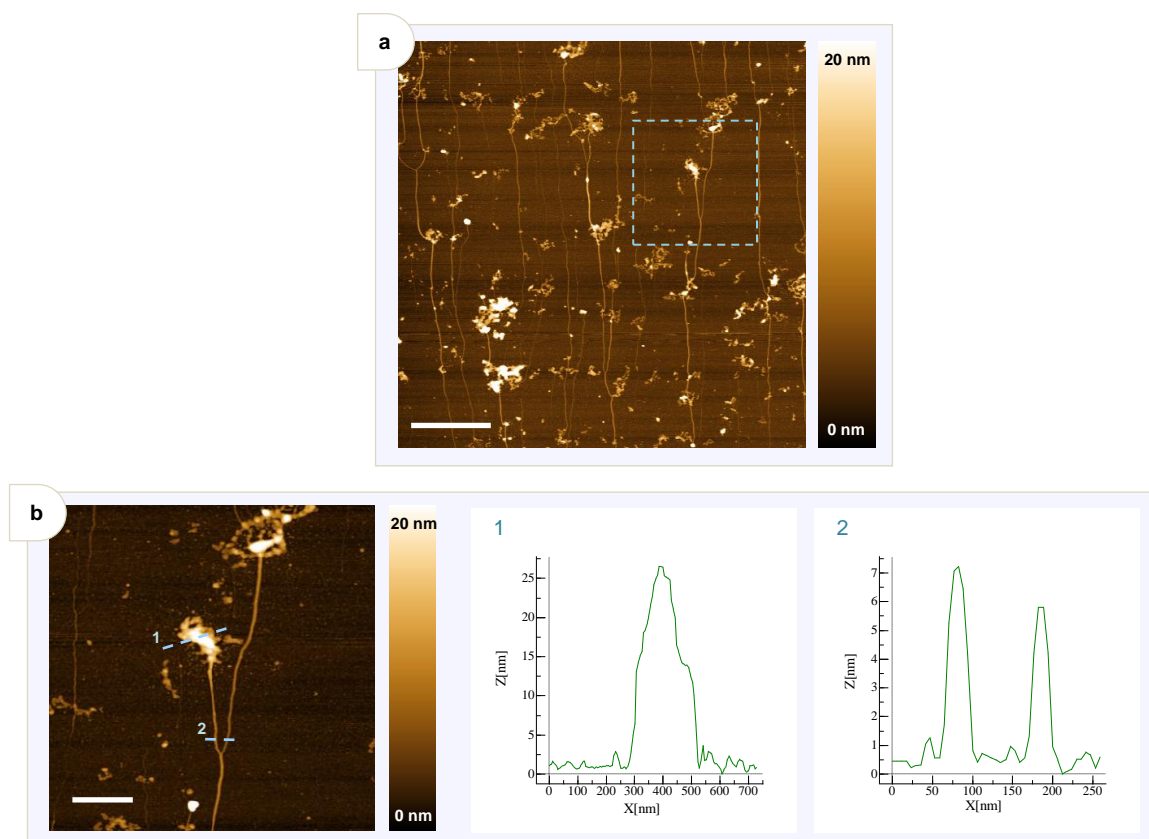

Figure 3.19: AFM images and cross sections of the partly collapsed bundles on a hydrophobic surface. PSSA M_W = 6 900 000 g/mol, 10 mg/mL concentration. (a) Scale bar - 2 µm; (b) Scale bar – 600 nm.

Such behavior of macromolecules indicates that nanostructures formation during the movement of the contact line is not a "pure" molecular combing process. In the molecular combing process the key factor is high affinity of the polymer molecules to the surface. In my case the PSSA molecules don't have the affinity to hydrophobic surface.

3.3.9. Moving the sample surface above the standing droplet

Bundle-like nanostructures can be fabricated even on surfaces with a water contact angle of ~70°. For this purpose a special technique has been developed. One of the

forces which work against the droplet movement is the adhesion force. This force is proportional to the area of the interface between the liquid and solid.

In the case when a droplet followed by capillary the droplet-solid interface has some value according to the droplet volume and the wetting contact angles. To decrease the droplet-stamp interface area one has to decrease the volume of the droplet. However, precise control over the movement of droplets smaller than 30 µL without special equipment is problematic. Also the maximum value of the capillary force is limited by the nature of the solution and the capillary diameter.
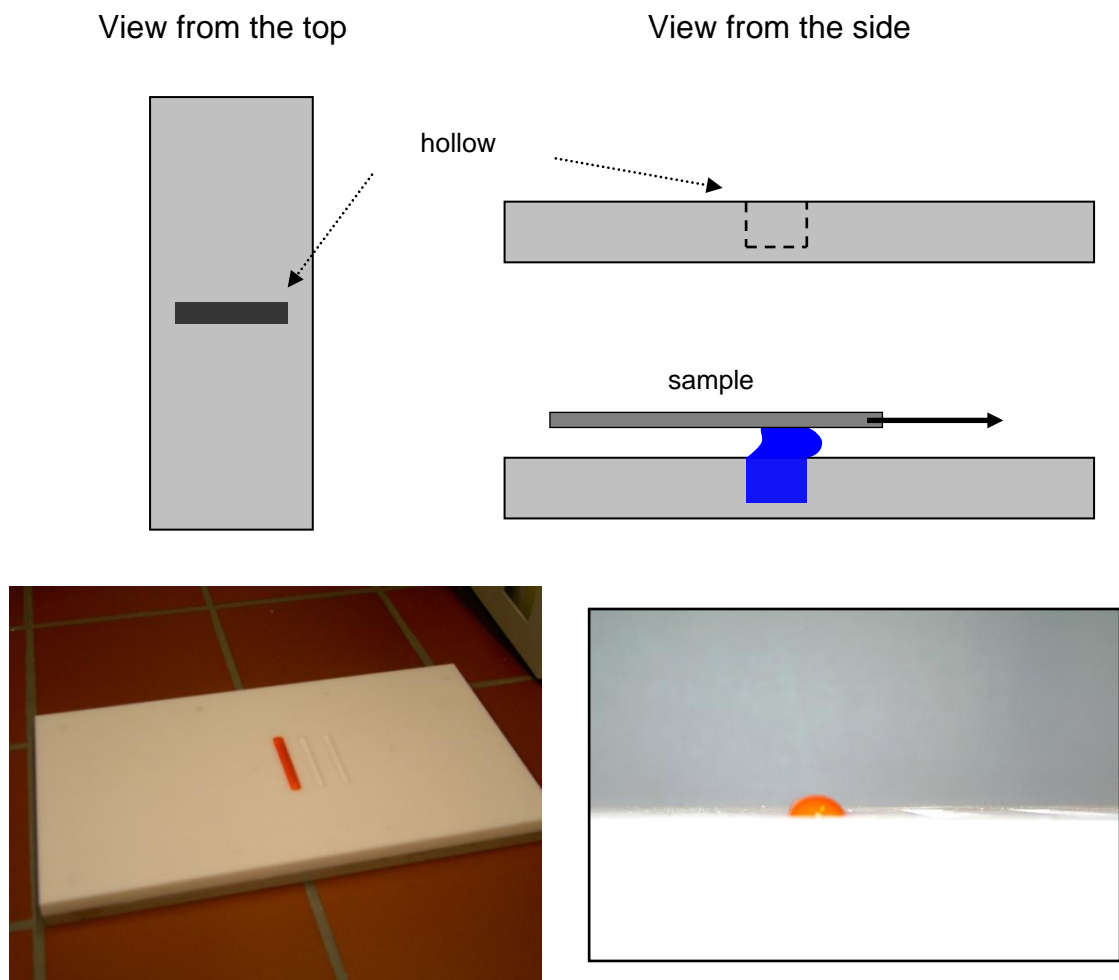

Figure 3.20: Sketch and photos of the set up where the surface of the sample moves above the standing droplet.

By using a set up where the surface of the sample moves above the standing droplet one avoid the problem of the limited maximum value of the capillary force. In

such a set up the liquid is placed in a hole in a Teflon plate that prevents the liquid movement on the Teflon surface. The water solution doesn't spread on the Teflon surface and forms a hemispherical profile. To perform the experiment the sample was gently brought in contact with the top part of the liquid and then moved. By adjusting the distance between the sample and the Teflon plate it is possible to control the interface area between the liquid and the sample and therefore the adhesion force. A sketch and a photo of the set up functioning on this principle are presented in figure 3.20.

Interestingly, there is a difference in the bundles size of the resulting structures obtained by the "droplet pulling" and "surface pulling" methods. For example, for PSSA M_W = 6 900 000 g/mol, the polyelectrolyte concentration of 10 mg/mL and the movement speed of 10 cm/min the bundles obtained by moving the sample above a standing droplet display a much lower height than the bundles obtained by the "droplet pulling" method (see figure 3.21).
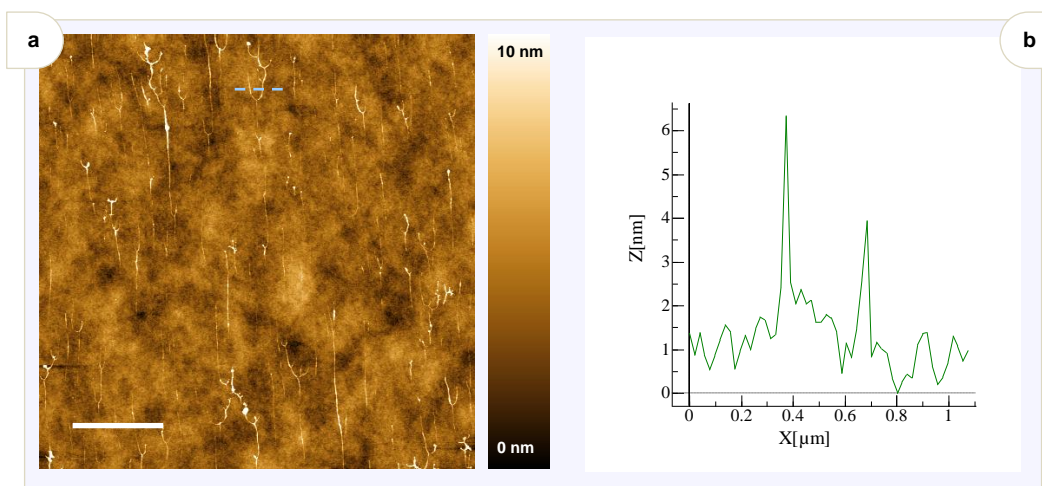

Figure 3.21: (a) AFM image and (b) cross section of the PSSA nanostructures obtained by moving the surface above the standing droplet. Scale bar - 2µm.

3.4. Model proposal and discussion

It has been shown above that the formation of nanostructures on a hydrophobic surface by the moving contact line cannot be explained by molecular combing. Clearly we are dealing with a different type of processes. The understanding of these processes

and of the key factors which determine the formation of nanostructures induced by the moving contact line is one of the goals of this thesis.

It has been demonstrated that the nanostructures morphology is the result of influence of many factors. There is polymer concentration, M_W's, speed of the droplet movement, surface properties, etc. The formation of nanostructures by the moving contact line is a complex process. For the purpose of simplification of the further discourse I would like to divide the moving liquid into 3 regions as shown in figure 3.22. Also I would like to underline that in my case the most important processes take place in the receding contact line and therefore I will focus on this part only.
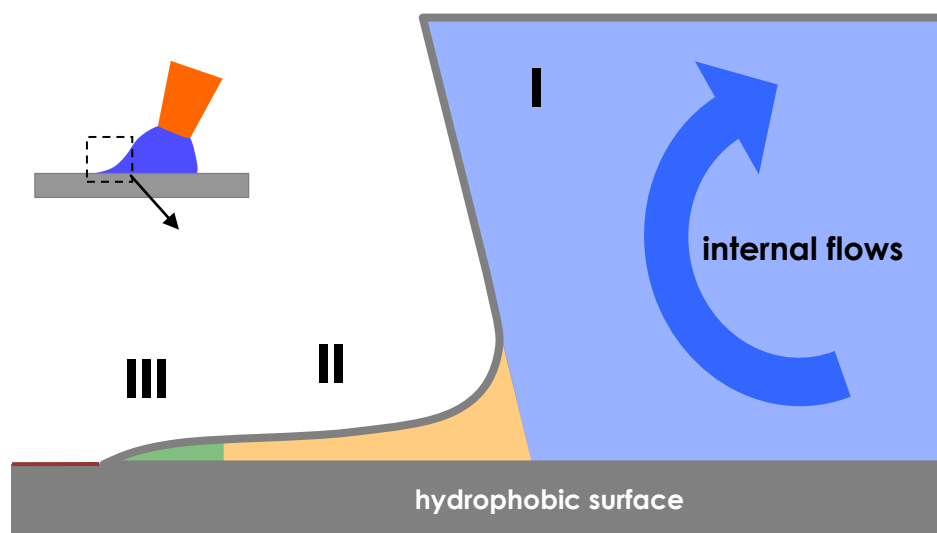

Figure 3.22: Sketch of the receding contact line. Three regions of interest.

The first region corresponds to the bulk of the liquid, where the polymer and water molecules should be described as a liquid phase with such macroparameters as concentration, temperature, pressure, viscosity. In this region the polymer molecules may or may not form an entangled network, which depends on the concentration, nature of the polymer and salt additives.

During the droplet movement in this phase internal flows appear, their cause being the friction forces. Undoubtedly, there are convection flows there, flows caused by changes in the concentration at the liquid-gas interface. Kaneda *et al.* pointed out that for a standing drying drop of acetophenone (which has the viscosity similar to that of the water) solution of PS the internal flows have velocities less than 10^{-5} m/s.[Kaneda2008]

However, circular flows caused by the rolling of the droplet are much more intensive in the case of moving water solutions at normal pressure, ambient temperature and movement speeds of ~10^{-3} m/s. The intensity of these flows increases with the increase of the droplet movement speed.

I will use the term lag region to denote the second region. This region should be defined as part of the receding contact line from which the solute cannot diffuse to the bulk of the liquid. In this region the dynamic contact angle significantly differs from the static contact angle.

The lag region originates from the following process. During the movement the adhesion forces act on the liquid and part of the liquid near the gas-liquid-solid interface forms a region with a contact angle lower than the static one, according to Cox equation 1.E13. The geometry limitation leads to the decrease of the polymer molecules mobility near the receding meniscus. The said drop in mobility causes an increase of the disturbance of the receding contact line and a thick film is formed. Further on this film becomes thinner in the direction away from the liquid phase.

The lag region may or may not be formed depending on the viscosity of the polyelectrolyte solution and the intensity of the adhesion forces. For example, a higher concentration of the polymer solution leads to a higher viscosity which results in the formation of the lag region.

An assumption which is important for the purpose of our study is that polymer molecules cannot diffuse into the first region or this process can be ignored on the basis of its low intensity. The implication of this assumption is that all of the polymer mass in region II will be deposited on the surface.

On the other hand the formation of the lag region causes an increase of the total adhesion force which acts on the liquid and may result in detachment of the droplet from the capillary, which has already been mentioned above.

The third region is the area where the polymer molecules deposit on the surface. The process taking place here determines the way the mass "trapped" in region II is deposited and also the way nanostructures are built.

Several possibilities can be identified here. The thin liquid film can be affected by different instabilities which may lead to film rupture. In case the instabilities growth

rate is a bit lower than the velocity of the drying processes, a thin polymer film (provided there is enough mass) or network-like structures will be formed. On the opposite, when the instabilities growth rate is high enough, separate nanostructures may be obtained.

In the case when separate bundles were formed I propose the existence of two effects which make the bundles formation process preferable and stable.

The first effect is the rupture of the receding contact line at the early stages of the movement of the liquid. The reason for this lie in the instability appearance in the thin film of the liquid (region III). Region III, without the part that is close enough to the contact line, can be approximated as a thin film with a certain average high h_0, see figure 1.6. The long-wave theory may be applied to determine and understand the processes underlying the film rupture into rivulets.

Taking into account the disjoining pressure only as an attraction potential $\varphi = \varphi_r + A'h^{-3}/6\pi$ it follows from Eq. 1.E90 that there is instability for A'>0, driven by the long-range molecular forces and stabilization is due to the surface tension and gravity. The cutoff wave number k'_c and cutoff wavelength λ_c are then given by

$$k_c{'} = \sqrt{\frac{A'}{2\pi\sigma h_0^2} - \frac{\rho g h_0^2}{\sigma}}, \quad \lambda_c = \sqrt{\frac{8\pi^3\sigma h_0^4}{A'-2\pi\rho g h_0^4}} \qquad (3.E1)$$

which reflects the fact that an initially corrugated interface has its thin regions thinned further by the van der Waals forces while the surface tension cuts off the small scales. Instability is possible only if $0<k'<k'_c$. It is useful to determine the wavelength of the perturbation which has the maximum growth rate. For this $\frac{ds}{d\lambda} = 0$ from Eq. 1.E90 was taken and λ_{max} was found as

$$\lambda_{max} = \sqrt{\frac{16\pi^2\sigma h_0^4}{A'-2\pi\rho g h_0^4}} \qquad (3.E2)$$

or

$$\lambda_{max} = \sqrt{2\pi}\,\lambda_c \qquad (3.E3)$$

Figure 3.23 shows the dependence of the most probable perturbation wavelength λ_{max} on h_0.
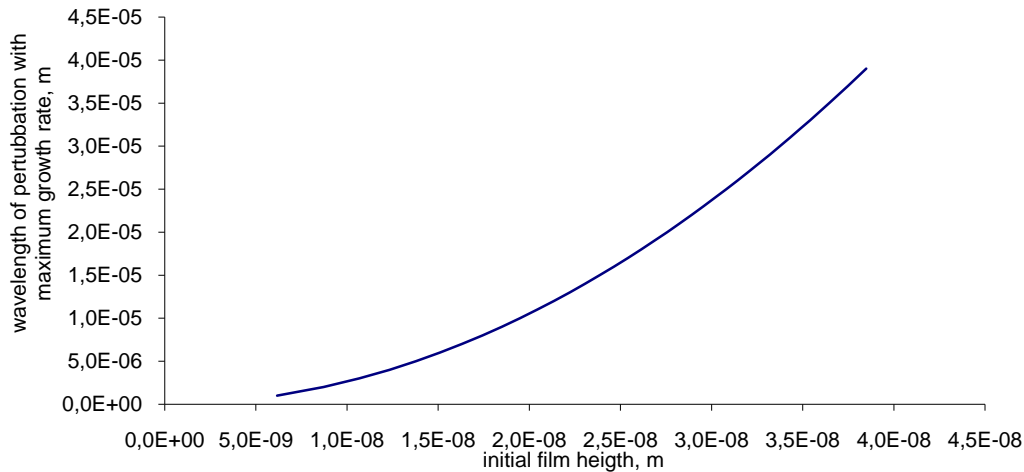

Figure 3.23: Dependence of the most probable perturbation wavelength on the initial film height, according to equation 3.E2, where A'=5*10^{-20} J; σ=7*10^{-2} N/m; ρ=1000 kg/m³.

According to the long-wave theory a thin liquid film has a tendency to rupture, and the wavelength of the instability decreases with the decrease of the initial h_0 as λ_{max} ~ h_0^2 and, as follows from equations 1.E90 and 3.E2, the growth rate of the most probable perturbations increases as S ~ h_0^{-5}, see figure 3.24.
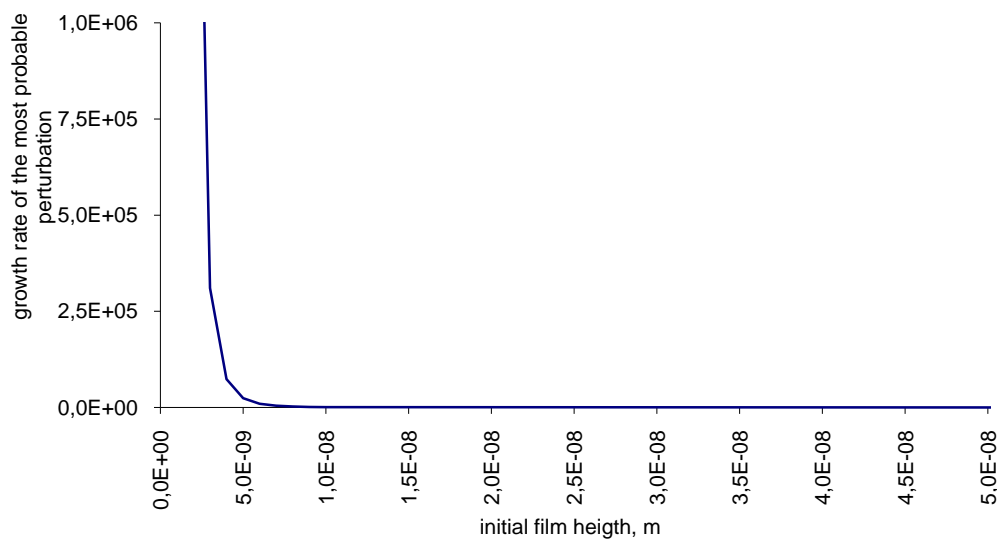

Figure 3.24: Dependence of the most probable perturbation growth rate on the initial film height. (A'=5*10^{-20} J; σ=7*10^{-2} N/m; ρ=1000 kg/m³)

As follows from figures 3.23 and 3.24 in the case of thin water films the instabilities start to grow when the film thickness approaches the nanometer scale. And the characteristic wavelengths of such instabilities are equal to several micrometers.

These periodic ruptures of the contact line lead to alternations of the regions with the viscous polyelectrolyte solution and regions with clean surface. And the regions with the viscous polyelectrolyte solution will result in starting of rivulets.

Simultaneously with the contact line rupture which causes the appearance of rivulets the second process starts. The polymer molecules in region II start to distribute into rivulets (see figure 3.25).

Each rivulet presents a new surface, and due to the total surface minimization requirement the system displays a tendency for reduction of the number of rivulets. On the other hand, the deposition of the "trapped" polymer molecules requirement calls for an increase of the number of rivulets. Acting in the opposite directions these two factors keep the number of rivulets constant.
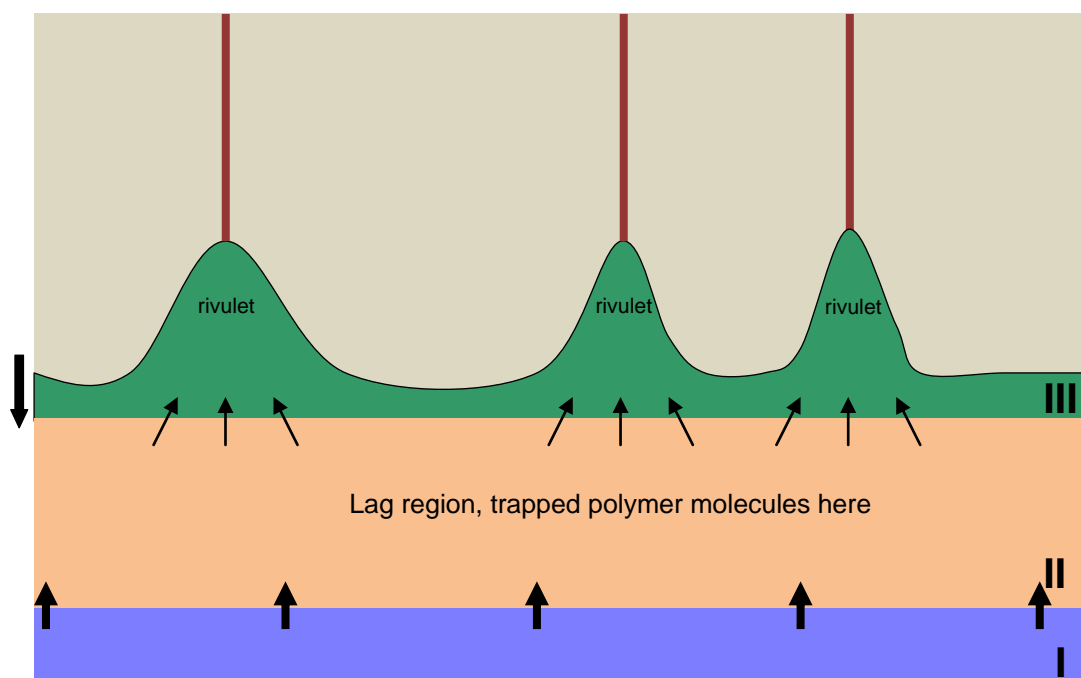

Figure 3.25: Distribution of the mass into rivulets. The black arrow on the left indicates the direction of the contact line movement.

In cases when a high concentration solution was used, a lot of molecular entanglement was registered. The polymer molecules which had already been involved

in the rivulets formation pull other molecules from region II, with which they were entangled. This process keeps each rivulet stable.

If the number of the entanglements is too high and the neighboring rivulets have molecules entangled in region II, such rivulets join into one. This process constitutes the mechanism of knot formation (see figure 3.26). If the local concentration is too high to keep the mass distribution process constant, a new rivulet will appear.

With the formation of rivulets the mobility of the polymer molecules drops completely, and the rivulets dry into bundles.

This sequence presents a mechanism of polymer deposition during the moving contact line processes on hydrophobic surfaces, which has not been described before. The application of this model gives the ground for an explanation of all the obtained experimental data.

The increase of the PSSA concentration brings about the increase of the solution viscosity and therefore provides for a large lag region. This leads to the increase of the "trapped" polymer mass, which is then distributed into a larger number of rivulets with a larger amount of polymer molecules per each rivulet, see figure 3.12. Also a higher PSSA concentration results in the increase of the polymer molecules entanglement and leads to the increase of the number of knots, as well as to a broad bundles diameters distribution, see figure 3.13.
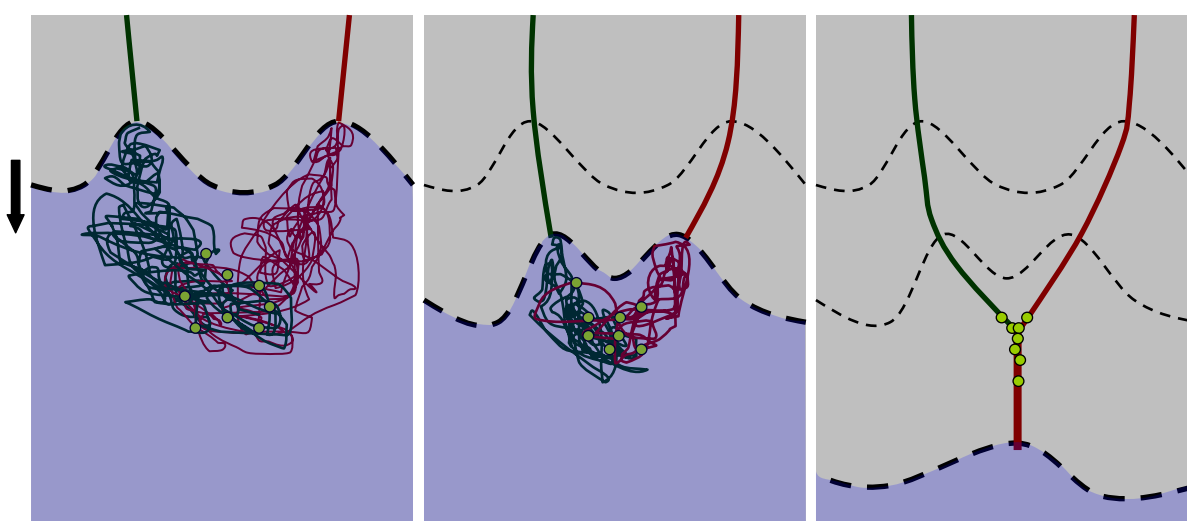

Figure 3.26: Mechanism of knots formation. Dots indicate the points where polymer molecules have entanglements. The black arrow on the left indicates the direction of the contact line movement.

According to the proposed model, the increase of the liquid phase movement speed causes the increase of the intensity of the internal flows. This factor inhibits the process of mass transfer into the slip region, because the internal flows sustain the circular movement of molecules, this process being even stronger for the entangled polymer molecules. The higher the movement speed the less mass is transferred into the slip region and the less mass is distributed into rivulets. The lower the number of bundles along the contact line, the lower the number of knots and hence the narrower the bundles diameter distribution obtained in this case, refer to figure 3.13. The expectation is that a threshold will appear when intensive internal flows caused by a high movement speed will completely inhibit the transfer of the mass into the slip region and no deposition will take place. Employing extrapolation of the experimental data I may suggest that for PSSA M_W = 6 900 000 g/mol with a concentration of 10 mg/mL this threshold equals ~$2.5*10^{-2}$ m/s. However no experimental proof of the above statement has been obtained due to the take off effect for a moving droplet.

At the same time the increase of the liquid phase movement speed shifts the adsorbed mass *vs.* concentration threshold in the direction of a lower concentration. The possible explanation of this may be the earlier lag region formation caused by the increased distortion on the receding area.

The dependence of the depositing polymer mass on the polymer M_W can be explained by the assumption that the increase of viscosity leads to the increase of the lag region and therefore to the increase of the trapped polymer mass. This explains the fact that the samples obtained for a polymer solution with PSSA M_W = 6 900 000 g/mol display several bundles of ~10 nm in height, whereas for PSSA M_W = 200 000 g/mol a few bundles with the height of several nanometers can be registered, see figure 3.14. A low molecular mass PSSA M_W = 30 000 g/mol cannot form bundles at all because the lag region in this case is absent. Only extremely high concentrations of ~100 mg/mL lead to the deposition of a network-like structure, which may be explained by random pinning of the contact line during movement, instead of rivulets formation. The number of the polymer molecules entanglements is too low to develop into a stable rivulet.

In cases when the concentration is too low to form a lag region, no deposition was registered. This permits me to talk about a threshold for the deposited mass – concentration dependence, see figure 3.15.

Addition of a small amount of bivalent salt of ~0.01 mg/mL to the PSSA solution brings about a reduction of the number of knots because more entangled structures are more likely to go into a single rivulet than to produce several separate rivulets. However, addition of large amounts of salt results in agglomeration of the polymer molecules and in fluctuations of the polymer molecules concentration along the rivulet. In this case root-like nanostructures are formed - intermediate structures between bundles and a network, see figure 3.16.

The proposed model does not take into account the specific forces existing between the polymer molecules and the surface. In actual experiments different surface defects and impurities are present and these may cause polymer-surface interactions which, no doubt, will affect the results and their interpretation on the basis of the proposed model. The higher the hydrophilicity of the surface the stronger the polymer-surface interaction, and for a strong polymer-surface attraction there exists a molecular combing effect, when the key factor of the polymer adsorption is the superiority of the polymer-surface interaction under others factors. In my opinion, the way a researcher can determine whether a specific case belongs to the combing driven adsorption or to the forced deposition caused by the push out of polymer molecules from solution, is by searching for the deposited mass - concentration dependence threshold. The appearance of the threshold will indicate the forced deposition nature of the process of the nanostructures formation.

3.5. Conclusion

In this chapter I present advanced deposition techniques for obtaining highly oriented polymeric nanostructures with known orientation by utilizing the moving contact line. A detailed investigation of the deposition process has made it possible to determine that each nanostructure within the oriented arrays is aligned perpendicular to the local receding contact line. This finding provides a possibility to control the

orientation of nanostructures on the macroscopic level by changing the movement direction and the shape of the receding contact line. It has also been found that the formed nanostructures display an extremely high aspect ratio. Typically, PSSA bundles have the diameter of several nanometers and the length of many microns.

The number of bundles per micron, their height distribution, and the number of knots depend on the speed of the droplet movement and on the solution concentration. The higher the movement speed the lower the number of bundles is. At the same time, the structures formed at higher deposition speeds usually possess a less branched morphology, and are thinner. At the same time, the decrease of the polyelectrolyte solution concentration derives similar changes in the morphology of the resulting structures as the increase of the deposition speed.

It has been found that there exists a critical polyelectrolyte concentration below which bundles are not formed on the surface and, in general, the deposition process becomes unstable and poorly reproducible. It has been further found that this critical concentration depends on the molecular weight of the polyelectrolyte and it decreases with the increase of the molecular weight or upon addition of multivalent ions. These observations suggest an important role of intermolecular interactions between the polyelectrolyte chains that occur in solutions. In this case, promotion of the intermolecular interactions (entanglement and ionic bonding) favors the formation of very long well-aligned and continuous fibers.

A method of preparion of 1D nanostructures has been found to be fairly universal and applicable to a wide range of polyelectrolytes of different nature (charge, hydrophobisity) and also to numerous kinds surfaces. The only prerequisite for a successful fabrication of aligned polyelectrolyte structures is a low adhesion force between the droplet with PE water solution and the surface.

As such, surfaces with a high enough hydrophobisity (e.g., PDMS, PTFE, PS, PMMA, PGMA, PtBA) are suitable for preparation of nanostructures, whereas, hydrophilic surfaces (e.g., silica, glass, P2VP) are not suitable substrates.

A model describing the polymer deposition on hydrophobic surfaces during the moving contact line processes has been proposed. The application of this model provides the ground for an explanation of all the obtained experimental data.

Chapter 4.

One-dimensional self-assembled nanostructures templated by polyelectrolyte molecules

4.1. Introduction

In the previous chapter I discussed the preparation of quasiperiodic aligned and oriented one-dimensional nanostructures formed on hydrophobic surfaces when drops of polyelectrolyte solutions are drawn along hydrophobic surfaces. Because of their one-dimensionality, the resulting nanostructures, in principle, can be envisaged for application in nanoelectronics, in wiring of other nanoelectronic devices and their integration into circuits. Unfortunately, the formed nanostructures are not electrically conductive and therefore, directly are not suitable for the above-mentioned applications. The advantage, however, is that the nanostructures are chemically reactive due to the presence of charged groups in each repeat unit that can be utilized for development of other useful properties, such as (semi)conductivity. There are two major routes to modify the properties of the polyelectrolyte nanostructures: 1) arrangement of useful materials involving non-covalent interactions (ionic, hydrogen bonding); 2) chemical assembly, i.e. a conduction of selective chemical reactions in close vicinity to the nanostructures leading to the formation of useful materials chemically bound to the nanostructures. In the present thesis I use both of these strategies, however the present chapter deals with the first one.

One of the most powerful approaches for arrangement of various useful molecules into large-area flat or patterned structures is self-assembly to form self-assembled monolayers (SAMs). SAMs are molecular assemblies that form spontaneously by immersion of a substrate into a solution of the appropriate surfactant interacting with the substrate by anchoring groups.[Ulman1996] SAMs have attracted widespread interest

since they are a versatile tool for surface modification in a wide range of technologies (e.g. corrosion resistance, biosensors, microelectronics, etc.).[Laibinis1989] For many applications, SAMs must be laterally structured and positioned in a desired location on the surface. Micrometer-scale patterns can be fabricated using the so-called microcontact printing (µCP) technique, introduced by Whitesides and co-workers.[Kumar1994, Jeon1997] When a properly structured elastomeric stamp coated with the appropriate ink is brought into contact with the substrate, the ink molecules transfer onto the substrate, thus forming a positive replica. In this case, the deposition is driven by the interactions between the substrate and the anchoring groups of the ink compound, while specific interactions between the ink molecules are responsible for their ordering.

Alkyl-phosphonic acids (APAs) were shown to assemble on a number of oxide surfaces such as TiO_2, Al_2O_3, SiO_2, or mica.[Woodward1996, Neves2000, Neves2001, Messerschmidt2001, Nie2002, Textor2000] Micrometer-scale patterns of APAs on the previously mentioned surfaces can be prepared using the µCP techniques with the aid of structured polydimethylsiloxane (PDMS) stamps. In this chapter, I propose an alternative approach to the APAs patterns. With the fabrication of conductive polymer nanostructures being our prospective task, we used (12-pyrrol-1-yl-dodecyl)-phosphonic acid (Py-DPA) with a polymerizable pyrrole head group (see figure 4.1).
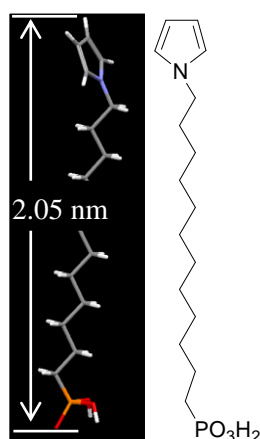

Figure 4.1: Chemical structure of Py-DPA: (12-pyrrol-1-yl-dodecyl)-phosphonic acid with a pyrrole head group.

Besides the metal oxide surfaces, Py-DPA in its ionized form also has an affinity towards positively charged polymers (polycations), but not to polyanions, like the PSSA discussed in the previous chapter. Indeed, mixing water solutions of Py-DPA with the linear polycation poly(methacryloyloxyethyldimethylbenzylammonium chloride) (PMB) [Kiriy2002] at pH 11 leads to a water-insoluble PMB-Py-DPA polyelectrolyte-surfactant complex. We applied this reaction to assemble Py-DPA along the polycation template. Previously, polyelectrolyte molecules were used as templates for selective deposition of various inorganic nanoparticles and conductive polymers.[Kiriy2002, Kiriy2002-2, Kiriy2002-3, Kiriy2003, Bocharova2005, Braun1998, Bjork2005, Nakao2005] However, the arrangement of SAM-forming compounds directed by individual surface-immobilized polyelectrolyte molecules is a less explored area of research.[Severin2004]

It was recently found that natural [Michalet1997] and synthetic [Bocharova2006] polyelectrolytes can be stretched and aligned by hydrodynamic forces upon deposition on hydrophobic surfaces. Furthermore, Ohtani *et al.* demonstrated that stretched DNA molecules can then be transferred by printing onto other substrates, if an elastic PDMS stamp is used as a support.[Nakao2003] This approach is a useful extension of Whitesides µCP technique, allowing for reduction of the feature size to the width of molecular structures.

In this chapter, I make a further step, demonstrating that:

- *The approach introduced by Ohtani et al. is also applicable to more flexible synthetic polyelectrolyte molecules;*
- *Produced 1D polyelectrolyte structures can act as templates for the directed assembly of APAs, playing a role similar to that of the lithography-made PDMS structures in the µCP technique.*

4.2. Materials and experimental procedures

Fabrication of PDMS stamps. To fabricate PDMS stamps, the Dow Corning WL-5351 photopatternable spin-On silicone from the Dow Corning corporation was spun

coated (500 rpm, 30 sec) onto freshly cleaned silicon wafers, irradiated at the wavelength of 254 nm (1000 J/cm^2), and cured for 1 h at 150 °C.

Stretching of PMB on PDMS stamps. A 50 µL drop of PMB or PSSA solutions (5 mg/mL in water) was deposited onto a PDMS stamp and moved by a pipette along the stamp with a velocity of approximately 2 mm/s.

Deposition of Py-DPA on PDMS stamp. A drop of Py-DPA basic water solution (1, 3, 5, or 10 mg/mL, pH 11, ammonia) was placed on a PDMS stamp with or without PMB nanostructures and moved by a pipette along the stamp with a velocity of approximately 2 mm/s. However, the deposition of Py-DPA was only observed when the PMB structures were present on the stamp.

Printing of Py-DPA on mica or Si wafer. Py-DPA structures were transferred from PDMS stamps onto freshly cleaved mica or clean Si wafers, when the stamp bearing the Py-DPA structures was gently pressed against the surfaces of mica or the Si wafer for a few seconds and afterward peeled off.

AFM measurements. A NanoScope IV-D3100 AFM instrument (Digital Instruments) was operated in both tapping and contact modes. Friction force images were obtained simultaneously with topography images with the AFM operating in the contact mode. For this, silicon cantilevers (Nanosensors, Inc.; type: CONT-W) 444 µm long with a tip radius of about 20 nm and a resonance frequency of 10-16 kHz were used. All images were recorded in air at a relative humidity of about 40%.

4.3. Results and discussion

4.3.1. Stretching and printing of polycation molecules

In the first step, relatively thick and smooth WL-5351 films were prepared on Si wafers, as described in detail in chapter 3. We realized that the approach developed for

patterning of polyanions (discussed in the previous chapter) is also applicable to structuring of polycations. To create patterns of stretched and aligned molecules, a drop of the PMB solution was deposited with the aid of a pipette onto a micrometer thick WL-5351 film. Because of the high hydrophobicity of the surface (the water contact angle is about 105°), the droplet of the PMB solution weakly interacts with the surface and remains adhered to the pipette. This fact allows moving the droplet in the desired direction with a controlled velocity by moving the pipette (figure 3.4). Although visually the droplet does not wet the WL-5351 surface, an adsorption process obviously takes place, which leads to large area patterns of oriented PMB fibers. Figure 4.2 shows a typical AFM image of the resulting tree-like PMB structures on the WL-5351 substrate. From the large size of the structures (diameter up to 10 nm and length up to several hundreds of micrometers) and from the brush-like morphology, we conclude that fibers are of multimolecular origin. Typically, the fibers have the largest diameter (5-10 nm) in their trunk part and are significantly thinner (1-3 nm) in the branches. The size of the structures and the number of knots can be controlled by the deposition conditions. In particular, deposition from a more concentrated polycation solution and application of a lower drawing velocity result in fibers with a larger diameter. 1D structures can be easily transferred onto mica or Si wafers by contact printing if the WL-5351 film with the immobilized PMB fibers is pressed against these surfaces (molecular stamping).
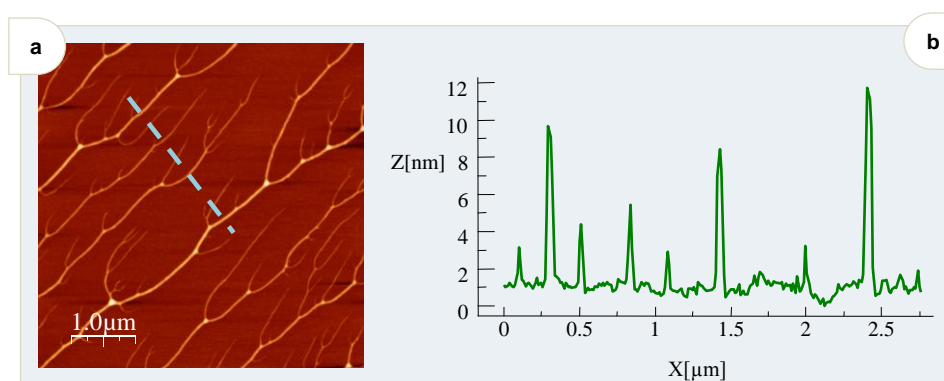

Figure 4.2: (a) AFM topography and (b) cross-section of PMB fibers deposited on PDMS by the "drawing" technique.

To understand the role of electrostatic forces in the assembling process of Py-DPA, negatively charged polystyrenesulfonic acid (PSSA) was also examined. Similar

patterns of oriented PSSA nanofibers can be prepared using the same drawing technique when PSSA solutions are used as the ink compound (see figure 3.4). Since both positively and negatively charged polyelectrolytes behave similarly in these experiments, the adsorption is, obviously, not driven by the electrostatic forces, and instead, hydrophobic interactions between the molecules and the surface are more important. Although the mechanism of the deposition and adsorption processes is not understood in detail, the important role of hydrodynamic forces causing stretching and alignment of chains may be postulated.[Bensimon1995] In addition, dewetting of the hydrophilic polycation molecules on the hydrophobic surface may be assumed to lead to segregation of the polyelectrolyte molecules into multistranded structures.

Much interest focuses on the formation of SAMs where different order and functionalities with thin films can be generated. SAMs of APA deposited on mica from apolar organic solvents were extensively investigated.[Woodward1996, Neves2000, Neves2001, Messerschmidt2001, Nie2002] We attempted to use the polyelectrolyte structures for dedicated deposition of charged SAMs. Thus, we bring the electrostatic forces into play for the arrangement of ionized Py-DPA SAMs along charged polycation molecules, when water is utilized as a solvent.

4.3.2. Formation of Py-DPA SAMs on mica from water solutions

A drop of Py-DPA dissolved in water at pH 11 was placed on mica for 20 s and afterwards dried under argon flux. Despite the fact that both the mica surface and ionized Py-DPA molecules are of the same charge (negative), adsorption takes place and results in 4 nm thick terrace structures (see figure 4.3). We consider the hydrophobic interactions to be the main driving force for the formation of SAMs in this case. Indeed, Py-DPA molecules being dissolved in basic water experience unfavored interactions between the hydrophobic alkyl chains and water environment. The molecules are significantly stabilized in the adsorbed state, if they form closely packed layered ensembles, maximizing favored van der Waals interactions between the stacked alkyl chains and eliminating unfavored contacts of hydrophobic fragments with the water.

However, most of the terraces can be washed away upon brief rinsing with water, and left over are, predominantly, randomly oriented elongated 1D structures, 2-2.5 nm in height, 20-30 nm in width, and up to 3 μm in length (see figure 4.4). A minority of the structures resembles round-shaped disks, 4 nm in height and a several hundred nanometers in diameter. The formation of these 1D structures is quite a reproducible process, and within the given sample, most of them have the same thickness (and hence the same number of layers). We suggest that the structures in figure 4.4 originate from the terrace-like structures (see figure 4.3) and are formed upon kinetically controlled removal of the less ordered and therefore better soluble material during washing. The comparison of AFM topography and phase images gives an important insight into the organization of these nanostructures. As seen from figure 3b-e, the 1D nanoparticles and disks appear on the phase images as light and dark structures, respectively.
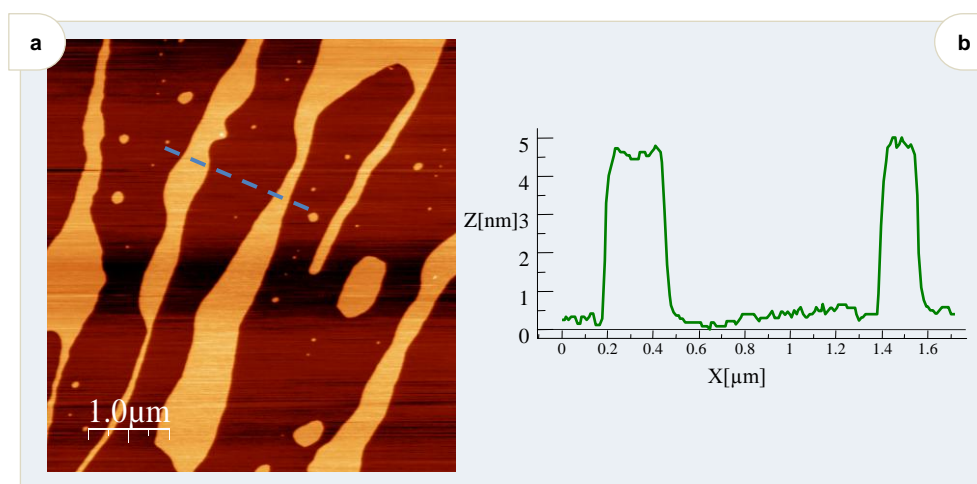

Figure 4.3: (a) AFM topography image of Py-DPA SAMs deposited on mica from water solution (left) and the chemical structure of Py-DPA (right). (b) Cross-section taken as shown in panel a.

This implies different interactions between the tip and the sample in different sample regions and with the end groups of the SAMs. Here, the dark color of the phase images corresponds to quite weak tip-sample interactions with soft material, whereas the bright color reflects strong interactions with hard surfaces. Hence, the darker color of the disk structure indicates that the SAMs here are terminated with soft alkyl groups, whereas the lighter color of the 1D structures reflects termination by harder phosphonic acid groups. It is interesting to note that the background surface between the

nanoobjects is also not uniform (figure 4.4d, e). The majority of the surface of the phase image has the same color as the disk structures (dark), which implies the same termination (i.e. by alkyl groups). The surface, however, contains approximately 1 nm deep holes (dark spots in the topography image and bright spots in the phase image), which obviously represent small regions of uncovered bare mica surface. The bright color on the phase image indicates the hard nature of the mica surface.
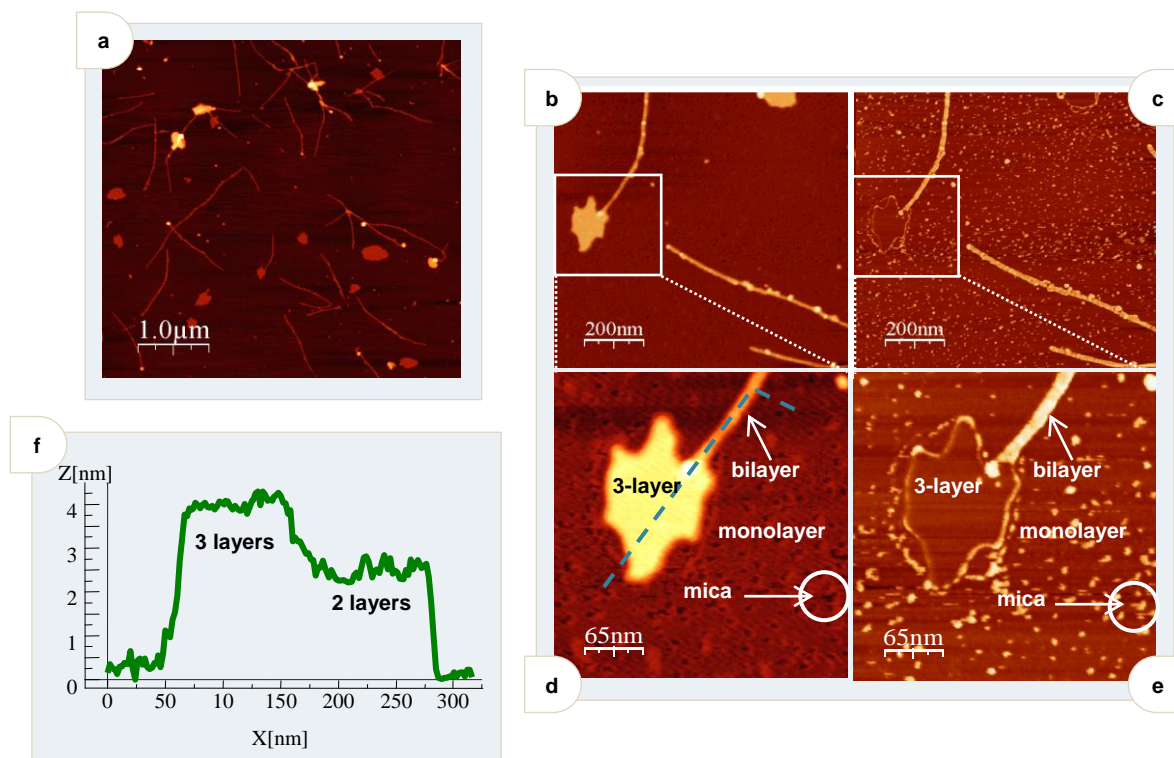

Figure 4.4: AFM topography (a, b, d) and phase images (c, e) of the Py-DPA SAM deposited on mica and briefly rinsed with water; (f) cross-section is taken as shown in plane d.

Thus, the image in figure 4.4 can be assigned as follows: (i) mica is almost completely covered by a basic monolayer of Py-DPA molecules stacked normal to the surface, where the molecules are oriented with their phosponic acid ends toward the mica surface and terminated by alkyl groups at the surface; (ii) 4 nm thick disks consist of three layers (bilayers located on top of the basic monolayer) and are also terminated by alkyl groups; and (iii) 1D structures are bilayers (monolayer located on top of the basic monolayer) and are terminated by phosphonic acid groups.

It is also worth mentioning that the thickness of the first layer on mica is thinner than the molecular length of Py-DPA and also less than the thickness of the upper Py-

DPA layers. The thickness of the upper layers approaches the theoretical molecular length of about 2 nm. This fact reflects the different packing modes of Py-DPA molecules within the first and next layers. As was similarly reported for APA monolayers, the molecules arranged directly on mica can be assumed to be significantly tilted and/or disordered. In contrast, the multilayers on top of the first layer self-assemble without much interaction with the mica lattice and thus can adopt an energetically more favored arrangement of close packed molecules oriented normal to the surface.
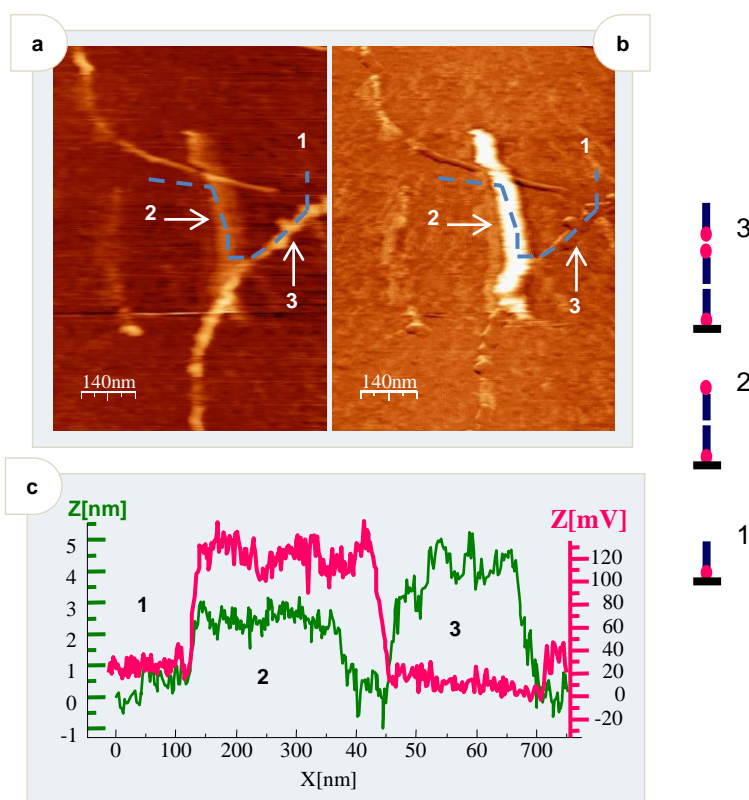

Figure 4.5: AFM topography (a) and friction mode images (b) of the Py-DPA SAM deposited on mica and briefly rinsed with water; (c) cross-section is taken as shown in (a) and (b); here the green and red line correspond to the topography and friction mode signals, respectively.

Additional information about the organization of SAMs is obtained from friction force AFM, a particular mode of contact mode AFM.[Nie2002] Figure 4.5 shows simultaneously recorded topography and friction force images of the 1D structures. As was already discussed, the mica surface is covered by the Py-DPA basic monolayer

terminated by pyrrole groups that provide rather weak tip-sample interactions. The bright object in the friction image with the height of about 2 nm above the background is the Py-DPA bilayer (the monolayer on top of the basic monolayer), terminated by phosphonic acid groups. As reported earlier for APAs, highly polar phosphonic acid groups strongly interact with the silicon tip.[Nie2002] The structures of about 4 nm in height are three layers (bilayer on top of the basic monolayer) and are terminated by pyrrole groups. The fact that the basic monolayer and the three layer structure are both terminated in the same way explains the poor contrast in the friction image despite a good topography contrast.

For comparison, Py-DPA SAMs were also prepared from chloroform. 1D structures were not formed in this case, neither right after deposition nor after subsequent rinsing of the sample with water or chloroform (not shown). The morphology of the resulting Py-DPA SAM in this experiment is close to the morphology of the previously described APAs SAMs on mica.[Woodward1996, Neves2000, Neves2001, Messerschmidt2001, Nie2002]

4.3.3. Assembling Py-DPA on polyelectrolyte patterns

We first tested the possibility to arrange Py-DPA onto PMB molecules immobilized on mica. We assumed that positively charged PMB molecules adsorbed onto mica would locally reduce mica's negative surface charge and therefore may serve as binding sites for preferential adsorption of negatively charged Py-DPA molecules. To realize this idea, PMB molecular coils were adsorbed onto mica, and afterwards, Py-DPA was deposited from a diluted water solution (0.01 mg/mL). I found that the surface immobilized PMB molecules indeed formed complexes with Py-DPA which was indicated by the increase of the thickness of the template molecules from about 1 nm to about 1.8 nm, see figure 4.6. However, the adsorption of Py-DPA was not selective in this case, and randomly located Py-DPA islands and 1D nanostructures were also registered on the surface (such as is shown by the arrow in figure 4.6c). Thus, it is very difficult to control the morphology of Py-DPA SAMs when mica is used as the support.
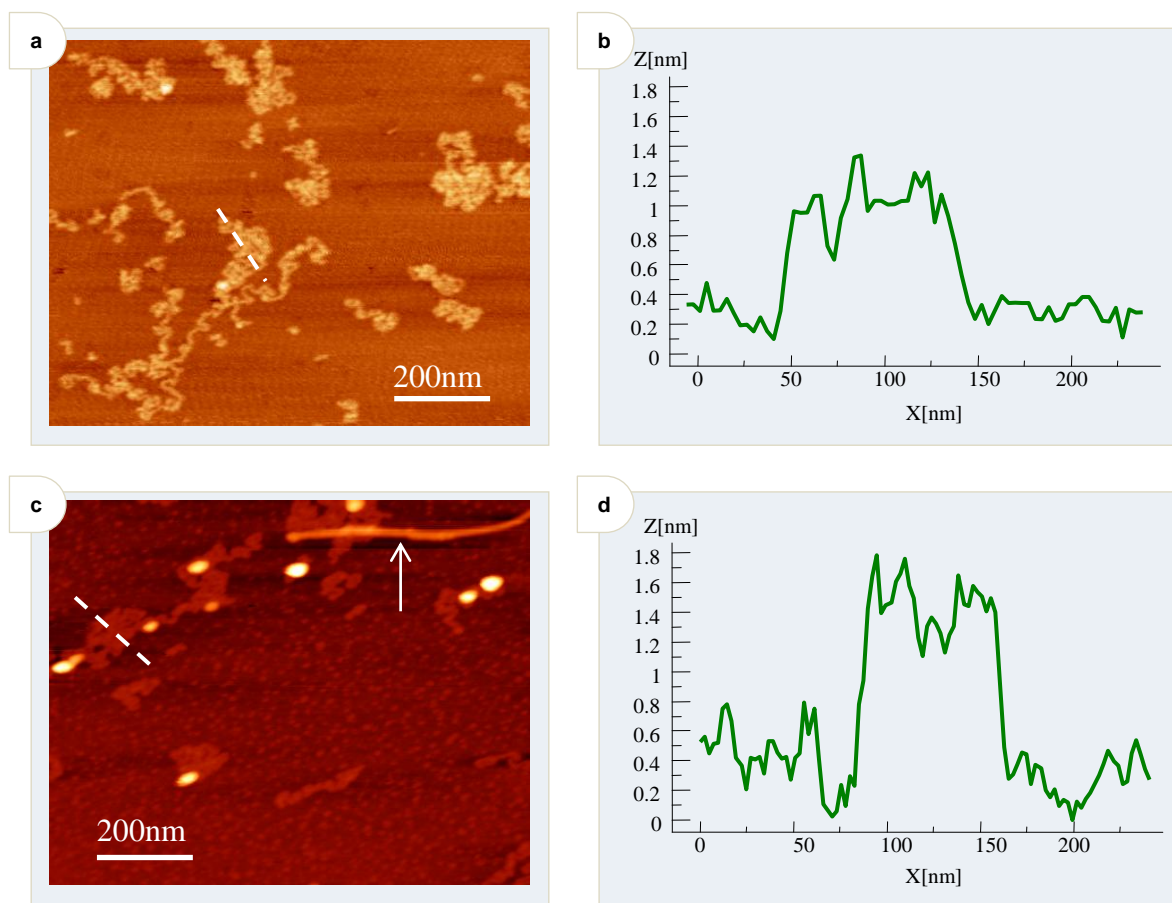
Figure 4.6: AFM topography images of (a) PMB molecules deposited on mica and (c)
SAMs formed upon workup of mica-immobilized PMB molecules with diluted Py-DPA
water solution (0.01 mg/mL). (b and d) Cross-sections taken as shown in panels a
and c, respectively.

Controlled assembly of Py-DPA into 1D nanostructures was, however, achieved in
an alternative way. In the first step, PMB was stretched and aligned on a PDMS stamp
using the moving droplet technique (see first section). In the next step, utilizing the
same technique, we deposited Py-DPA from a solution in water at pH 11. For this, a
drop of Py-DPA solution was pulled along the pre-deposited PMB structures. As is seen
from the topography images (figure 4.2a *vs.* figure 4.7a), the resulting structures become
wider and higher (thickness increases from less than 10 nm to 15 nm). Even more
pronounced changes were found in the phase image. A much stronger phase contrast
for the resulting structures corroborates with the complexing of PMB with Py-DPA.
Utilization of more concentrated solutions of Py-DPA results in the deposition of still
more material, as indicated in figure 4.7e-k. Obviously, Py-DPA molecules are arranged

along PMB templates by electrostatic forces and act then as seeding sites for the deposition of additional Py-DPA. Although Py-DPA does not order uniformly along the PMB fibers, the templating effect of the 1D PMB structures is pronounced.
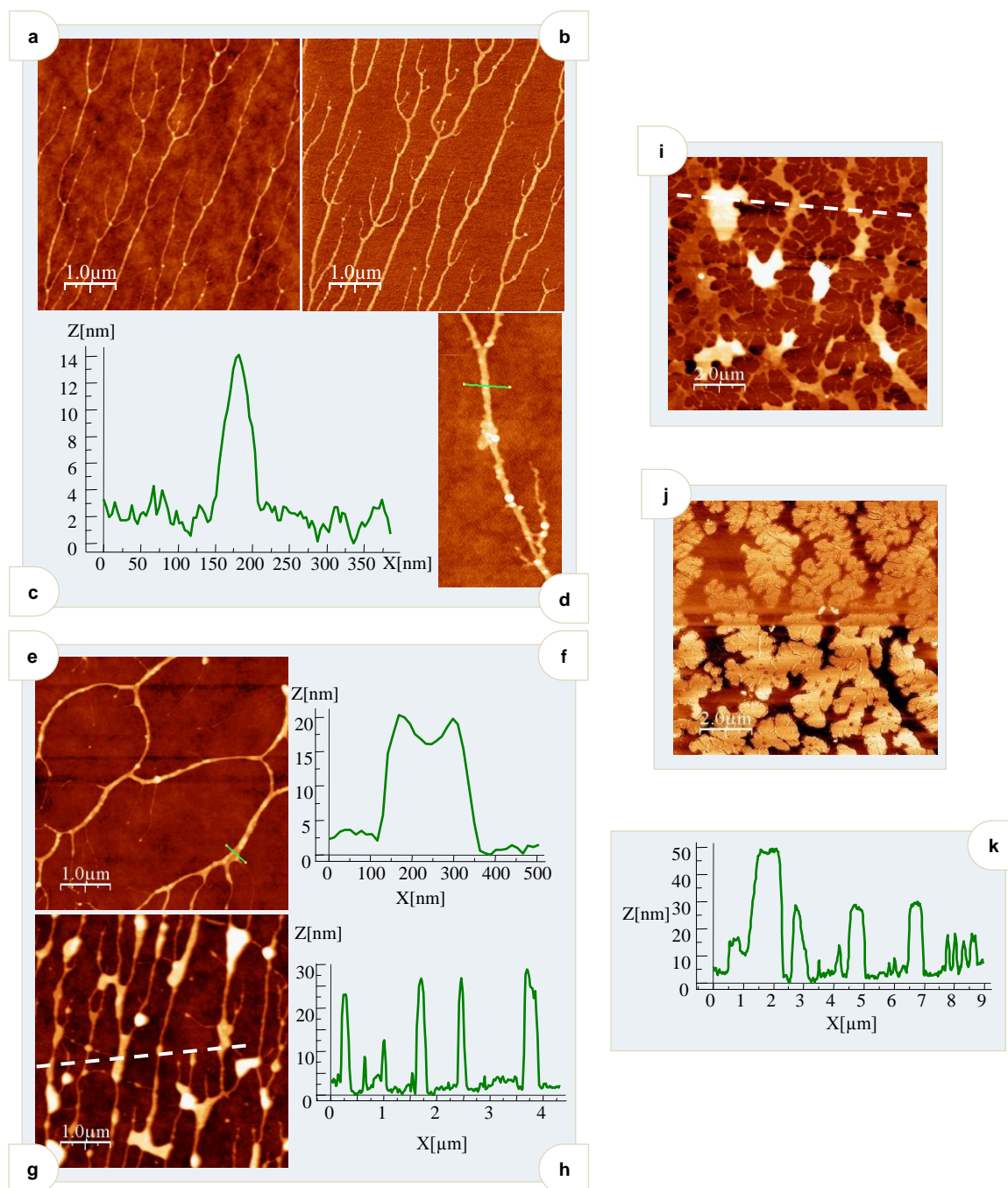

Figure 4.7: AFM topography (a, d, e, g, and i) and (b and j) phase images of Py-DPA SAMs formed on PDMS stamps upon the following procedure: PMB structures were developed by the drawing technique (pipette was filled with PMB solution); afterwards, Py-DPA was deposited using the drawing technique from water solutions with increasing Py-DPA concentrations: (a-d) 1 mg/mL; (e and f) 3 mg/mL; (g and h) 5 mg/mL; and (i-k) 10 mg/mL. (c, f, h, and k) Cross-sections taken as shown in panels d, e, g, and i, respectively.

Additional confirmation of successful deposition of Py-DPA along PMB comes from a control experiment. Instead of the Py-DPA solution, we used water with the same pH 11 during the deposition stage. Brief contact with water in this case resulted in partial debundling of the PMB fibers, revealing single PMB strands (Extensive rinsing of the PMB fibers immobilized on the PDMS stamp leads to complete removal of PMB molecules). Obviously, this occurs due to repulsive interactions of like charges of PMB molecules ionized upon contact with water, see figure 4.8. The debundling process, however, does not proceed, neither if PMB bundles are treated with Py-DPA solution nor if the resulting PMB-Py-DPA structures are treated with water. Water insolubility of the PMB-Py-DPA complex causes the observed persistence of the structures against washing and debundling.
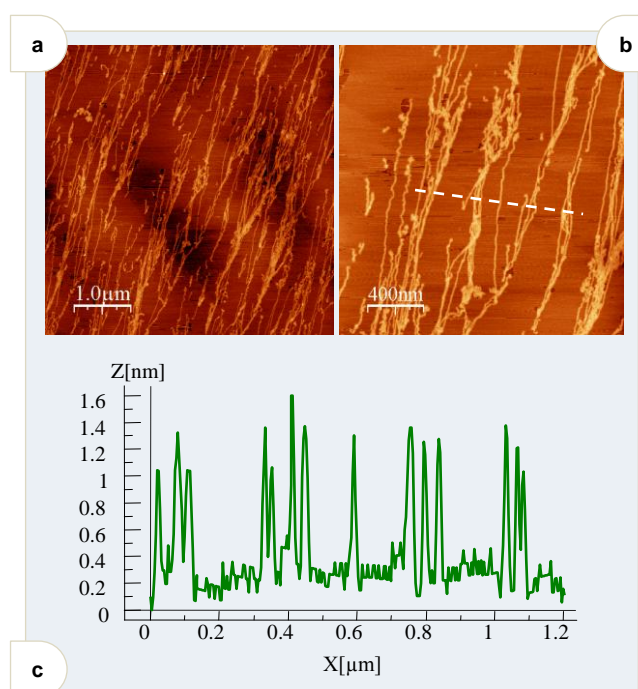

Figure 4.8: Result of the control experiment when PMB fibers were deposited onto PDMS stamp by the drawing technique and then treated with water using the same drawing technique: (a and b) AFM topography images and (c) cross-section as shown in panel b.

In another control experiment, we demonstrated the important role of PMB templates for the formation of Py-DPA SAMs on PDMS. Particularly in the absence of PMB templates Py-DPA deposition on PDMS is not observed. In the next control

experiment, a negatively charged polyelectrolyte (PSSA) was used as a template instead of positively charged PMB. In this experiment, oriented PSSA nanofibers were deposited on the PDMS stamp (figure 3.12), and then a Py-DPA water solution was applied with the help of the same drawing technique. The deposition of Py-DPA was not observed, and the procedure only resulted in the removal of most of the PSSA template during washing (not shown). Thus, these control experiments clearly reveal the crucial importance of electrostatic interactions in the controllable formation of SAMs.
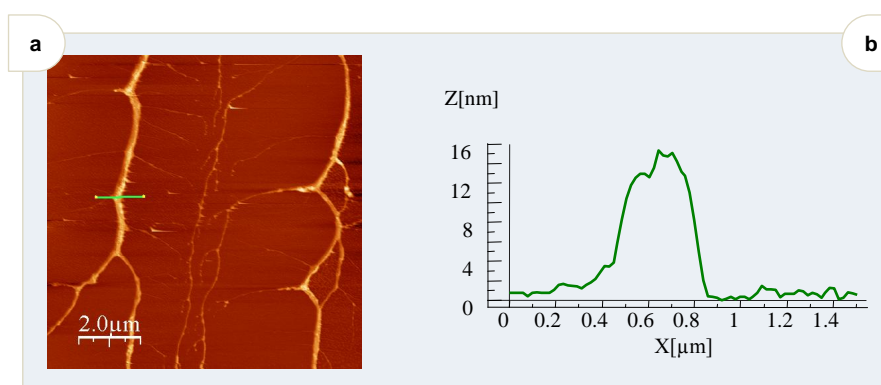

Figure 4.9: (a) AFM topography image and (b) cross-section of Py-DPA structures transferred from a PDMS stamp onto mica: branched treelike morphology of the structures similar to the morphology of PMB Py-DPA structures on PDMS highlights a successful transferring step.

Structures of Py-DPA-PMB produced this way can be transferred onto a mica surface by printing. For this, the PDMS stamp was gently brought in contact with freshly cleaved mica for a few seconds. Figure 4.9 demonstrates the resulting Py-DPA structures on mica. Their morphology resembles the morphology of the previous structure on PDMS, confirming a successful transfer.

4.4. Conclusion

In this chapter, I present the proof-of-concept for the conversion of polyelectrolyte patterns into corresponding patterns of self-assembled multilayers of oppositely charged amphiphiles. In particular, aligned 1D polycation structures on a PDMS stamp were prepared by moving a droplet of the polycation solution over the surface. These

structures were used as templates for assembling amphiphile molecules, bearing a charge opposite to the charge of the template. SAMs of Py-DPA can then be transferred onto mica or silica wafers. We believe that these nanostructures with polymerizable pyrrole head groups will be useful for creation of electrically conductive patterns of conjugated polymers. Although the PMB template fibers used in this work are usually branched and irregularly spaced, the regularity of the patterns can be further optimized, especially for less hydrophobic polyelectrolytes. Furthermore, a combination of the self-assembly approaches with the traditional lithographic methods could be a promising way toward ordered patterns of polyelectrolyte templated SAMs.

Chapter 5.

Electrically conductive nanowires based on polyelectrolyte nanostructures

5.1. Introduction

As was discussed in the previous chapter, there are two major routes for utilization of nanostructures formed by polyelectrolyte molecules: 1) arrangement of materials involving non-covalent interactions; and 2) chemical assembly, i.e. conducting selective chemical reactions in close vicinity to the nanostructures. The second route was used in this chapter and quasiperiodic aligned and oriented nanostructures were utilized for fabrication of electrically conductive one-dimensional nanowires.

In fact, 1D systems are the smallest structures that can be used for efficient transport of electrons and are thus critical to the function and integration of these nanoscale devices. Because of their high surface-to-volume ratio and tunable electron transport properties due to quantum confinement effect, their electrical properties are strongly influenced by minor perturbations. Compared to 2D thin films where binding to the surface leads to depletion or accumulation of charge carriers only on the surface of a planar device, the charge accumulation or depletion in 1D nanostructure takes place in the "bulk" of the structure thus giving rise to considerable changes in the electrical properties. 1D nanostructures thus avoid the reduction in signal intensities that are inherent in 2D thin films as a result of the lateral current shunting. This property of 1D nanostructures provides a sensing modality for label-free and direct electrical readout when the nanostructure is used as a semiconducting channel of a chemiresistor or field-effect transistor. Such label-free and direct detection is particularly desirable for rapid and real-time monitoring of receptor–ligand interaction with a receptor-modified nanostructure, particularly when the receptor is a biomolecule

such as an antibody, DNA or protein. This is critical for clinical diagnosis and biowarfare agents detection applications. Additionally, the sizes of biological macromolecules, such as proteins and nucleic acids are comparable to nanoscale building blocks. Therefore, any interaction between such molecules should induce significant changes in the electrical properties of 1D nanostructures. Furthermore, 1D nanostructures offer new capabilities not available in larger scale devices (for example, study of single molecule properties).

A good method for generating 1D nanostructures should enable simultaneous control of the dimensions, properties, and morphology. Recently, it was demonstrated that single polyelectrolyte molecules can be randomly deposited and stretched using the spincoating technique. These molecules were used as positive templates for conductive nanowires fabrication which makes them perspective candidates for fabrication of nanodevices and sensors. However, an important drawback of the developed method is its low reproducibility and uncontrolled orientation and positioning of the structures. In chapter 3 it was demonstrated that the morphology of nanostructures obtained using the contact line movement approach displays a range of structure variations from root-like to a single wire structure with a high anisotropy and aspect ratio. The number of nanostructures and their orientation can be controlled by way of adjusting the macroscopic parameters such as concentration, velocity of the contact line movement, MW and others.

Goal of this capter is:

- *Fabrication of electrically conductive conjugated polymer (polypyrrole) nanowires on the basis of 1D polyelectrolyte templates via selective polymerization*

5.2. Materials and experimental procedures

Polystyrenesulfonic acid (M_W 6 900 000 g/mol, PDI=1.3) was purchased from Polymer Standards Service, Mainz. Ammonium persulfate (APS), pyrrole (Py) and other chemicals were purchased from Aldrich.

Fabrication of PDMS Stamps. To fabricate PDMS stamps, Dow Corning WL-5351 photopatternable spin-On silicone from the Dow Corning corporation was spun coated (500 rpm, 30 sec) onto freshly cleaned silicon wafers, irradiated at the wavelength of 254 nm (1000 J/cm^2), and cured for 1 h at 150 °C.

Stretching of PSSA on PDMS stamps. A 30 µL drop of PSSA solutions (10 mg/mL in water) was deposited onto a PDMS stamp and moved by a pipette along the stamp with a velocity of approximately 2 mm/s.

Printing of PSSA from PDMS stamps. PSSA nanostructures were transferred from PDMS stamps onto different surfaces (freshly cleaved mica, clean Si wafers, flat polymer surfaces, silica-gold chip) as a stamp bearing the PSSA structures was gently pressed against the surfaces of interest for a few seconds and afterwards peeled off.

Synthesis of PPy nanowires. 50 µL of Py (3 mg/mL) and 50 µL of APS (30 mg/mL) solutions in deionized water were placed onto substrates with pre-deposited PSSA molecules for a limited time (10-60 seconds).

Conductivity measurements. 18-finger gold micro-electrodes were fabricated by photo-lithography on Si-wafer with an insulating SiO_2 layer (see figure 5.3). Using the Keithley 2400 Source-Measure Unit the voltage from 0.1 V to 1 V with step 0.1 V was applied. In each step 20 data points were recorded and the average value of current corresponding to a certain voltage was calculated.

5.3. Results and discussion

5.3.1. Stretching and printing of polyelectrolyte molecules

In the first step, relatively thick and smooth PDMS films were prepared on Si wafers. Then, to create patterns of stretched and aligned molecules, a drop of PSSA solution was deposited with the aid of a pipette onto a micrometer thick PDMS film.

Because of the high hydrophobicity of the surface (the water contact angle is about 105°), the droplet of the PMB solution weakly interacts with the surface and remains adhered to the pipette. This fact allows moving the droplet in the desired direction with a controlled velocity by moving the pipette (figure 3.4).
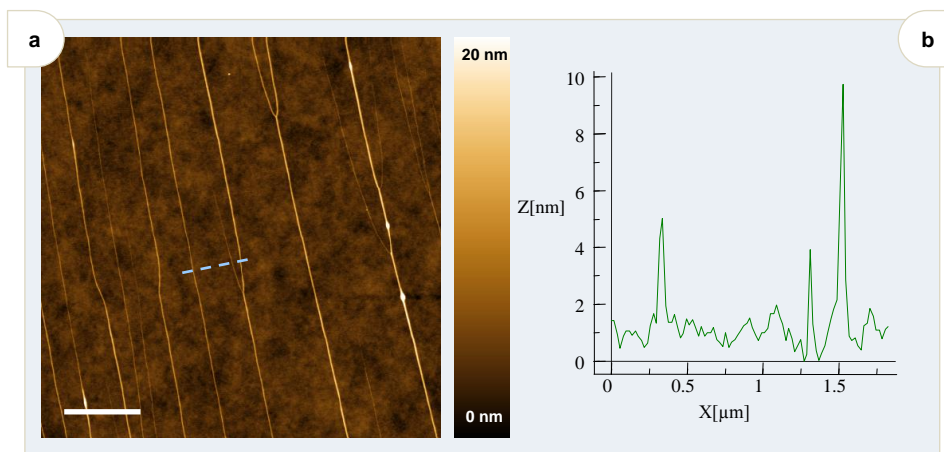

Figure 5.1: (a) AFM topography and (b) cross-section of PSSA fibers deposited on PDMS by the "drawing" technique. Scale bar - 2µm.
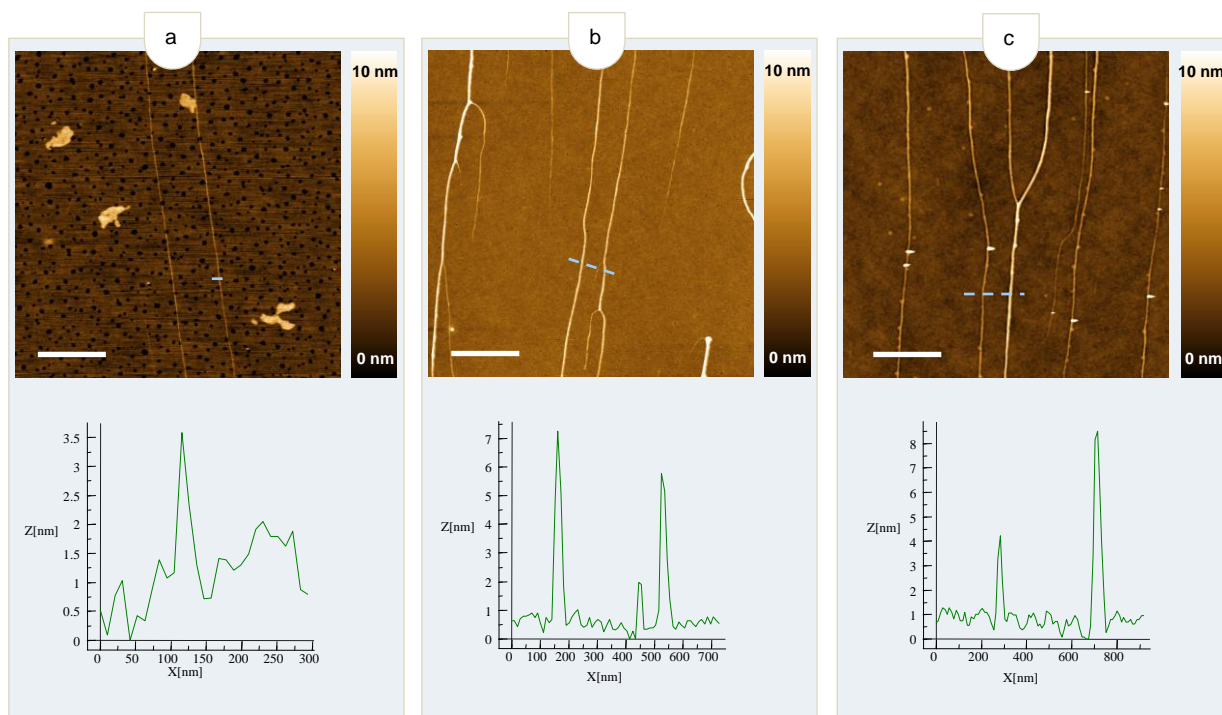

Figure 5.2: AFM images and cross-sections of the nanostructure printed from a PDMS stamp onto different surfaces: (a) partly dewetted P2VP surface; (b) surface covered by PMMA; (c) surface covered by PtBuA. Scale bar - 1µm.

Although visually the droplet does not wet the PDMS surface, a deposition process obviously takes place, which leads to large area patterns of oriented PSSA fibers. Figure 5.1 shows a typical AFM image of the resulting PSSA structures on the PDMS substrate. Typically, the fibers have the largest diameter (5-10 nm) in their trunk part and are significantly thinner (1-3 nm) in the branches. The size of the structures and the number of knots can be controlled by the deposition conditions. In particular, deposition from a more concentrated polyelectrolyte solution and application of a lower drawing velocity results in bundles with a larger diameter. 1D structures can be transferred onto mica or Si wafers by contact printing if the PDMS film with the deposited PSSA fibers is pressed against these surfaces (molecular stamping).
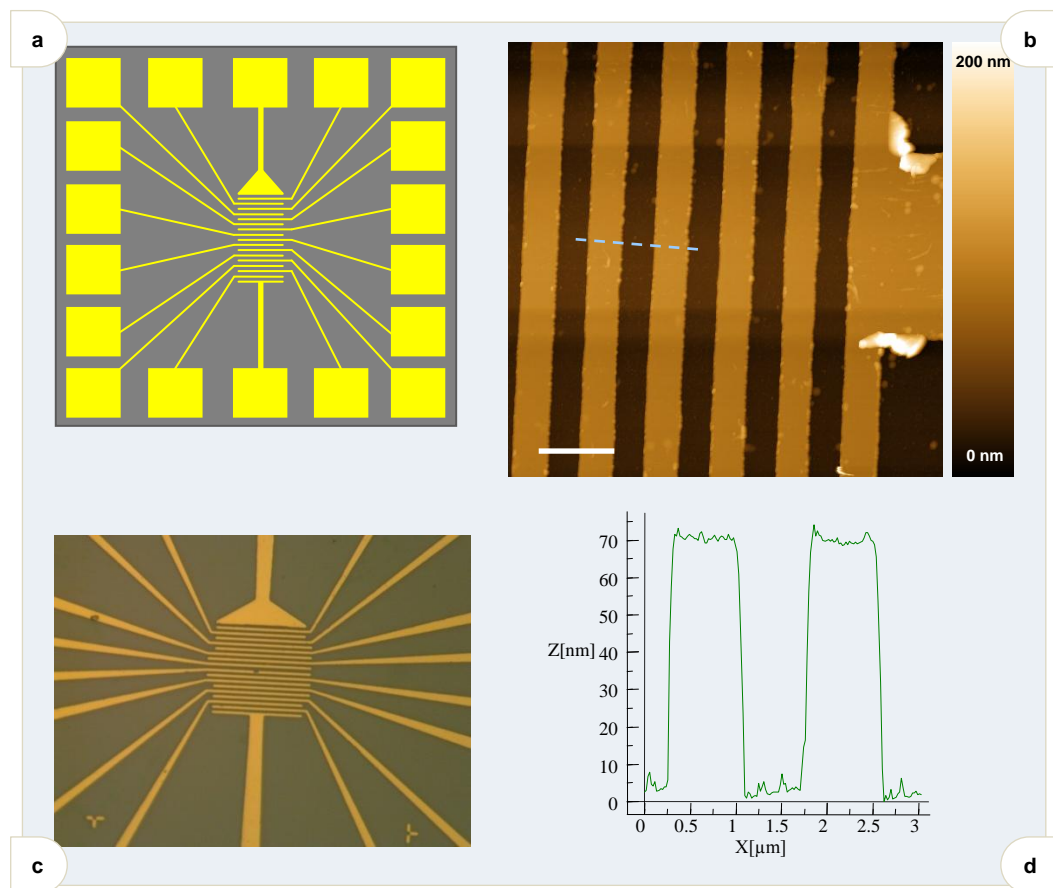

Figure 5.3: Silica-gold chip. (a) sketch of the silica-gold chip: periodic golden contacts go from the center to the edge and ends as large (millimeter size) flat rectangles; (b) AFM image and (d) cross-section of part of the central contacts; Scale bar - 2µm; (c) image of the central part of the silica-gold chip captured by optical microscope.

Firstly, I checked the possibility to transfer polyelectrolyte nanostructures onto different polymer layers fabricated on Si wafers, such as Si wafers coated with P2VP, PMMA or PtBuA. A transfer degree approaching 100% upon the microcontact printing (μCP) was found in these experiments which means that almost all structures initially present on PDMS were transferred onto the respective surface. As can be seen from figure 5.2 polyelectrolyte bundles keep orientation and shape constant (even on a partly dewetted surface, e.g., figure 5.2a).

However, the transfer of polyelectrolyte nanostructures onto a silica-gold chip was much less successes. Frequently, the polyelectrolyte nanostructures would not transfer onto a non-treated silica-gold chip at all or the transfer would occur just in several spots. The most probable reason for this is the complex profile of the silica-gold chip where the height changes from zero to ~100 nm every micron (see figure 5.3). Although, the PDMS material has certain flexibility, the relatively low thickness of the PDMS stamp of about one micron prevents achieving the proper contact between the PDMS stamp and the silica-gold chip surface.

5.3.2. Synthesis of polypyrrole nanowires using polyelectrolyte molecules

In the present work I have utilized a bundle of negatively charged synthetic polyelectrolyte molecules (PSSA) to grow continuous and conductive polypyrrole (PPy) nanowires via "electroless" deposition of PPy selectively along PSA molecules.

PSSA chains were deposited onto a silica-gold chip in the stretched conformation and afterwards Py and APS water solutions were employed. I varied the polymerization time at constant concentration of the pyrrole monomer. A continuous growth in height of the PPy nanowires from ~20 nm till ~100 nm was observed upon the increase of the polymerization time from 30 to 60 seconds. AFM investigations and conductivity measurements revealed a successful formation of PSSA-PPy nanowires, see figures 5.4 and 5.5.

In general, the growth of PPy nanowires can be arranged according to two schemes: a) precipitation of hydrophobic PPy nanoparticles preformed in solution onto

a hydrophobic PSSA-Py complex; and b) growing of PPy from a PSSA-Py complex. However, experiments previously performed by Bocharova support the "growing of PPy from a PSSA-Py complex" scheme for PPy nanowires formation.[Bocharova2005]
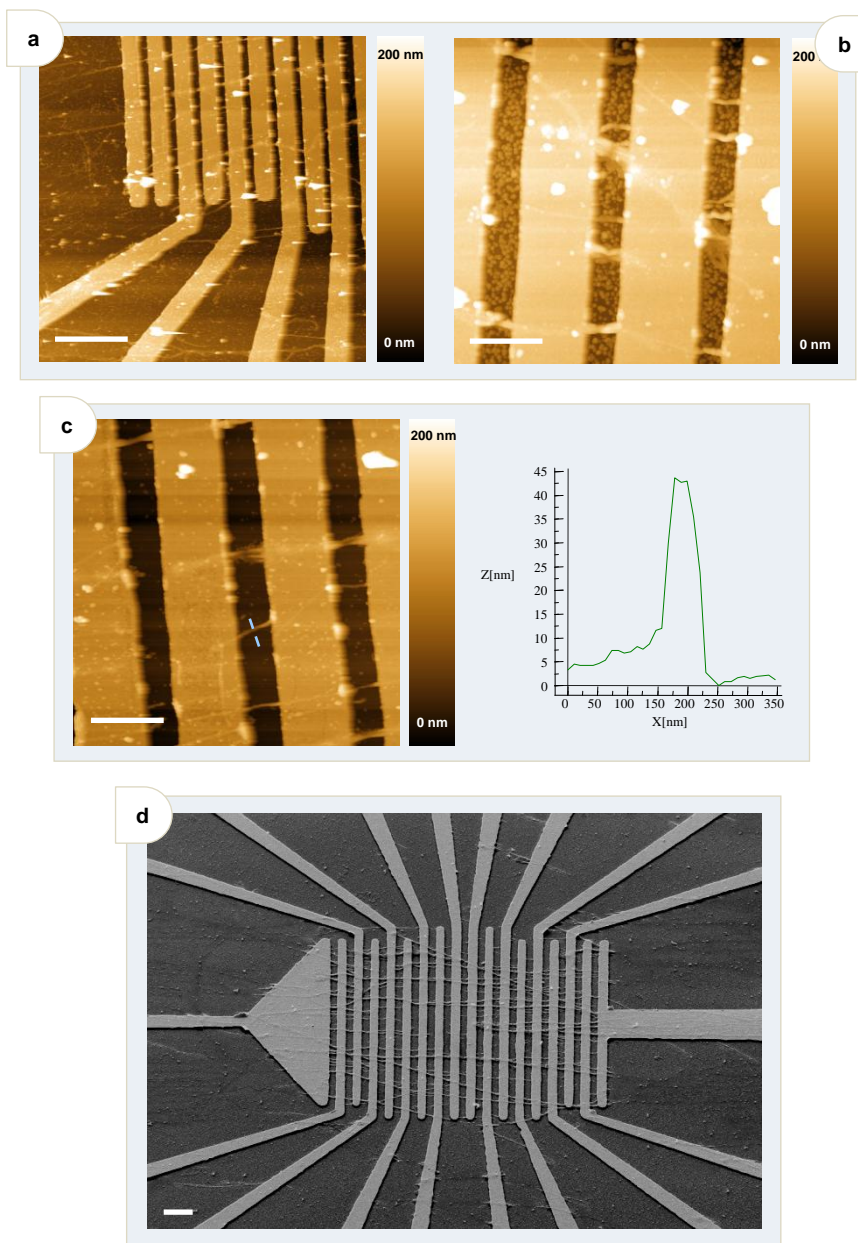

Figure 5.4: AFM images of silica-gold chips with PPy nanowires:
(a, c) Py concentration 3 mg/mL, polymerization time 50 seconds; Scale bar: (a) 4 µm, (c) 1 µm;
(b) Py concentration 7 mg/mL, polymerization time 40 seconds; Scale bar – 1 µm.
(d) SEM image of silica-gold chips with PPy nanowires; Scale bar – 4 µm.

It was shown that low polymerization time lead to no nanowires fabrication, while high polymerization time results in film formation. This experimental observation could be explained by different stages of the PPy grains growth. At the beginning, when PPy just start to grow at several spots along the polyelectrolyte nanostructure, the conductivity equal zero because the grains do not touch each others. An electrically conductive nanowire appears as the growth of the grains reaches the point when contact is established among them. The electrical conductivity of the nanowires jumps from the zero level at that moment and progressively rises with the increase of the polymerization time (and of the PPy structures height) to the certain highest value. This highest value of the conductivity represents the electrical property of thick PPy films and the PPy bulk.
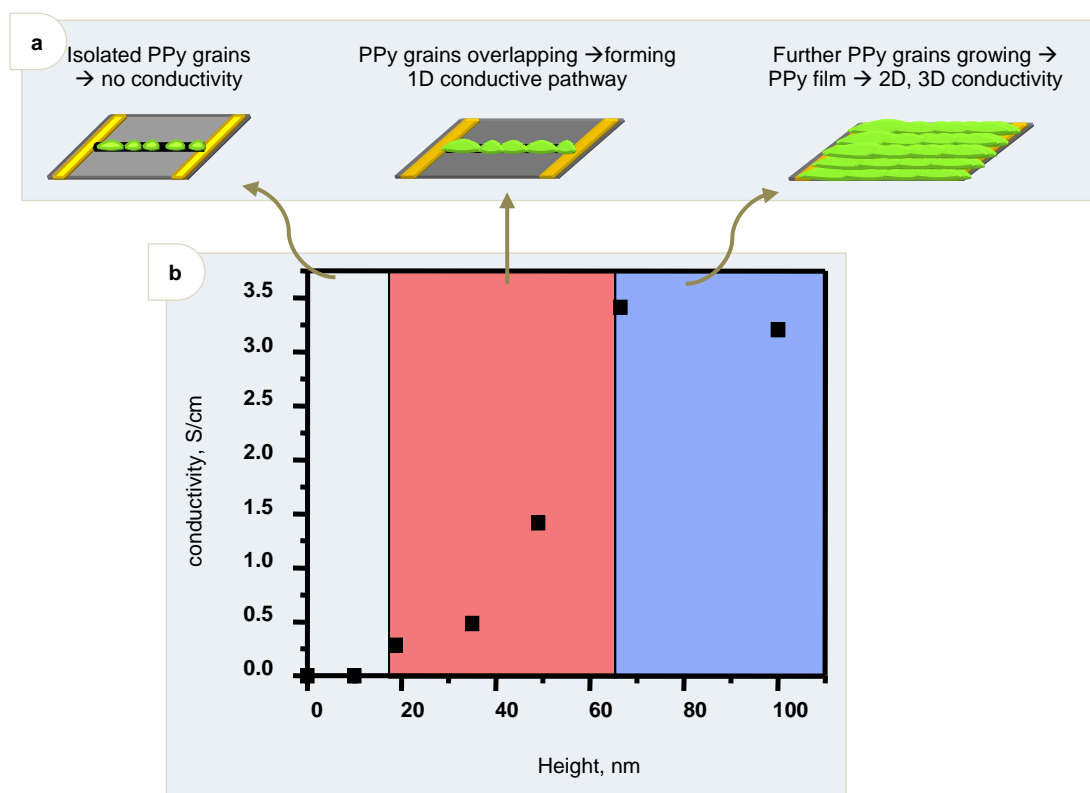

Figure 5.5: (a) Scheme of PPy nanostructures formation during polymerization. From left to right: PPy grains formation on polyelectrolyte template; PPy nanowire; PPy film; (b) PPy conductivity dependence on PPy height.

Water is a poor solvent for Py and PPy. During the polymerization in a solution, which take place at the same time with the Py polymerization on polyelectrolyte

nanostructures, the growth of the PPy grains and their solubility decrease with the increase of their size. The PPy film formation could be explained by the process of adsorption of the PPy grains from the water solution (see figure 5.5).

5.3.3. Investigation of the electrical properties

Using AFM after polyelectrolyte bundles deposition and polymerization I obtained several PPy nanowires between each contact pair.

In this thesis the nanowires were characterized by the "two-contact" method. Although the "four-contact" measurements allows to eliminate the contribution from the well-known "contact" problems originating from possible defects on the electrode-nanowire interface, in our case the "four-contact" method was impossible to implement. The reason for this is that it is very difficult to position single nanowires on four electrodes. Generally my attempts led to devices with nanowires that were mostly too short to bridge four electrodes. The "contact problems" associated with morphological defects in the contact areas and improper charge-injection between PPy and the gold electrodes cannot be recognized from the "two-contact" method of the conductivity measurements but it can be indirectly proved that the existence of such problems is not likely in my case. This conclusion comes from the AFM inspection of the electrode-PPy interface. As seen from figure 5.4b, c, the interface looks quite smooth on topography images suggesting rather good mechanical contact.

For characterization of the electrical properties the conductive measurements were carried out as described in experimental section. The current *vs.* voltage dependence in region 0.1 - 1 V could be approximated by a line, therefore Ohm`s law can be applied: $Y = \frac{U}{R}$, where U – voltage applied to the system, Y – current recorded from the system, R – electrical resistance.

I assume that geometrically each PPy nanowire could be approximated as a half-cylinder. Then the resistivity of this body can be found as $R = \rho \frac{2l}{\pi r^2}$, where l – length of the half-cylinder; r – radius; ρ - static resistivity. Several nanowires connected in parallel have the resistivity $\frac{1}{R} = \frac{1}{R_1} + \frac{1}{R_2} + \cdots + \frac{1}{R_n}$ (n – number of nanowires). Assuming that static

115

resistivity slightly depends on the radius I propose an equation for the resistance of several nanowires connected in parallel:

$$\frac{1}{R} = \frac{\pi}{2\rho}\left(\frac{r_1^2}{l_1} + \frac{r_2^2}{l_2} + \cdots + \frac{r_n^2}{l_n}\right). \tag{5.E1}$$

Taking R from Ohm`s law and $\sigma = \frac{1}{\rho}$ I got an equation for calculation of the electrical conductivity of a single PPy nanowire from the data obtained from electrical measurements and the AFM data (the number of nanowires between the contacts, their heights and lengths were measured):

$$\sigma = \frac{2Y}{\pi U\left(\frac{r_1^2}{l_1} + \frac{r_2^2}{l_2} + \cdots + \frac{r_n^2}{l_n}\right)}. \tag{5.E2}$$

This electrical conductivity is used as the characteristic electrical property of the samples. Conductivity is independent of the geometry and reflects only the fundamental property of matter.

The electrical measurements revealed the resistance of single nanowires in the range of 0.6-1.5 MΩ that corresponds to their conductivity of about 1-3 S/cm. This rather high value approaches the conductivity of PPy in the bulk.[Wu1997]
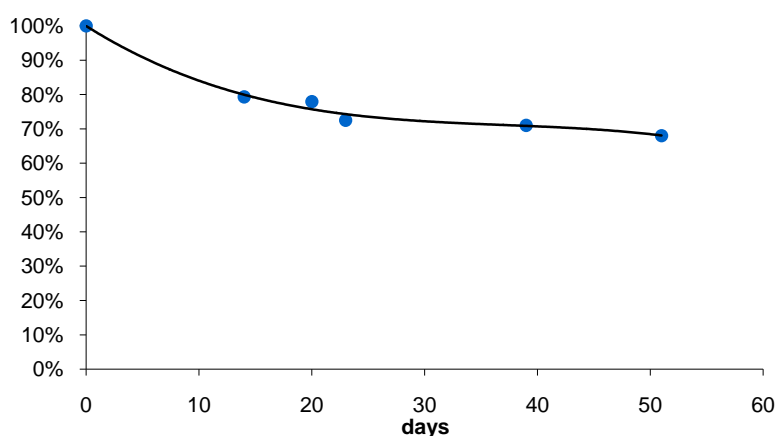

Figure 5.6: PPy nanowires aging – the drop of conductivity. Dots correspond to the experimental data, the curve represents the approximation of the experimental data by polynom.

It was reported that PPy films are usually not stable under ambient conditions and their conductivity decreases with time. In general, the stability of the polypyrrole films depends on many factors.[Mitchell1988] The most important are their structures, mobility of the doping counterion and possible side reactions occurring during polymerization of polypyrrole. These reactions lead to various defects in polymer chains and, consequently, enhance the degradation upon interaction with oxygen or water.[Thieblemont1994] It was found that films of polypyrrole with Cl$^-$ counterion lose more than 70% of their initial conductivity in 25 days due to the high mobility of the counterions.[Thieblemont1994] On the other hand, aromatic counterions have no such high mobility and films have higher conductivity and stability.[Mitchell1988]

In my case, it was found that PPy nanowires have the conductivity of several S/cm just after preparation (see figure 5.5). The conductivity of the samples stored in air decreases with time, obviously because of chemical degradation (see figure 5.6).

5.4. Conclusion

Quasiperiodic aligned and oriented nanostructures of polyelectrolyte molecules formed in moving droplets have been utilized for fabrication of electrically conductive one-dimensional nanowires. In particular, I have used a simple chemical route to fabricate conductive PPy nanowires by grafting of PPy from isolated synthetic polyelectrolyte molecules or their bundles. The location and length of the synthesized PPy nanowires are defined by the location and length of the deposited PSSA templates. The diameter of the nanowires varies from several nanometers to a hundred of nanometers and can be adjusted by changing the polycondensation time and the concentration of reagents. The DC conductivity of individual PPy nanowires approaches the conductivity of PPy in the bulk. This result opens broad opportunities for fabrication of electronic devices and sensors at the molecular level.

References

Adachi1995   Adachi, E.; Dimitrov, A. S.; Nagayama, K. Langmuir 1995, 11, 1057.

Bensimon1994   Bensimon, A.; Simon, A.; Chiffaudel, A.; Croquette, V.; Heslot, F.; Bensimon, D. Science 1994, 265, 2096.

Bensimon1995   Bensimon, D.; Simon, A.; Croquette, V.; Bensimon, A. Phys. ReV. Lett. 1995, 74, 4754.

Berg1993   Berg, J. C. Ed.; Marcel Dekker: Wettability; New York, 1993.

Bjork2005   Bjork, P.; Herland, A.; Scheblykin, I. G.; Inganas, O. Nano Lett. 2005, 5, 1948.

Blake1969   Blake, T. D.; Haynea, J. M. J. Colloid Interface Sei. 1969,30,421.

Bocharova2004   Bocharova, V; Kiriy, A.; Gorodyska, G.; Minko, S.; Stamm, M. Assembling of Prussian Blue Nanoclusters Along Single Polyelectrolyte Molecules. Polymer Materials: Science & Engineering 2004, 90, 593.

Bocharova2005   Bocharova, V.; Kiriy, A.; Vinzelberg, H.; Moench, I.; Stamm, M. Polypyrrole Nanowires Grown from Single Adsorbed Polyelectrolyte Molecules Angew. Chem. 2005, 117, 6549-6552.

Bocharova2006   Bocharova, V.; Kiriy, A.; Stamm, M.; Stoffelbach, F.; Jerome R.; Detrembleur , C. Simple Method for the Stretching and Alignment of Single Adsorbed Synthetic Polycations. Small 2006, 2, 910-916.

Bocharova2006-2   Bocharova, V.; Kiriy, A.; Vinzelberg, H.; Mönch, I.; Stamm, M. Polypyrrole Nanowires Grown from Polyelectrolyte Single Molecules: Conductivity in Aqueous Solutions Polymeric Materials: Science & Engineering 2006, 51, 222

Bradbury1996   Bradbury, S. and Evennett, P., Fluorescence microscopy., Contrast Techniques in Light Microscopy., BIOS Scientific Publishers, Ltd., Oxford, United Kingdom (1996).

Braun1998   Braun, E.; Eichen, Y.; Sivan, U.; Ben-Yoseph, G. Nature 1998, 391, 775.

Brochard-Wyart1994   Brochard-Wyart, F.; de Gennes, P.-G.; Herver, H.; Redon, C. Langmuir 1994,10, 1566-1572

Cachile2002   Cachile, M.; Be'nichou, O.; Cazabat, A. M. Langmuir 2002, 18, 7985.

Cachile2002-2   Cachile, M.; Be'nichou, O.; Poulard, C.; Cazabat, A. M. Langmuir 2002, 18, 8070.

Cahn1960   Cahn, J. W., 1960, ''On spinodal decomposition,'' Acta. Metall. 9, 795-801.

Chow1998   Chow, T. S. J. Phys.: Condens. Matter 1998, 10, L445.

Cox1986   Cox, R. G. J. Fluid Mech. 1986, 168, 169.

Davidson   Davidson M., Abramowitz M. Optical microscopy.

de Gans2004   de Gans, B. J.; Schubert, U. S. Langmuir 2004, 20, 7789.

de Gennes1979   de Gennes, P.-G. C. R. Acad. Sci. 1979, 228B, 219.

de Gennes1985   de Gennes, P. G. "Wetting: Statics and dynamics," Rev. Mod. Phy., vol. 57, p. 827, 1985.

de Gennes1985   de Gennes, P. G. Reo. Mod. Phys. 1985,57,827.

Deegan1997   Deegan, R. D.; Bakajin, O.; Dupont, T. F.; Huber, G.; Nagel, S. R.; Witten, T. A. Nature 1997, 389, 827.

Deegan2000   Deegan, R. D.; Bakajin, O.; Dupont, T. F.; Huber, G.; Nagel, S. R.; Witten, T. A. Phys. Rev. E 2000, 62, 756.

Deegan2000-2   Deegan, R. D. Phys. ReV. E 2000, 61, 475.

Dowson1979   Dowson, D., 1979, History of Tribology (Longmans, Green, London/New York).

Drexler1991   Drexler, E. (1991). Nanosystems: Molecular Machinery, Manufacturing, and Computation. MIT PhD thesis. New York: Wiley. ISBN 0471575186.

Dusean1979   Dusean V., E. B. Annu. Rev. Fluid Mech. 1979, 11, 371.

Dussan1974   Dussan V., E. B., and S. H. Davis, 1974, ''On the motion of fluid-fluid interface along a solid surface,'' J. Fluid Mech. 65, 71-95.

Dzyaloshinskii1959   Dzyaloshinskii, I. E., E. M. Lifshitz, and L. P. Pitaevskii, 1959, ''Van der Waals forces in liquid films,'' Zh. Eksp. Teor. Fiz. 37, 229-241 [Sov. Phys. JETP 10, 161-170 (1960)].

Fang2006   Fang, X.; Li, B.; Petersen, E.; Seo, Y. S.; Samuilov, V. A.; Chen, Y.; Sokolov, J. C.; Shew, C. Y.; Rafailovich, M. H. Langmuir 2006, 22, 6308.

Favier2001   Favier, F.; Walter, E. C.; Zach, M. P.; Benter, T.; Penner, R. M. Science 2001, 293, 2227-2231.

Feynman2000   Feynman, R. P. Selected papers of Richard Feynman (River Edge, NJ, 2000).

Fox1955   Fox, H. W.; Hare, E. F.; Zisman, W. A. "Wetting properties of organic liquids on high energy surfaces," J. Phys. Chem., vol. 59, p. 1097, 1955.

Fukai2006   Fukai, J.; Ishizuka, H.; Sakai, Y.; Kaneda, M.; Morita, M.; Takahara, A. Int. J. Heat Mass Transfer 2006, 49, 3561.

Gleiche2000   Gleiche, M.; Chi, L. F.; Fuchs, H. Nature 2000, 403, 173.

Golestanian2001   Golestanian, R.; Raphaeïl, E. Europhys. Lett. 2001, 55, 228.

Golestanian2004   Golestanian, R. Philos. Trans. R. Soc. London, Sect. A 2004, 362, 1613.

Gonuguntla2004   Gonuguntla, M.; Sharma, A. Langmuir 2004, 20, 3456.

Haidara2001   Haidara, H.; Mougin, K.; Schultz, J. Langmuir 2001, 17, 659.

Hansen1971   Hansen, R. J.; Toong, T. Y. J. Colloid Interface Sci. 1971,37,196

Harris2007   Harris, D. J.; Hu, H.; Conrad, J. C.; Lewis, J. A. Phys. ReV. Lett. 2007, 98, 148301.

References

Henrichs1999	Henrichs, S. E.; Sample, J. L.; Shiang, J. J.; Heath, J. R.; Collier, C. P.; Saykally, R. J. J. Phys. Chem. B 1999, 103, 3524-3528.
Herman1993	Herman B., Lemasters J. J. (eds.), Optical Microscopy: Emerging Methods and Applications. Academic Press, New York, 1993, 441 pp.
Hocking1982	Hocking, L. M.; Rivers, A. D. J. Fluid Mech. 1982, 121, 425.
Huh1971	Huh, C.; Scriven, L. E. J. Colloid Interface Sci. 1971,35, 85.
Huppert1982	Huppert, H. E. Nature 1982, 300, 427.
Israelachvili1992	Israelachvili, J. Intermolecular and Surface Forces, 1992. Academic Press.
Jameel1994	Jameel, A. T., and A. Sharma, 1994, ''Morphological phase separation in thin liquid films,'' J. Colloid Interface Sci. 164, 416-427.
Jeon1997	Jeon, N. L.; Finnie, K.; Branshaw, K.; Nuzzo, R. G. Langmuir 1997, 13, 3382.
Joanny1984	Joanny, J. F.; de Gennes, P. G. J. Chem. Phys. 1984, 81, 552.
Joanny1986	Joanny, J. F.; de Gennes, P. G. "Upward creep of a wetting fluid - a scaling analysis," J. Phys., vol. 47, p. 121, 1986.
Kajiya2006	Kajiya, T.; Nishitani, E.; Yamaue, T.; Doi, M. Phys. Rev. E: Stat., Nonlinear, Soft Matter Phys. 2006, 73, 011601.
Kajiya2009	Kajiya, T.; Monteux, C.; Narita, T.; Lequeux, F.; Doi, M. Langmuir, Article ASAP DOI: 10.1021/la900216k Publication Date (Web): 08 April 2009
Kaneda2008	Kaneda, M.; Hyakuta, K.; Takao, Y.; Ishizuka, H.; Fukai, J. Langmuir 2008, 24, 9102.
Khanduyeva2009	Khanduyeva, N.; Senkovskyy, V.; Beryozkina, T.; Horecha, M.; Stamm, M.; Uhrich, C.; Riede, M.; Leo, K.; Kiriy, A. J. Am. Chem. Soc., 2009, 131 (1), pp 153–161, DOI: 10.1021/ja8050734
Kheshgi1991	Kheshgi, H. S., and L. E. Scriven, 1991, ''Dewetting: nucleation and growth of dry regions,'' Chem. Eng. Sci. 46, 519-526.
Kiriy2002	Kiriy, A.; Gorodyska, A.; Minko, S.; Jaeger, W.; Sÿtepaˊnek, P.; Stamm, M. J. Am. Chem. Soc. 2002, 124, 13454.
Kiriy2002-2	Kiriy, A.; Gorodyska, A.; Minko, S.; Jaeger, W.; Sÿtepaˊnek, P.; Stamm, M. J. Am. Chem. Soc. 2002, 124, 13454.
Kiriy2002-3	Kiriy, A.; Minko, S.; Gorodyska, G.; Stamm, M.; Jaeger, W. Nano Lett. 2002, 2, 881.
Kiriy2003	Kiriy, A.; Gorodyska, A.; Minko, S.; Tsitsilianis, C.; Jaeger, W.; Stamm, M. J. Am. Chem. Soc. 2003, 125, 11202.
Kovalchuk2003	Kovalchuk, V. I.; Bondarenko, M. P.; Zholkovskiy, E. K.; Vollhardt, D. J. Phys. Chem. B 2003, 107, 3486-3495.
Kumar1994	Kumar, A.; Biebuyck, H. A.; Whitesides, G. M. Langmuir 1994, 10, 1499.
Kumar1995	Kumar, S.; Reich, D. H.; Robbins, M. O. Phys. ReV. E 1995, 52, R5776.

Kuncicky2006   Kuncicky, D.; Naik, R. R.; Velev, O. D. Small 2006, 2, 1462.

Laibinis1989   Laibinis, P. E.; Hickman, J. J.; Wrighton, M. S.; Whitesides, G. M. Science 1989, 245, 845.

Landau1987   Landau, L. D., and E. M. Lifshits, 1987, Fluid Mechanics (Oxford, London).

Lenhert2004   Lenhert, S.; Zhang, L.; Mueller, J.; Wiesmann, H. P.; G., E.; Fuchs, H.; Chi, L. F. AdV. Mater. 2004, 16, 619-624.

Liu2008   Liu, G.; Zhang, C.; Zhao, J.; Zhu, Y.; Langmuir, 2008, 24 (15), 7923-7930.

Lopez1976   Lopez, J.; M. C. A, and E. Ruckenstein, "Spreading kinetics of liquid-drops on solids," J. Colloid. Interface Sci, vol. 56, p. 460, 1976.

Lowndes1980   Lowndes, J. J. Fluid Mech. 1980,101, 631.

Lu2002   Lu, N.; Gleiche, M.; Zheng, J.; Lenhert, S.; Xu, B.; Chi, L. F.; Fuchs, H. AdV. Mater. 2002, 14, 1812-1815.

Maeda1999   Maeda, H. Langmuir 1999, 15, 8505.

Maeda2000   Maeda, H. Langmuir 2000, 16, 9977.

Maheshwari2008   Maheshwari, S.; Zhang, L.; Zhu, Y.; Chang, H.-C. Phys. ReV. Lett. 2008, 100, 044503.

Mahnke1999   Mahnke, J.; Vollhardt, D.; Sto¨ckelhuber, K. W.; Meine K.; Schulze, H. J. Langmuir 1999, 15, 8220.

Maier2003   Maier, S. A.; Kik, P. G.; Atwater, H. A.; Meltzer, S.; Harel, E.; Koel, B. E.; Requicha, A. A. G. Nat. Mater. 2003, 2, 229-232.

Maillard2001   Maillard, M.; Motte, L.; Pileni, M. P. Adv. Mater. 2001, 13, 200.

Marmur1983   Marmur, A. "Equilibrium and spreading of liquids on solid-surfaces," Adv. Colloid. Interf. Sci., vol. 19, p. 75, 1983.

Marsh1993   Marsh, J. A.; Cazabat, A. M. Phys. ReV. Lett. 1993, 71, 2433.

Messerschmidt2001   Messerschmidt, C.; Schwartz, D. K. Langmuir 2001, 17, 462.

Michalet1997   Michalet, X.; Ekong, R.; Fougerousse, F.; Rousseaux, S.; Schurra, C.; Hornigold, N.; Slegtenhorst, M.; Wolfe, J.; Povey, S.; Beckmann, J.; Bensimon, A. Science 1997, 277, 1518.

Minsky1957   Minsky M. US 3013467 (A)

Mitchell1988   Mitchell, G.R.; Davis, F.G.; Legge, C.H. Synthetic Metals 1988, 26, 247-257.

Mitlin1993   Mitlin, V. S., 1993, ''Dewetting of solid surface: analogy with spinodal decomposition,'' J. Colloid Interface Sci. 156, 491-497.

Mitlin1994   Mitlin, V. S., and N. V. Petviashvili, 1994, ''Nonlinear dynamics of dewetting: kinetically stable structures,'' Phys. Lett. A 192, 323-326.

Moraille2002   Moraille, P.; Badia, A. Angew. Chem., Int. Ed. Engl. 2002, 41, 4303-4306.

Mougin2002   Mougin, K.; Haidara, H. Langmuir 2002, 18, 9566.

References

Nakao2003   Nakao, H.; Gad, M.; Sugiyama, S.; Otobe, K.; Ohtani, T. J. Am. Chem. Soc. 2003, 125, 7162.

Nakao2005   Nakao, H.; Hayashi, H.; Iwata, F.; Karasawa, H.; Hirano, K.; Sugiyama, S.; Ohtani, T. Langmuir 2005, 21, 7945.

Neves2000   Neves, B. R. A.; Salmon, M. E.; Russell, P. E.; Troughton, E. B. Langmuir 2000, 16, 2409.

Neves2001   Neves, B. R. A.; Salmon, M. E.; Troughton, E. B., Jr.; Russell, P. E. Nanotechnology 2001, 12, 285.

Nguyen2002   Nguyen, V. X.; Stebe, K. J. Phys. Rev. Lett. 2002, 88, 164501-1.

Nie2002   Nie, H.-Y.; Walzak, M. J.; McIntyre, N. S. Langmuir 2002, 18, 2955.

Nikolayev2005   Nikolayev, V. S. J. Phys.: Conden. Matter. 2005, 17, 2111.

Ondarcuhu1991   Ondarcuhu, T.; Veyssie´, M. Nature 1991, 352, 418.

Oron1997   Oron, A., S. G. Bankoff, and S. H. Davis, 1997, ''Evolution of a thin evaporating liquid film heated by a spatially nonuniform heat flux,'' Rev. Mod. Phys. 69, 931 - 980

Pignataro2002   Pignataro, B.; Sardone, L.; Marletta, G. Mater. Sci. Eng. C 2002, 22, 177-181.

Poulard2003   Poulard, C.; Be'nichou, O.; Cazabat, A. M. Langmuir 2003, 19, 8828.

Przerwa2004   Przerwa, E.; Sosnowski, S.; Slomkowski, S. Langmuir 2004, 20, 4684-4689.

Ramos2003   Ramos, S. M. M.; Charlaix, E.; Benyagoub, A. Surf. Sci. 2003, 540, 355.

Ramos2003   Ramos, S. M. M.; Charlaix, E.; Benyagoub, A.; Toulemonde, M. Phys. ReV. E 2003, 67, 031604.

Ramos2006   Ramos, S.; Tanguy, A. Eur. Phys. J. E 2006, 19, 433.

Raphael1989   Raphael, E.; de Gennes, P. G. J. Chem. Phys. 1989, 90, 7577.

Raudino2007   Raudino, A.; Pignataro, B. J. Phys. Chem. B, 2007, 111 (31), 9189-9192.

Reynolds1886   Reynolds, O., 1886, ''On the theory of lubrication and its application to Mr. Beauchamp Tower's experiments, including an experimental determination of the viscosity of olive oil,'' Philos. Trans. R. Soc. London 177, 157-234.

Roco1999   Roco M. C., Williams R. S., Alivisatos P. Nanostructure Science and Technology (Book Springer, 1999).

Rowlinson1984   Rowlinson, J. S.; Widom, B. "Molecular theory of capillarity," Clarendon Press, 1984.

Schlichting1968   Schlichting, H., 1968, Boundary-layer Theory (McGraw-Hill, New York).

Sedev1992   Sedev, R. V.; Petrov, J. G. Colloids Surf. 1992, 62, 141.

Seemann2005   Seemann, R.; Brinkmann, M.; Kramer, E. J.; Lange, F. F.; Lipowsky, R. Proc. Natl. Acad. Sci. U.S.A. 2005, 102, 1848.

Severin2004   Severin, N.; Rabe, J. P.; Kurth, D. G. J. Am. Chem. Soc. 2004, 126, 3696.

Sharma1986   Sharma, A., and E. Ruckenstein, 1986, ''An analytical nonlinear theory of thin film rupture and its application to wetting films,'' J. Colloid Interface Sci. 113, 456-479.

Sharma1993   Sharma, A., and A. T. Jameel, 1993, ''Nonlinear stability, rupture, and morphological phase separation of thin fluid films on apolar and polar substrates,'' J. Colloid Interface Sci. 161, 190-208.

Shipway2000   Shipway, A. N.; Katz, E.; Willner, I. ChemPhysChem 2000, 1, 18-52.

Shmuylovich2002   Shmuylovich, L.; Shen, A. Q.; Stone, H. A. Langmuir 2002, 18, 3441.

Simon1998   Simon, U. Adv. Mater. 1998, 10, 1487-1492.

Smalyukh2006   Smalyukh, I. I.; Zribi, O. V.; Butler, J. C.; Lavrentovich, O. D.; Wong, G. C. L. Phys. ReV. Lett. 2006, 96, 177801.

Spratte1994   Spratte, K.; Chi, L. F.; Riegler, H. Europhys. Lett. 1994, 25, 211-217.

Takhistov2002   Takhistov, P.; Chang, H.-C. Ind. Eng. Chem. Res. 2002, 41, 6256.

Taniguchi1974   Taniguchi N. (1974). On the Basic Concept of 'Nano-Technology. Proc. Intl. Conf. Prod. London, Part II British Society of Precision Engineering.

Tanner1979   Tanner, L. H. "Spreading of silicone oil drops on horizontal surfaces," J. Phys. D, vol. 12, p. 1473, 1979.

Teletzke1988   Teletzke, G. F., H. T. Davis, and L. E. Scriven, 1988, ''Wetting hydrodynamics,'' Rev. Phys. Appl. 23, 989-1007.

Textor2000   Textor, M.; Ruiz, L.; Hofer, R.; Rossi, A.; Feldman, K.; Hahner, G.; Spencer, N. D. Langmuir 2000, 16, 3257.

Thieblemont1994   Thieblemont, J.C.,;Gabelle, J.L.; Planche, M.F. Synthetic Metals 1994, 66, 243-247.

Ulman1996   Ulman, A. Chem. ReV. 1996, 96, 1533.

Vannimenus2002   Vannimenus, J. Physica A 2002, 314, 264.

Visser1972   Visser, J. "On Hamaker constants: A comparison between Hamaker constants and Lifshitz-van der Waals constants," Adv. Colloid Interface Sci., vol. 3, p. 331, 1972.

Voinov1976   Voinov, 0. V. Izu. Akad. Nauk SSSR, Mekh. Zhidk. Gaza 1976 576; Fluid Dun. (Engl. Tranal.) 1976,11,714.

Vyawahare2006   Vyawahare, S.; Craig, K. M.; Scherer, A. Nano Lett. 2006, 6, 271.

Williams1981   Williams, M. B., 1981, ''Nonlinear theory of film rupture,'' Ph.D. thesis (Johns Hopkins University).

Williams1982   Williams, M. B., and S. H. Davis, 1982, ''Nonlinear theory of film rupture,'' J. Colloid Interface Sci. 90, 220-228.

Woodward1996   Woodward, J. T.; Ulman, A.; Schwartz, D. K. Langmuir 1996, 12, 3626.

Wu1997   Wu, C.; Chen, C. J. Mater. Chem. 1997, 7, 1409.

References

Xu2004   Xu, H.; Shirvanyants, D.; Beers, K. L.; Matyjaszewski, K.; Dobrynin, A. V.; Rubinstein, M.; Sheiko, S. S. Phys. ReV. Lett. 2004, 93, 206103.

Xu2005   Xu, H.; Shirvanyants, D.; Beers, K. L.; Matyjaszewski, K.; Dobrynin, A. V.; Rubinstein, M.; Sheiko, S. S. Phys. ReV. Lett. 2005, 94, 23780.

Yaminski1997   Yaminski, V.; Nylander, T.; Ninham, B. Langmuir 1997, 13, 1746-1757.

Zhang2005   Zhang J.; Ma, Y.; Stachura, S.; He, H. Langmuir 2005, 21, 4180-4184

Zhang2008   Zhang, L.; Maheshwari, S.; Chang, H. C.; Zhu, Y. Langmuir 2008, 24, 3911.

Summary and outlook

Summary

A crucial problem of nanotechnology is that a number of different elements have to be integrated into complex and predictably operating systems. It was previously shown that single molecules of polymers or their structures can be utilized as diverse and convenient nanotechnological building blocks. It is important that the modern polymer chemistry provides an access to various molecules (building blocks) of desired size, shape (architecture) and functionality. Important advantage of the proposed "single-molecule approach" is that, in principle, it would give a possibility for manipulation and organization of complex structures via self-assembly. Just like conventional ropes, single molecules of linear polymers could be stretched and aligned under external forces (e.g., centrifugal or capillary forces, electric or shear fields) and immobilized onto surfaces by simple procedures like casting or printing. Recently it was demonstrated that single polyelectrolyte molecules could be randomly deposited and stretched using a spincoating technique. These molecules were used as positive templates for conductive nanowires fabrication, that makes them a perspective candidates for fabrication of nanodevices and sensors.

However, an important drawback of the developed method is its low reproducibility and uncontrolled orientation and positioning of the structures. Another drawback of the polyelectrolyte nanoobjects is lack of a useful functionality in their structure that would contribute to electrical conductivity, specific adsorption of biomolecules, etc.

In a view of this, the development of new advanced deposition techniques for a high throughput preparation of aligned structures with known orientation is an important task. Furthermore, it is important to investigate deeply the deposition process in order to identify the key factors of the nanostructures formation. The obtained knowledge will allow systematically control the morphology of the resulting structures (type of the structures, feature size, orientation, periodicity, etc.), that is necessary for nanofabrications of electronic devices and sensors. Still another task of the

present thesis is the development of efficient and, desirably, universal methods for conversion of electrically non-conductive templates into conductive nanowires or other functional nanostructures.

It was found that one dimensional nanostructures of polyelectrolytes are formed on hydrophobic surfaces in the moving contact line. It was demonstrated that the morphology of nanostructures displays a range of structure variations from root-like to single wire structures with a high anisotropy and aspect ratio (providing diameters of several nanometers and the length limited by the sample surface dimensions).

Detailed investigation of the deposition process allowed to determine that each nanostructure within the oriented arrays is aligned perpendicular to the local receding contact line. This finding provides a possibility to control the orientation of nanostructures on the macroscopic level by changing the movement direction and the shape of the receding contact line. It was also found that the formed nanostructures display an extremely high aspect ratio. Typically, PSSA bundles have the diameter of several nanometers and the length of many microns.

The number of bundles per micron, their height distribution, and the number of knots depend on the speed of the droplet movement and on solution concentration. The higher the movement speed the lower the number of bundles is. At the same time, the structures formed at higher deposition speeds usually have less branched morphology, and are thinner. At the same time, decrease of the polyelectrolyte solution concentration derives similar changes in the morphology of the resulting structures as the increase in the deposition speed.

It was found that there is a critical polyelectrolyte concentration below of which the bundles on the surface are not formed and, in general, the deposition process becomes unstable and poorly reproducible. It was further found that this critical concentration depends on the molecular weight of the polyelectrolyte and it decreases with the increase of the molecular weight or upon addition of multivalent ions. These observations suggest an important role on the deposition process of intermolecular interactions between the polyelectrolyte chains that occur in solutions. In this case, promoting of the intermolecular interactions (entanglement and ionic bonding) favors the formation of very long well-aligned and continuous fibers.

The method of preparing of the 1D nanostructures was found to be fairly universal and applicable to a wide range of polyelectrolytes of different nature (charge, hydrophobisity) and also to a numerous surfaces kinds. The only prerequisite for successful fabrication of the aligned PE structures is that a low adhesion force between the droplet with PE water solution and the applied surface to provide an easy movement of the droplet without the deposition of macroscopic films of water solution.

As such, the surfaces with high enough hydrophobisity (e.g., polydimethylsiloxane, polytetrafluoroethylene, polystyrene, poly(methyl methacrylate), poly(glycidyl methacrylate), poly(tert-butyl acrylate)) are suitable for the preparation of the nanostructures, whereas, hydrophilic surfaces (e.g., silica, glass, poly-2-vinylpyridine) are not suitable substrates.

It was demonstrated that such nanostructures can be produced exactly on a place when they are needed or they can be transferred by a contact printing technique from hydrophobic stamps to other surfaces.

A model describing the polymer deposition during the moving contact line processes on hydrophobic surfaces has been proposed. The application of this model provides the ground for an explanation of all the obtained experimental data.

The prepared aligned one-dimensional polyelectrolyte structures were used as templates for assembling amphiphile molecules bearing a charge opposite to the charge of the template. Thus prepared one dimensional self-assembled monolayers of functional amphiphilic compounds can be transferred onto mica or silica wafers. We believe that these nanostructures with polymerizable pyrrole headgroups will be useful for the creation of electrically conductive patterns of conjugated polymers. A combination of the self-assembly approaches with the traditional lithographic methods could be a promising way toward ordered patterns of polyelectrolyte templated SAMs.

Quasiperiodic aligned and oriented nanostructures of polyelectrolyte molecules formed in moving droplets were utilized for fabrication of electrically conductive one-dimensional nanowires. In particular, I have used a simple chemical route to fabricate conductive PPy nanowires by the grafting of PPy from isolated synthetic polyelectrolyte molecules or their bundles. The location and length of the synthesized PPy nanowires are defined by the location and length of deposited PSSA templates. Diameter of the

nanowires varies from few nanometers to hundred of nanometers and can be adjusted by polycondensation time and concentration of reagents. The DC conductivity of individual PPy nanowires approaches the conductivity of PPy in the bulk. This result opens broad opportunities for fabrication of electronic devices and sensors at molecular level.

Outlook

The results achieved open new and broad perspectives for the construction of molecule-based devices - sensors and transistors. Chemical and biological sensors on the basis of (semi)conductive polymer nanowires grown from single polyelectrolyte molecules and operating as analyte-gated field effect transistors (FETs) are a promising way for the real-time detection of extremely low concentrations (up to single-molecule level) of multiple biological targets (proteins, viruses, DNA/RNA, etc.) in vitro, and possibly even in vivo, inside leaving cells and viable alternative to inorganic nanoscale materials. In addition to the attractive properties of the inorganic NWs (e.g., variable conductivity and high surface-to-volume ratio), conducting polymer NWs possess the following important advantages: easy and cheap production (synthetic procedures exclude high temperatures and vacuum equipment); easy variability of chemical structure, size and shape of NWs allowing precise tuning of other properties (optical, electrical, surface functionality, charge, etc.). The operation principle of such sensors is based on changing of the conductivity in the channel in response on changed environment. Since most biological species (proteins, DNA or viruses) are charged (in water solutions), their binding results in depletion or accumulation (depending on the charge of the analyte) of carriers within the transistor and, therefore, in altered conductance. In such a way NW FETs can serve as efficient transducers transforming the chemical signals (recognition and binding events) into a technologically relevant electrical signal.

Acknowledgements